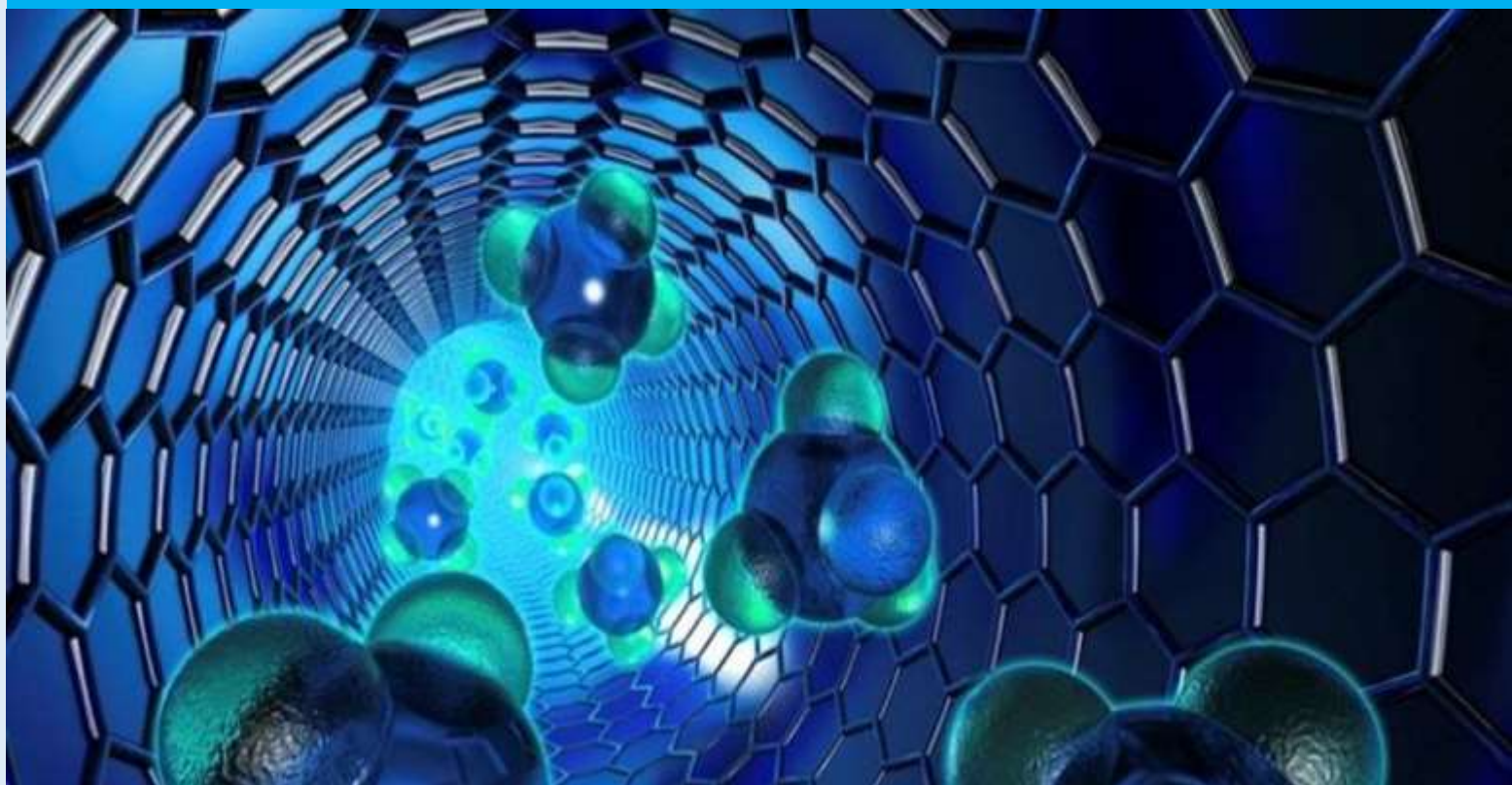


e-ISSN: 2602-277X

International Journal of and Chemistry



Volume: 4, Issue: 2
E - Journal

31 December 2020
<http://dergipark.org.tr/ijct>

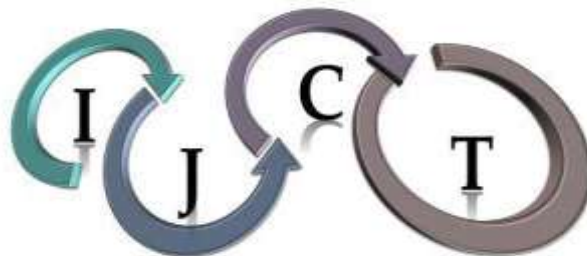


International Journal of Chemistry and Technology

JOURNAL INFO

Journal Name	International Journal of Chemistry and Technology
Journal Initial	IJCT
Journal Abbreviation	Int. J. Chem. Technol.
ISSN (Online)	2602-277X
Year of Launching	2017, August
Editor-in-Chief and Managing Editor	Prof. Dr. Bilal Acemioğlu
Manager of Publication	Assist. Prof. Mehmet Akyüz
Scope and Focus	Chemistry, Material Science, Technology
Review Type	Peer Review Double-Blinded
Ethical Rules	Plagiarism check, copyright agreement form, conflict of interest, ethics committee report
Access Type	Open Access
Publication Fee	Free
Article Language	English
Frequency of Publication	Biannualy
Publication Issue	June, December
Publisher	Prof. Dr. Bilal ACEMİOĞLU
Web Page	http://dergipark.org.tr/ijct
Contact E-mail address	ijctsubmission@gmail.com, ijctsubmission@yahoo.com
Contact Address and Executive address	Kilis 7 Aralık University, Faculty of Science and Arts, Department of Chemistry, 79000, Kilis
Contact Telephone	90 532 233 17 38 (Secretary)
Publication Date	28/12/2018
Technical Editor	Assist. Prof. Dr. Evrim BARAN AYDIN
Spelling Editor	Dr. Oğuzhan Koçer, MSc. Rabia Acemioğlu
Language (Grammar) Editor	Assist. Prof. Dr. Muhammet KARAMAN, Assist. Prof. Dr. Muhittin KULAK, Dr. Lawali YABO DAMBAGI
Secretary	Dr. Oğuzhan KOÇER, MSc. Rabia ACEMİOĞLU

All detailed information including instructions for authors, aim and scopes, ethical rules, manuscript evaluation, indexing info, and manuscript template etc. can be found on the main web page of IJCT (<http://dergipark.gov.tr/ijct>).



International Journal of Chemistry and Technology

Volume: 4, Issue: 2, Year 2020

Founder of IJCT

Prof. Dr. Bilal ACEMIOĞLU

EDITORIAL BOARD

Editor-in-Chief

Prof. Dr. Bilal ACEMIOĞLU

(Physical Chemistry, Kilis 7 Aralık University, Kilis, Turkey)

Associate Editors

Prof. Dr. İbrahim DEMİRTAŞ
(Organic Chemistry and Phytochemistry Iğdır
University, Iğdır, Turkey)

Prof. Dr. Yuh-Shan HO
(Chemical and Environmental Engineering,
Asia University, Taichung City, Taiwan)

Prof. Dr. M. Hakkı ALMA
(Material Science and Technology
K.Maraş Sütçü İmam/Iğdır University, Turkey)

Prof. Dr. Yahya GÜZEL
(Theoretical Chemistry and Polymer Chemistry
Erciyes University, Kayseri, Turkey)

Prof. Dr. Ekrem KÖKSAL
(Biochemistry,
Erzincan Binali Yıldırım University, Erzincan, Turkey)

Prof. Dr. Mustafa ARIK
(Physical Chemistry,
Atatürk University, Erzurum, Turkey)

Prof. Dr. Fevzi KILIÇEL
(Analytical Chemistry,
Karamanoğlu Mehmet Bey Uni., Karaman, Turkey)

Prof. Dr. Mehmet SÖNMEZ
(Inorganic Chemistry,
Gaziantep University, Gaziantep, Turkey)



International Journal of Chemistry and Technology

Advisory Editorial Board

Prof. Dr. Harun PARLAR
(Technical University of Munich, München Germany)

Prof. Dr. Shaobin WANG
(Curtin University, Perth, Australia)

Prof. Dr. Ana Beatriz Rodriguez MORATINOS
(University of Exramadura, Badajoz, Spain)

Prof. Dr. Jon-Bae KIM
(College of Health Sciences, South Korea)

Prof. Dr. Rashid AHMAD
(University of Malakand, Chakdara, Pakistan)

Prof. Dr. Guang-Jie ZHAO
(Beijing Forestry University, Beijing, China)

Prof. Dr. Jaine H. Hortolan LUIZ
(Federal University of Alfenas, Unifal-MG, Brazil)

Prof. Dr. Papita DAS
(Jadavpur University, Jadavpur, India)

Prof. Dr. Vagif ABBASOV
(Nef-Kimya Prosesleri Institutu, Baku, Azerbaijan)

Prof. Dr. Atiqur RAHMAN
(Islamic University, Kushita, Bangladesh)

Prof. Dr. Mika SILLANPAA
(LUT Lappeenranta Uni.y of Technology, Lappeenranta, Finland)

Prof. Dr. Salah AKKAL
(University of Mentouri Consatntine Consatntine, Algeria)

Prof. Dr. Gilbert Kapche DECCAUX
(University of Yaounde I, Yaounde, Cameroon)

Prof. Dr. Gelu BOURCEANU
(Alexandru Ioan Cuza University, Romania)

Prof. Dr. Ahmet ÇAKIR
(Kilis 7 Aralik University, Kilis, Turkey)

Prof. Dr. M. SALIH AĞIRTAŞ
(Yüzüncü Yıl University, Van, Turkey)

Prof. Dr. Nufullah SARAÇOĞLU
(Atatürk University, Erzurum, Turkey)

Prof. Dr. Rahmi KASIMOĞULLARI
(Dumlupınar University, Kütahya, Turkey)

Prof. Dr. Ahmet Baysar
(Inonu University, Malatya, Turkey)

Prof. Dr. Hamdi TEMEL
(Dicle University, Diyarbakır, Turkey)

Prof. Dr. Ö. İrfan KÜFREVOĞLU
(Atatürk University, Erzurum, Turkey)

Prof. Dr. Ömer ŞAHİN
(Siirt University, Siirt, Turkey)

Prof. Dr. Anatoli DIMOGLU
(Düzce University, Düzce, Turkey)

Prof. Dr. Mehmet UĞURLU
(Sıtkı Kocman University, Muğla, Turkey)

Prof. Dr. Şükrü BEYDEMİR
(Anadolu University, Eskişehir, Turkey)

Prof. Dr. Ramazan SOLMAZ
(Bingol University, Bingöl, Turkey)

Prof. Dr. Mahfuz ELMASTAŞ
(Health Sciences University, İstanbul, Turkey)

Prof. Dr. Mehmet DOĞAN
(Balıkesir University, Balıkesir, Turkey)

Prof. Dr. Giray TOPAL
(Dicle University, Diyarbakır, Turkey)

Prof. Dr. Birgül YAZICI
(Cukurova University, Adana, Turkey)



International Journal of Chemistry and Technology

Advisory Editorial Board

Prof. Dr. Barbaros NALBANTOĞLU
(Yıldız Technical University, İstanbul, Turkey)

Prof. Dr. Murat ALANYALIOĞLU
(Atatürk University, Erzurum, Turkey)

Prof. Dr. T. Abdulkadir ÇOBAN
(Erzincan Binali Yıldırım University, Erzincan Turkey)

Prof. Dr. İsmet KAYA
(18 Mart University, Çanakklae, Turkey)

Prof. Dr. Serhan URUŞ
(Sütçü İmam University, K.Maraş, Turkey)

Prof. Dr. Ömer İŞILDAK
(Gaziosmanpaşa University, Tokat, Turkey)

Prof. Dr. Halim AVCI
(Kilis 7 Aralık University, Kilis, Turkey)

Prof. Dr. Ahmet TUTAR
(Sakarya University, Sakarya, Turkey)

Prof. Dr. Duygu EKINCI
(Atatürk University, Erzurum, Turkey)

Prof. Dr. Metin BÜLBÜL
(Dumlupınar University, Kütahya, Turkey)

Prof. Dr. Ali KARA
(Uludağ University, Bursa, Turkey)

Prof. Dr. Murat SARAÇOĞLU
(Erciyes University, Kayseri, Turkey)

Prof. Dr. Murat SADIKOĞLU
(Gaziosman Paşa University, Tokat, Turkey)

Prof. Dr. Mustafa KARATAŞ
(Aksaray University, Aksaray, Turkey)

Assoc. Prof. Dr. Şenay ŞİMŞEK
(North Dakota State University, Fargo, USA)

Assoc. Prof. Dr. Mahjoub JABLI
(University of Monastir, Monastir, Tunisia)

Assoc. Prof. Dr. Muhammet KÖSE
(Sütçü İmam University, K.Maraş, Turkey)

Assoc. Prof. Chin-Hung LAI
(Chung Shan Medical University, Taiwan)

Assoc. Prof. Niyaz M. MAHMOODI
(Institute for Color Science and Technology Tehran, Iran)

Assoc. Prof. Dr. Mustafa ÖZDEMİR
(Süleyman Demirel University, Isparta, Turkey)

Assoc. Prof. Dr. Metin AÇIKYILDIZ
(Kilis 7 Aralık University, Kilis, Turkey)

Assist. Prof. Masood Ayoub KALOO
(Govt. Degree College Shopian, J & K, India)

Assist. Prof. Dr. Mutasem Z. BANI-FWAZ
(King Khalid University, Asir-Abha, Saudi Arabia)

Assist. Prof. Dr. Bakhtiyor RASULEV
(North Dakota State University, Fargo, USA)

Dr. Zineb TRİBAK
(Sidi Mohamed Ben Abdellah University, Fez Morocco)

Dr. Sameer Ahmed AWAD
(University of Anbar, Ramadi, Iraq)

Dr. Ramadan E. ASHERY
(Damanhour University, Egypt)



International Journal of Chemistry and Technology

Reviewers for June 2020, Vol: 4, Issue: 2

Assist Prof. Dr. Safa Majeed HAMEED
University Of Kufa, Najaf Governorate, Iraq

Assoc. Prof. Dr. Ayhan Abdullah CEYHAN
Konya Teknik University, Konya, Turkey

Assoc. Prof. Dr. İsmail ÖÇSOY
Erciyes University, Kayseri, Turkey

Assist Prof. Dr. Mehmet Fatih DİLEKOĞLU
Harran University, Şanlıurfa, Turkey

Dr. Lawali YABO DAMBAGİ
Kilis 7 Aralık University, Kilis, Turkey

Prof. Dr. Mustafa KURT
Kırşehir Ahiervan University, Kırşehir, Turkey

Assist Prof. Dr. Vijay M. TANGDE
Rashtrasant Tukadoji Maharaj Nagpur Uni., Nagpur

Prof. Dr. Hamit ALYAR
Çankırı Karatekin University, Çankırı, Turkey

Assoc. Prof. Dr. Mahmut TOPRAK
Bingöl University, Bingöl, Turkey

Prof. Dr. Mehmet UĞURLU
Muğla Sıtkı Koçman University, Muğla, Turkey

Prof. Dr. Ömer ŞAHİN
Siirt University, Siirt, Turkey

Prof. Dr. Murat ERTAŞ
Bursa Teknik University, Bursa, Turkey

Prof. Dr. Ahmet YARTAŞI
Çankırı Karatekin University, Çankırı, Turkey

Prof. Dr. Yahya GÜZEL
Erciyes University, Kayseri, Turkey

Prof. Dr. Bilal ACEMİOĞLU
Kilis 7 Aralık University, Kilis, Turkey

Prof. Dr. Esin Emine AKI YALCIN
Ankara University, Ankara Turkey

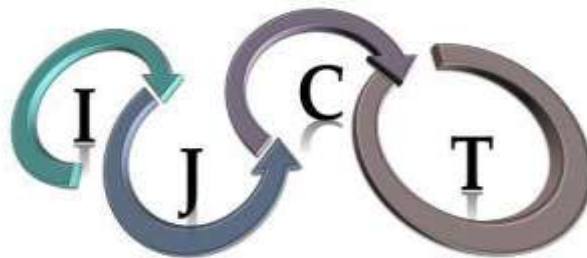
Assoc. Prof. Dr. Yunus ÖNAL
İnönü University, Malatya, Turkey

Prof. Dr. Ayşe ŞAHİN YAĞLIOĞLU
Amasya University, Amasya, Turkey

Assist. Prof. Dr. Muatsem BANİ-FWAZ
King Khalid University, Asir-Abha, Saudi Arabia

Prof. Dr. Atiqur RAHMAN
Islamic University, Kushita, Bangladesh

Prof. Dr. Kani ARICI
Kilis 7 Aralık University, Kilis, Turkey



International Journal of Chemistry and Technology

TABLE OF CONTENTS


Research Articles	Pages
1. Separation and determination of Pb (II) ions from aqueous media by cloud point extraction Pb (II) iyonlarının bulutlanma noktası ekstraksiyonu ile sulu ortamdan seçici olarak ayrılması ve tayini Yavuz SÜRME	103-108
2. Partial molar volumes and thermodynamic properties of alkali metal halides in 10% (w/w) 2-(Ethoxy) ethanol water mixture 10% (w/w) 2-(Etoksi) etanol-su karışımında alkali metal tuzların kısmi molar hacimleri ve termodinamik özellikleri T. Srinivasa MURTHY	109-120
3. Investigation dissolution behaviours and kinetics parameters of ulexite in boric acid solution Uleksitin borik asit çözeltisinde çözünme ve kinetik parametre davranışlarının incelenmesi Mehmet Harbi ÇALIMLI, Mehmet TUNÇ, Mehmet Muhtar KOCAKERİM	121-129
4. Preparation and characterization of activated carbon from almond shell by microwave-assisted using ZnCl ₂ activator ZnCl ₂ kullanılarak badem kabuğundan mikrodalga destekli aktif karbon üretimi ve karakterizasyonu Şirin Özlem TEĞİN, Ömer ŞAHİN, Orhan BAYTAR, Mehmet Sait İZGİ	130-137
5. Natural bond orbital (NBO) population analysis and non-linear optical (NLO) properties of 2-(azepan-1-yl(naphthalen-1-yl)methyl)phenol 2-(Azepan-1-il (naftalen-1-il) metil) fenolün doğal bağ orbital (NBO) popülasyon analizi ve doğrusal olmayan optik (NLO) özellikleri Yeliz ULAŞ	138-145
6. Synthesis of magnetic Fe ₃ O ₄ /AC nanoparticles and its application for the removal of gas-phase toluene by adsorption process Manyetik Fe ₃ O ₄ /aktif karbon nanoparçacıklarının sentezlenmesi ve adsorpsiyon prosesi ile gaz-fazındaki toluenin giderilmesi için uygulanması Sinan KUTLUAY, Mehmet Şakir ECE, Ömer ŞAHİN	146-155
7. Calculation of the infrared spectrum of 4-Cyanostyrene by Hartree-Fock (HF) and Density Functional Theory (DFT) 4- Siyanostirenin infrared spektrumunun Hartree-Fock (HF) ve yoğunluk fonksiyon teorisiyle (DFT) hesaplanması Kani ARICI, Rafet YILMAZ	156-161



8. Kinetic and analytical studies on pyrolysis of olive oil industry wastes 162-170
Zeytinyağı endüstrisi atıklarının pirolizi üzerine kinetik ve analitik çalışma
Gözde DUMAN TAC
9. Synthesis and characterization of a new 2D-imine-linked covalent organic framework 171-178
Yeni bir 2D-imin bağlı kovalent organik yapının sentezi ve karakterizasyonu
Lalehan AKYÜZ
10. Quantitative analysis of phenolic compounds of commercial basil cultivars (*Ocimum basilicum* L.) by LC-TOF-MS and their antioxidant effects 179-184
Ticari fesleğen çeşitlerinin (*Ocimum basilicum* L.) fenolik bileşiklerinin LC-TOF-MS ile kantitatif analizi ve antioksidan etkileri
Nusret GENC, Mahfuz ELMASTAŞ, İsa TELCİ, Ramazan ERENLER



Separation and determination of Pb (II) ions from aqueous media by cloud point extraction

 Yavuz SÜRME*

Department of Chemistry, Faculty of Science and Literature, Niğde Ömer Halisdemir University, Niğde 51240, Turkey

Received: 5 April 2020; Revised: 14 July 2020; Accepted: 16 July 2020

*Corresponding author e-mail: ysurme@ohu.edu.tr

Citation: Sürme, Y. *Int. J. Chem. Technol.* 2020, 4 (2), 103-108.

ABSTRACT

A simple, effective and highly selective cloud point extraction procedure was performed for enrichment of Pb (II) from aqueous matrix. The process depends on the formation of a stable complex between Pb (II) ions and Azure A compound at pH 6.0. The formed complex was extracted into micelle phase "Tergitol-NP7" at 25°C. This method was used for preconcentration of Pb (II) before its determination by FAAS. The values of limit of detection and limit of quantification were determined as 2.5 and 4.7 $\mu\text{g l}^{-1}$, respectively. The enrichment factor of the method was determined as 10 for 50 ml sample volume. Pb^{2+} analyte was quantitatively extracted and successfully determined in the presence of the most common foreign ions. The proposed method was then employed for the analysis of Pb (II) in natural and wastewater samples.

Keywords: Azure A, cloud point extraction, lead determination, TNP7.

Pb (II) iyonlarının bulutlanma noktası ekstraksiyonu ile sulu ortamdan seçici olarak ayrılması ve tayini

ÖZ

Pb (II) iyonlarının sulu ortamdan zenginleştirilmesi için basit, etkili ve oldukça seçici bir bulutlanma noktası ekstraksiyon prosedürü gerçekleştirilmiştir. Proses, pH 6.0' da Pb (II) iyonlarıyla Azure A bileşiği arasında kararlı bir kompleks oluşumuna bağlıdır. Oluşturulan kompleks 25°C'de "TNP7" misel fazı içerisine ekstrakte edilmiştir. Bu yöntem, Pb (II)'nin FAAS ile tayin edilmesinden önce önderiştirilmesi amacıyla kullanılmıştır. Tayin sınırı ve gözlenebilirlik sınırı değerleri sırasıyla 2,5 ve 4,7 $\mu\text{g l}^{-1}$ olarak belirlenmiştir. Yöntemin zenginleştirme faktörü, 50 ml numune hacmi için 10 olarak saptanmıştır. Pb^{+2} analiti, kantitatif olarak ekstrakte edilmiş ve en yaygın yabancı iyonların varlığında başarıyla tayin edilmiştir. Önerilen yöntem daha sonra doğal ve atık su numunelerindeki Pb (II) analizi için kullanılmıştır.

Anahtar Kelimeler: Azure A, bulutlanma noktası ekstraksiyonu, kurşun tayini, TNP7.

1. INTRODUCTION

Water is considered as an essential and valuable resource for all living organisms.^{1,2} The rapid development of industrial activities in the past few decades has caused pollution and reduced water quality. Industrial wastewaters can contain heavy metal ions such as lead, arsenic, mercury, nickel, cobalt and chromium.³ These heavy metals from various industries, such as metal coating industries, mining, tanneries, paint, batteries, fertilizers pollute the waters.⁴ Industrial waste containing contaminants can disrupt a huge harm to the aquatic ecosystem by deteriorating the

quality of both surface and ground waters and can cause serious damage and bad effects on the existing ecosystem.⁵ The atom electron shell structure of these heavy metals identifies their reactivity, complex forming tendencies, physical and biochemical activities.⁶

High concentration of the heavy metals with a certain value may cause serious health problems. The heavy metal toxicity may harm the central nervous activities, damage the liver, lungs, kidneys and some other main organs. Also longer exposure times may cause muscular dystrophy, Alzheimer's disease and several types of

cancer.⁷ Among these heavy metals, lead is a toxic and non-biodegradable metal which is employed in industries such as vehicle manufacture, lubricants, additives, brake pads, tires, insecticides, ceramic products, batteries and dyes.⁸

Exposure to lead may cause the cancer, anaemia, kidney disease, and mental retardation. Lead adversely affects nervous system, gastro-intestinal track, kidneys, reproductive system and also cause encephalopathy, neuro-behavioral deficits.⁹ Due to all these adverse effects, the determination of heavy metals in waters is of prime importance for human and environment health.¹⁰ Consequently, many technologies such as adsorption,¹¹ chemical precipitation,¹² flocculation,¹³ ion exchange and membrane filtration.¹⁴ have been used for the determination and removal of Pb(II) ions from wastewater samples.

The cloud point extraction (CPE) technique is one of the most effective techniques for preconcentration of trace metals because of its simplicity, rapidity and environmental compatibility.¹⁵ This technique is based on the phase separation formed in aqueous solutions of non-ionic surfactants which becomes cloudy when heated to a known temperature called as the cloud point temperature (CPT). This causes to the form of two separate phases. The first phase contains the analytes surrounded by surfactants (water insoluble surfactant-rich phase) and the aqueous phase that contains matrix ions. The total volume of the surfactant containing rich phase is much smaller than the aqueous one and that allows very high preconcentration factors for analytes.¹⁶

In literature, there are studies focused on preconcentration and determination of heavy metal ions based on CPE method. CPE has been used for the preconcentration of lead, after the formation of a brilliant cresyl blue dye and the lead has been analysed by flame atomic absorption spectrometry (FAAS) using surfactant TritonX-114,¹⁶ There are also simultaneous preconcentration and determination studies with CPE method. For example, various metals such as copper manganese and nickel have been simultaneously extracted after their complexation with 2-amino-6-(1,3-thiazol-2-diazeyl)-phenol at pH 7¹⁷ and analysed by FAAS, using TritonX-114 as the surfactant.

In this study a highly selective cloud point extraction procedure for separation, preconcentration and determination of Pb (II) ions as its Azure A complex in wastewater samples was developed. Determination of Pb (II) ions were performed by FAAS. The optimum conditions for quantitative recoveries were investigated.

According to our literature survey, the combination of Azure A and Tergitol NP7 for lead preconcentration has not been used before in cloud point extraction.

2. MATERIALS AND METHODS

2.1. Reagents and solutions

The non-ionic surfactant Tergitol NP7 was purchased from Sigma Aldrich. A 1×10^{-3} mol l⁻¹ of Azure A complexing agent solution was prepared by dissolving appropriate amount of Azure A in distilled water. Pb²⁺ stock standard solution was prepared by dissolving pure Pb(NO₃)₂ in distilled water. Pb²⁺ solutions with different concentrations were prepared by diluting from the stock solution. Phosphate and citrate buffer solutions were prepared and used in the experiments. The calibration curves have correlation coefficients of 0.999. A sample of the calibration curve used in the experiments is given in Figure 1.

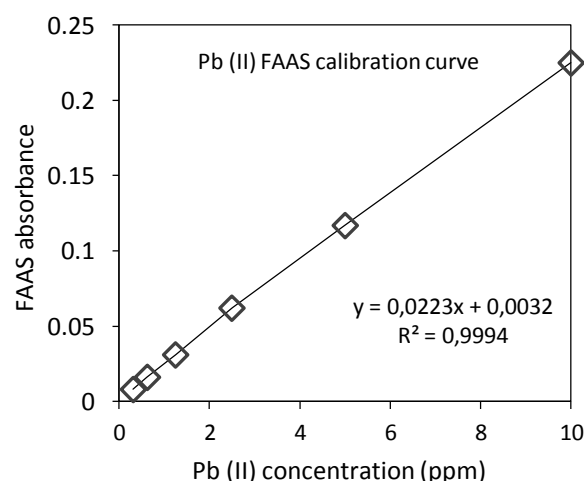


Figure 1. Calibration curve of Pb (II) used in the experiments.

2.2. Apparatus

The absorbance values of Azure A and Pb (II)–Azure A complex were determined by using Shimadzu UV–160A ultraviolet/visible spectrophotometer. The atomic absorbance values of Pb (II) ions were measured by using Shimadzu AA 7000 flame atomic absorption spectrometer and a lead hollow cathode lamp. The atomic absorption signal of Pb was measured as a peak height versus analytical curve. A Nuve BM 402 model thermostatic bath (Nuve Ltd. Turkey) was used to obtain the desired cloud point temperatures. The phase separations were performed by a Nuve NF 400 model centrifuge. The pH measurements of the solutions were conducted by a WTW level 1 model pH meter.

2.3. CPE test procedure

The cloud point extraction procedure was operated by using the designed model test solutions. A 40 ml of test solution containing 25 mg Pb (II) ions were transferred into a plastic tube. A 0.35 ml of Azure A solution of $1 \times 10^{-3} \text{ mol l}^{-1}$, a 0.5 ml of 2% (v/v) TNP7 surfactant, and a 4.0 ml of buffer solutions of pH 6 were added on it. The centrifuge tube was filled with covered. After shaking the final solution, taken into a thermostatic bath at 30°C for 10 min. Then this solution was centrifuged to separate Pb(II)–Azure A metal chelates from the other matrix at 4000 rpm for 5 min. The aqueous phase was removed and the highly viscous surfactant rich phase was dissolved by adding 1.0 ml, $1 \text{ mol l}^{-1} \text{ HNO}_3$ in methanol. This final solution was transferred into a 5 ml volumetric flask and the original tube washed with small aliquots of $1 \text{ mol l}^{-1} \text{ HNO}_3$ in methanol. The final dilution was to 5 ml. The Pb (II) concentration of the final solution was measured by FAAS. All experiments were conducted triplicate.

3. RESULTS AND DISCUSSION

The optimization of the method was examined by changing one variable at a time concept. The main analytical parameters such as solution pH, concentrations of chelating agent and surfactant, incubation time, experiment temperature, sample volume, and matrix ions were optimized.

3.1. The UV-Visible spectrum of Azure A and Pb (II)–Azure chelates

Azure A (3-amino-7-(dimethylamino)phenothiazin-5-ium chloride) is a sulphur and nitrogen containing water soluble organic dye used in industry and some scientific researches about corrosion inhibitors.¹⁸⁻²⁰ In this study, it is used as a chelating agent. The chemical structure and UV-Vis spectrum of aqueous Azure A solution and Pb (II)–Azure A complex solution are given in Figure 2.

According to UV-Vis. spectra of Azure A and Pb(II)–Azure A complex, three absorption bands are observed at 240 nm, 290 nm and 630 nm. These bands are identical both for dye and complex. On the other hand, the band at 210 nm was appeared after mixing the Pb(II) and Azure A. This can be considered as an evidence to the formation of the Pb(II)–Azure A complex.

3.2. Effect of Solution pH

In the CPE method, the pH value of the solution constitutes one of the most important steps in the extraction of Pb (II) ions. Because, the metal chelating capability and the stability of the Pb(II)–Azure A complex directly effects the extraction efficiency, and Solution pH is also the main reason for changing them.

To gain the optimum extraction efficiency, the solution pH was investigated between pH 2–8 which is adjusted by using phosphate, ammonium and acetate buffer solutions. The results are given in Figure 3.

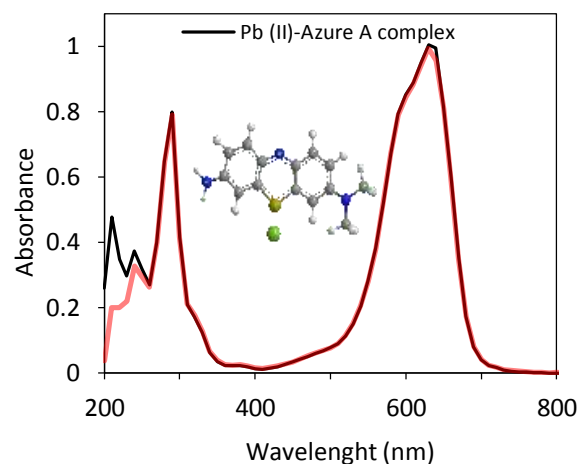


Figure 2. The 3D chemical structure and UV/Vis. spectrum of aqueous Azure A and Pb (II)–Azure A complex.

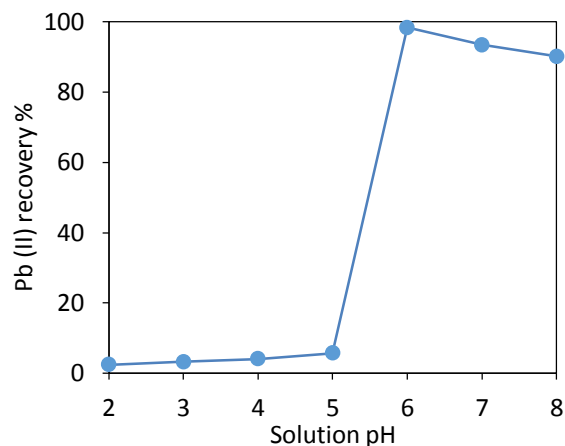


Figure 3. Recovery of Pb(II) ions at different solution pHs.

The optimum recovery value was obtained at pH 6 as given in Figure 3. Consequently, pH 6 value was selected as the most appropriate solution acidity and therefore rest of the experiments were performed at pH 6.

3.3. Concentration of Azure A ligand

Figure 2 clearly indicates that Pb (II) ions and Azure A molecules form a complex. Therefore, the effect of Azure A concentration on the CPE recovery of Pb (II) ions was investigated using volumes from 0.05 to 0.6 ml for solution of $1 \times 10^{-3} \text{ mol l}^{-1}$.

The results are shown in Figure 4. From Figure 4, it is clearly seen that the recovery of Pb (II) ions increases up to 98.2% at 0.35 ml of Azure A and remains stable after this value. So, the 0.35 ml of Azure A was selected for preconcentration of Pb(II) ions for further experiments.

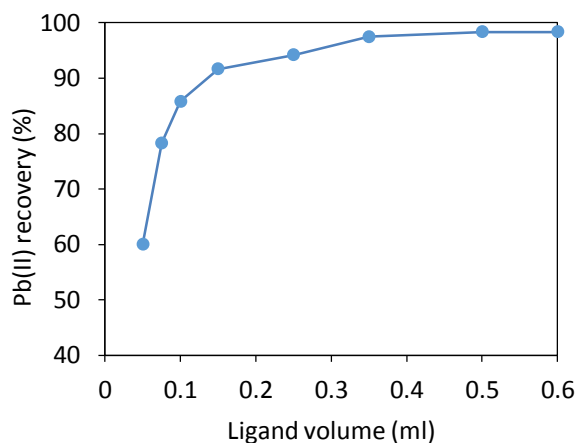


Figure 4. Effect of Azure A volume on the recovery of Pb(II) ions at pH 6.

3.4. Effect of surfactant concentration

In the CPE method, for extraction of Pb(II), choosing an appropriate surfactant and optimization of its concentration is important. Therefore, the effect of TNP-7 surfactant concentration on the CPE recovery of Pb(II) ions was studied using volumes between 0.10 and 3.0 ml from 2% stock solution. The results obtained are given in Figure 5.

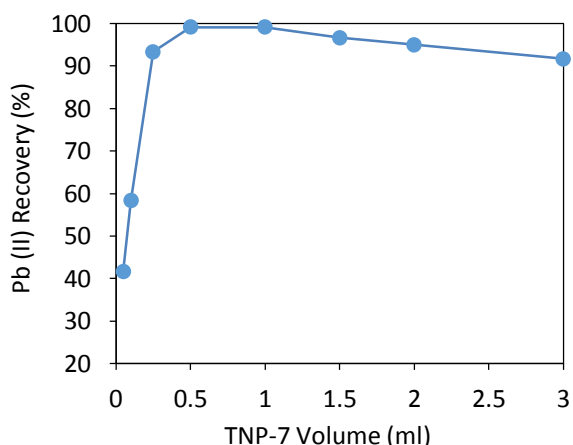


Figure 5. Effect of surfactant concentration on the recovery of Pb(II) ions for 0.35 ml Azure A at pH 6.

As it can be seen from the Figure 5, a 0.5 ml of TNP-7 surfactant is optimum for the quantitative recovery of

Pb(II) ions (99.2%). Therefore, a surfactant volume of 0.5 ml was chosen as optimum and the further studies were conducted with 0.5 ml of TNP-7.

3.5. Effect of temperature

Optimizing the temperature of the CPE medium is of prime importance to gain high extraction efficiency and to avoid insufficient phase separation. In CPE analysis, it is necessary to use a low extraction temperature as the temperature affects both the stabilization of metal complexes and the separation of the surfactant-rich phase from the aqueous medium. The surfactant TNP-7 used in this study has a very low cloud point temperature (CPT = 20°C) than other non-ionic surfactants. This allows a very low phase separation temperature and prevents energy consumption. The effect of the temperature was analyzed by varying from 20 to 60°C, and the results showed that the extraction efficiencies were quantitative and stable for temperatures up to 45°C and then decreased (Figure 6). This decrease can be attributed to the lower stability of Pb(II)–Azure A complex at high temperatures. As a result, the 25°C was applied as optimum value for further experiments.

3.6. Effect of interfering ions

The Azure A organic compound was used as chelating agent to bind with Pb(II) ions. However, the possibility of its complexing with several transition metals, alkaline, alkaline-earth and other ions in aqueous media was investigated at pH 6. The tests were made with each ion separately. Obtained results are given in Table 1.

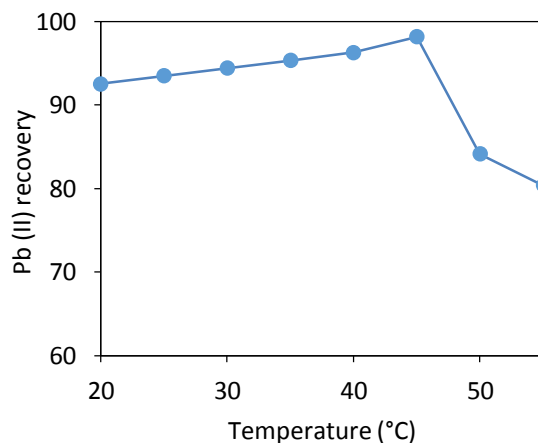


Figure 6. Effect of temperature on the recovery of Pb(II) ions.

The consequences in Table 1 clearly indicate that there is no significant effect of interfering ions on the

quantitative recovery of Pb(II). Therefore, the CPE method can safely be applied for preconcentration and determination of lead ions in aqueous media and can be detected by FAAS.

The selectivity of the Azure A complexing agent was also studied in the presence of other chelatable transition metal ions such as Cu(II), Cd(II) and Ni(II) to prove the selectivity for all pH values. The results obtained are given in Figure 7.

Table 1. Effect of interfering ions on the recovery of Pb(II) ions for 0.35 ml Azure A at pH 6

Ion	Added as	Concentration (mg l ⁻¹)	% recovery Pb(II)
Mn ²⁺	Mn(NO ₃) ₂ ·4H ₂ O	50	96 ± 3 ^a
Cr ³⁺	Cr(NO ₃) ₃ ·3H ₂ O	50	95 ± 1
Al ³⁺	Al(NO ₃) ₃ ·9H ₂ O	50	95 ± 2
Bi ³⁺	Bi(NO ₃) ₃ ·5H ₂ O	100	96 ± 3
Na ⁺	NaNO ₃	1000	98 ± 4
K ⁺	KNO ₃	1000	97 ± 4
Ca ²⁺	CaCl ₂	1000	96 ± 3
Mg ²⁺	Mg(NO ₃) ₂ ·6H ₂ O	1000	95 ± 2

^aMean ± standard deviation

The tolerable concentrations of the interfering ions were selected as difference in the analytical signal of Pb(II) which is not higher than 5%, when compared with the signal of 5.0 µg l⁻¹ Pb(II) in isolated solution. Figure 7 explains there is no possible competitive chelating effect at any pH which may reduce the potential complexing between Azure A and lead ions and decrease the recovery of Pb(II) ions.

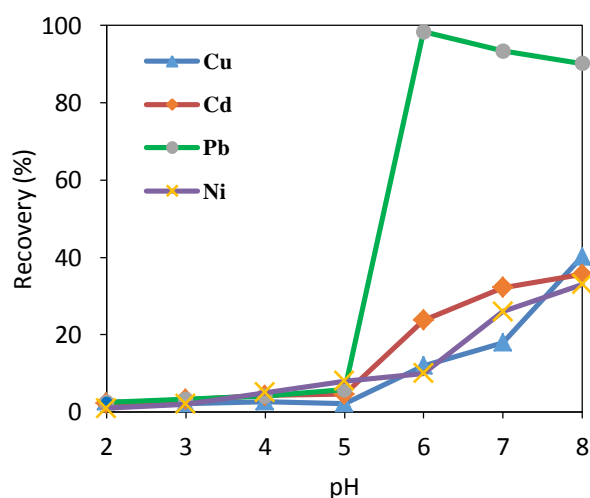


Figure 7. Effect of other metal ions on the recovery of Pb(II) ions for 0.35 ml Azure A and 0.5 ml TNP-7 at pH 6.

3.7. Analytical performance of the CPE method

The analytical characteristics of the cloud point extraction method such as preconcentration factor, limit of detection and quantification were determined. The results obtained are given in Table 2. The limit of quantification (LOQ) and the limit of detection (LOD) were defined as $LOQ = 10 Sd/m$ and $LOD = 3 Sd/m$, respectively (where m is the slope of calibration curve, Sd is the average standard deviations of 21 blank solutions. The relative standard deviation (RSD) was found by using ten replicate measurements of standard solutions of Pb (II).

Table 2. Analytical characteristics of the method

Parameters	Pb(II)
Limit of detection, µg l ⁻¹	2.5
Limit of quantification, µg l ⁻¹	4.7
Preconcentration factor	10
Relative standard deviation, %	4
Calibration curve	$A = 0.0223C + 0.0032$
Correlation coefficient, R ²	0.9994

3.8. Real sample analysis

Analyte addition tests for Pb(II) ions were performed on two natural and one industrial waste water samples to validate the optimized method. pH of samples was adjusted to 6 and the CPE procedure was applied to samples and the results are given in Table 3.

Table 3. Analyte addition-recovery test in different water samples by developed CPE method (N = 3)

Samples	Pb		
	Added (µg)	Found (µg)	Recovery (%)
Natural spring water I	-	BDL	-
	5.0	5.09 ± 0.28^a	102 ± 4
	10.0	9.78 ± 0.23	98 ± 2
Natural spring water II	-	BDL	-
	5.0	5.12 ± 0.19	102 ± 2
	10.0	10.15 ± 0.44	101 ± 3
Factory wastewater	-	BDL	-
	5.0	5.05 ± 0.36	101 ± 4
	10.0	10.22 ± 0.47	102 ± 5

^aMean ± standard deviation, BDL: Below detection limit

4. CONCLUSIONS

An effective and highly selective cloud point extraction method was established for the preconcentration of Pb(II) ions in natural and waste water samples prior to their flame atomic absorption spectrophotometric determination. The results revealed that the Azure A ligand was highly selective for Pb(II) ions between pH 5 and pH 8 region. The pH studies showed that the recovery values of the Pb(II) was quantitative in the presence of Cu(II), Cd(II) and Ni(II) ions under the same circumstances. It was concluded that this

phenomenon could be explained by the affinity of the Azure A ligand to Pb (II) ions. It was also obvious that this tendency was because of the chemical compatibility between the Azure A and Pb(II). The proposed method is inexpensive and easy to operate. The analytical performance of the method in the presence of interfering ions was excellent for the detection of Pb (II) ions. As a result, the developed method may be considered as a useful tool for preconcentration and determination of Pb(II) in water samples for routine quality controls.

Conflict of interests

I declares that there is no a conflict of interest with any person, institute, company, etc.

REFERENCES

- Verma, B.; Balomajumder, Y. *Environ. Techn. Innov.* **2020**, 17, 100596-10610.
- Vakili, M.; Deng, S.; Cagnetta, G.; Wang, W.; Meng, P.; Liu, D.; Yu, G. *Sep. Purif. Technol.* **2019**, 224, 373-387.
- Wang, R.; Liang, R.; Dai, T.; Chen, J.; Shuai, X.; Liu, C. *Trends Food Sci. Techn.* **2019**, 91, 319-329.
- Yadav, V.B.; Gadi, R.; Kalra, S. *J. Environ. Manage.* **2019**, 232, 803-817.
- Wadhawan, S.; Jain, A.; Nayyara, J.; Mehta, S.K. *J. Water Process Eng.* **2020**, 33, 101038-101055.
- Burakov, A.E.; Galunina, E.V.; Burakova, I.V.; Kucherova, A.E.; Agarwal, S.; Tkacheva, A.G.; Gupta, V.K. *Ecotox. Environ. Safe.* **2018**, 148, 702-712.
- Vardhan, K.H.; Kumar, P.S.; Panda, R.C. *J. Mol. Liq.* **2019**, 290, 111197-111219.
- Ghorbani, M.; Seyedin, O.; Aghamohammadhassan, M. *J. Environ. Manage.* **2020**, 254, 109814-109919.
- Ramola, S.; Belwal, T.; Li, C.J.; Wang, Y.Y.; Luc, H.H.; Yang, S.M.; Zhou, C.H. *Sci. Total Environ.* **2020**, 709, 136171-136183.
- Biata, R.N.; Mashile, G.P.; Ramontja, J.; Mketi, N.; Nomngongo, P.N. *J. Food Compos. Anal.* **2019**, 76, 14-21.
- Alsuhybani, M.; Alshahrani, A.; Algamdi, M.; Al-Kahtani, A.A.; Alqadami, A.A. *J. Mol. Liq.* **2020**, 301, 112393-112494.
- Zhang, P.; Ouyang, S.; Li, P.; Sun, Z.; Ding, N.; Huang, Y. *J. Clean. Prod.* **2020**, 246, 118728-118740.
- Pang, F.M.; Kumar, P.; Teng, T.T.; Omar, A.K.; Wasewar, K.L. *J. Taiwan Inst. Chem. E.* **2011**, 42, 809-815.
- Berber, Y.; Hammache, Z.E.; Bensaadi, S.; Soukeura, R.; Amara, M.; Bruggen, B. *J. Water Process Eng.* **2019**, 32, 100953-100960.
- Jalbani, N.; Soylak, M. *J. Ind. Eng. Chem.* **2015**, 29, 48-51.
- Surme, Y.; Narin, I.; Soylak, M.; Yuruk, H.; Dogan, M. *Microchim. Acta*, **2007**, 157, 193-199.
- Sheikh, R.E.; Shaltout, M.; Nabawy, K.E.; Gouda, A.A. *Anal. Bioanal. Chem. Res.* **2020**, 1, 49-60.
- Özkır, D. *Int. J. Electrochem.* **2019**, 1, 1-11.
- Özkır, D. *Int. J. Chem. Technol.* **2019**, 3, 17-25.
- Özkır, D.; Kayakırılmaz, K.; Bayol, E.; Gürten, A.A.; Kandemirli, F. *Corros. Sci.* **2012**, 56, 143-152.



Partial molar volumes and thermodynamic properties of alkali metal halides in 10% (w/w) 2-(Ethoxy) ethanol water mixture

T. Srinivasa MURTHY

Sanjay Ghodawat JEE-NEET Academy, Sanjay Ghodawat University
Atigre 416118, Kolhapur (M.H)-India

Received: 24 April 2020; Final revised: 28 July 2020; Accepted: 30 July 2020

*Corresponding author e-mail: vasuchemistry@gmail.com

Citation: Murthy, T. S. *Int. J. Chem. Technol.* 2020, 4 (2), 109-120.

ABSTRACT

Apparent molar volumes of alkali metal halides in 10% (W/W) 2-(Ethoxy) ethanol-water mixture were calculated from the measured densities at 303.15K, 308.15K and 313.15K. Using Masson equation the partial molar volumes were obtained which are further divided into ionic components adopting the methods of Conway and Jolicoeur. A comparison of values of ionic partial molar volumes of alkali metal and halide ions with the values reported in pure water indicates a decrease in hydrophobic hydration, which may be due to the addition of co-solvent 2-(Ethoxy) ethanol. The conclusions drawn from viscosity studies confirm that the structure of water is reduced by the breaking of hydrogen bonds in 2-(Ethoxy) ethanol-water mixture. For all the ions, the \bar{V}_{ion}^0 values are divided into \bar{V}_{stru}^0 and \bar{V}_{cage}^0 . Using the Padova's equation, the \bar{V}_{intr}^0 values of alkali metal salts were calculated and further divided into ionic contributions. Calculated dimensions of ions show that the classification of alkali metal halide salts into structure makers and structurebreakers based on the sign of $\bar{V}_{ion}^0 - \bar{V}_{cryst}^0$ is not valid for the present solvent system.

Keywords: Molar volumes of electrolytes, alkali metal salts, 2-(Ethoxy) ethanol, liquid mixtures, solute-solvent interactions.

10% (w/w) 2-(Etoksi) etanol-su karışımında alkali metal tuzların kısmi molar hacimleri ve termodinamik özellikleri

ÖZ

10% (w/w) 2-(Etoksi) etanol-su karışımlarında alkali metal tuzların gözlenen molar hacimleri 303.15 K, 308.15 K and 313.15 K' de ölçülen yoğunluklardan hesaplandı. Masson denklemini kullanarak, Conway ve Jolicoeur yöntemlerini benimseyen iyonik bileşenlere ayrılan kısmi molar hacimler elde edildi. Alkali metal ve halojenür iyonların iyonik kısmi molar hacimlerinin saf suda bildirilen değerlerle karşılaştırılması, hidrofobik hidrasyonda bir düşüşe işaret etmektedir ki bu yardımcı çözücü 2- (Etoksi) etanolün eklenmesinden kaynaklanabilir. Viskozite çalışmalarından elde edilen sonuçlar, 2- (Etoksi) etanol-su karışımında hidrojen bağlarının kırılmasıyla suyun yapısının azaldığını doğrulamaktadır. Tüm iyonlar için, \bar{V}_{ion}^0 değerleri \bar{V}_{stru}^0 and \bar{V}_{cage}^0 ' e ayrılır. Padova denklemini kullanarak, alkali metal tuzlarının \bar{V}_{intr}^0 değerleri hesaplandı ve ayrıca iyonik katkılara bölündü. iyonların hesaplanan boyutları, alkali metal halojenür tuzlarının $\bar{V}_{ion}^0 - \bar{V}_{cryst}^0$ işaretine göre yapı oluşturalara ve yapı kırıcılara sınıflandırılmasının mevcut çözücü sistemi için geçerli olmadığını göstermektedir.

Anahtar Kelimeler: Elektrolitlerin kısmi molar hacimleri, alkali metal tuzlar, 2-(Etoksi) etanol, liquid mixtures, çözücü-çözünen etkileşimleri.

1. INTRODUCTION

Water-organic mixed solvents have been the subject of intense research conducted by many researchers all over the world. Knowledge of their structures and properties

is very important on account of their application in various areas of chemistry and modern technologies.¹ Ion-ion and ion-solvent interactions are notable among the interactions that occur in solutions since these are connected with the physical and chemical properties of

the mixtures. Studies on thermo-chemical properties and transport properties such as viscosity, refractive index, ultrasonic velocity, adiabatic compressibility, density and conductivity of ionic solutions help to characterize the structures and properties of the solutions.²⁻⁵

n-(Alkoxy) ethanols also known as cello solves are good industrial solvents which are used as a component of solvents and co-emulgators and stabilizers of emulsion paints, lacquers and plastics. Cello solves are used as additives to gasoline due to their Octane enhancing and pollution-reducing properties.⁶ n-Alkoxy alkanols are in fact monoalkyl ether of ethylene glycol. Therefore, its physicochemical properties are probably between dipolar aprotic and protic solvents. Previous studies have shown that they exist as molecular dispersion in water at low concentration of 2-alkoxy ethanol (at high concentration micelle-like aggregation occurs). It would be interesting to study the electrolyte behavior in such an uncharacteristic solvent medium. The study of thermal and transport properties of electrolytes in solutions would help indicate the use of cellosolves in various technologies like high energy batteries and ion exchangers.⁷ Despite the potential applications of these solvents, there are relatively few solute-solvent interaction studies on substances in this class and their water mixtures. 2-(Butoxy)-ethanol and 2-(Methoxy)-ethanol are the solvents studied to some extent.⁸⁻¹⁴

Thermo chemical properties of electrolyte solutions in 2-alkoxyethanol-water mixtures have been reported with an emphasis on solution enthalpies. However no specific work has been reported so far on transport and quasi thermodynamic properties of electrolytes in 2-(Ethoxy)-ethanol water mixtures where some modifications are expected in the structure of water. The objective in selecting a 10% (W/W) 2-(Ethoxy) ethanol-water mixture in the present investigation is that the water-rich liquid mixtures are more economical and facilitates the desired properties required for the industry.

The purpose of the present study is to study the density, molar volumes and thermodynamic parameters of alkali metal halide salts in a 10% (W/W) 2-(Ethoxy) ethanol-water mixture. For this, it is aimed to do the following:

- (i) To probe into the effect of temperature on the solvation process.
- (ii) To study the effect of increasing both cation and anion size.
- (iii) To compare the partial molar volumes of alkali

metal salts with partial molar volumes and thermodynamic parameters of our previous work related to tetra alkyl ammonium bromides in the same 10% (W/W) 2-(Ethoxy) ethanol-water mixed solvent medium.⁹

2. EXPERIMENTAL

Sodium chloride, potassium chloride and potassium iodide (Sarabhai Chemicals G. R. grade), rubidium chloride (E.Merk analar grade) and potassium bromide (LOBA Chemie G. R. grade) were dried at 110°C in a hot air oven and stored in a desiccator. Electrolyte solutions of desired concentrations were prepared each time by mass with a precision of ± 0.0001 g.

2-(Ethoxy)-ethanol (E.Merk sample) was first refluxed for an hour with Tin II chloride to remove the traces of peroxide as per the procedure discussed in my earlier communication.¹² The refluxed solvent was then dried over anhydrous potassium carbonate and then fractionally distilled. The middle fraction distilling between 133-134°C was collected. 10% 2-(Ethoxy) ethanol-water mixture was prepared weight by weight. A bicapillary pycnometer of parker and parker type with minor modifications was used to determine densities. The uncertainty of the density measurements (95% confidence limits) was $\pm (8 \times 10^{-5})$ g cm⁻³. The density value we measured at 298.15 K for pure 2-Ethoxy ethanol is 0.92407 g cm⁻³ which is in reasonable agreement with literature value: 0.9253 g cm⁻³.¹⁵

3. RESULTS AND DISCUSSION

The experimentally measured densities of alkali metal halide salt solutions of 10% (w/w) 2-(ethoxy) ethanol-water mixture at 303.15 K, 308.15 K and 313.15 K (temperature control was monitored to ± 0.001 K) were used to calculate the apparent molar volumes by using the equation where all the terms have their usual significance.¹⁶ The densities along with the apparent molar volumes of the alkali metal halides are presented in Table 1.

$$\phi_V = \frac{M}{d_0} + \frac{1000(d_0 - d)}{d_0} \quad (1)$$

The Debye-Huckel theory serves as a basis for the extrapolation of ϕ_V to infinite dilution. The recommended procedure for the extrapolation of ϕ_V to infinite dilution employs the Redlich-Meyer equation.⁷

Table 1. Density (d) and apparent molar volume (ϕ_v) of alkali metal halides in 10% (w/w) 2-(Ethoxy) ethanol-water mixture at 303.15 K, 308.15 K and 313.15 K

303.15 K			308.15 K			313.15 K		
$c \times 10^3$	d	ϕ_v	$c \times 10^3$	d	ϕ_v	$c \times 10^3$	d	ϕ_v
NaCl								
22.01	0.99636	13.0768	22.01	0.99436	12.6459	22.01	0.99215	15.4235
30.31	0.99672	13.6437	38.39	0.99504	14.5247	38.39	0.99284	15.8702
41.39	0.99720	14.0600	41.39	0.99518	14.3318	54.35	0.99348	16.6462
53.89	0.99774	14.3526	54.35	0.99568	15.6840	63.79	0.99386	16.8995
61.66	0.99805	14.8928	63.79	0.99606	16.0738	70.89	0.99414	17.1280
70.89	0.99840	15.6393	70.89	0.99630	16.9490	83.92	0.99462	17.3540
78.71	0.99871	15.9628	83.92	0.99684	16.9757	94.73	0.99510	17.4338
94.70	0.9993	16.9235	94.73	0.99728	17.0772	104.91	0.9955	17.6175
104.90	0.9997	17.1669	104.91	0.99766	17.4835	112.03	0.99580	17.5440
112.03	1.00004	16.7532	112.03	0.99804	16.6973			
KCl								
28.30	0.99678	24.4969	28.30	0.99474	25.6137	28.30	0.99258	26.0257
41.20	0.99740	25.1662	41.20	0.99534	26.4348	41.20	0.99318	26.7370
52.00	0.99786	26.6055	52.00	0.99584	26.8539	52.00	0.99366	27.4942
61.70	0.99835	26.2214	61.70	0.99630	26.9270	61.70	0.99410	27.8030
71.20	0.99880	26.3678	71.2	0.99674	27.1280	71.20	0.99450	28.4621
82.20	0.99930	26.7523	82.2	0.99703	27.5412	82.20	0.99540	28.5828
91.04	0.9997	27.0139	91.04	0.99760	27.8427	91.04	0.99500	28.6788
100.09	1.00011	27.2291	100.09	0.99805	27.7870	100.09	0.99584	28.4521
110.50	1.00061	27.2179	110.60	0.99852	28.0012	110.6	0.99630	28.7004
119.6	1.00102	27.3626	119.60	0.99892	28.1754	119.60	0.99670	28.8270
RbCl								
21.11	0.99732	28.224	21.11	0.99532	27.804	21.11	0.99310	31.167
29.59	0.99808	29.152	29.59	0.99608	28.871	29.59	0.99384	32.002
40.60	0.99902	30.936	40.60	0.99709	29.015	40.60	0.99482	32.059
50.98	0.99993	31.443	50.98	0.99796	30.717	50.98	0.99574	32.158
61.10	1.00082	31.725	61.10	0.99883	31.460	51.10	0.99663	32.354
70.50	1.00165	31.858	70.50	0.99964	31.932	70.50	0.99745	32.574
80.02	1.00248	32.111	80.02	1.00048	32.050	80.02	0.99828	32.750
90.80	1.00342	32.323	90.80	1.00143	32.167	90.80	0.99919	33.237
108.90	1.00500	32.569	108.90	1.00303	32.266	108.90	1.00077	33.355
120.40	1.00601	32.636	120.40	1.00404	32.368	120.40	1.00176	33.527
KBr								
30.50	0.99786	36.557	30.50	0.99587	36.631	30.50	0.99366	37.373
39.86	0.99864	35.381	39.86	0.99664	36.705	39.86	0.99443	37.302
49.15	0.99949	35.750	49.75	0.99749	36.034	49.75	0.99522	37.735
61.40	1.00046	35.789	61.40	0.99845	36.189	61.40	0.99618	37.519
70.48	1.00126	35.178	70.48	1.00012	35.249	70.48	0.99699	36.615
80.80	1.00211	35.388	80.80	1.00100	35.459	80.80	0.99783	36.785
90.50	1.00301	34.419	90.50	1.00179	35.488	90.50	0.99870	36.013
100.87	1.00385	34.806	100.87	1.00256	35.515	100.87	0.99956	36.053
109.90	1.00453	35.097				109.90	1.000296	36.200
KI								
20.90	0.9975	50.936	20.90	0.99578	48.631	20.90	0.99359	49.221
31.82	0.99903	50.279	31.82	0.99106	48.800	31.82	0.99490	48.273
40.08	1.00000	49.975	40.08	0.99807	47.816	40.08	0.99588	48.973
51.16	1.00136	48.566	51.76	0.99939	47.681	51.16	0.99720	47.983
60.30	1.00246	48.158	60.30	1.00047	47.755	60.30	0.99830	47.693
72.56	1.00395	47.571	72.56	1.00195	47.390	72.56	0.99978	47.355
80.57	1.00494	47.078	80.57	1.00288	47.674	80.57	1.00077	46.902
89.85	1.00607	46.807	89.85	1.00404	47.014	89.85	1.00190	46.668
102.27	1.00749	47.427	102.27	1.00559	46.343	102.27	1.00337	46.839
120.24	1.00967	47.051	120.24	1.00768	46.895	120.24	1.00552	46.831

Units: Molarity as $c \times 10^3 = (\text{mol dm}^{-3})$; $d = \text{kg m}^{-3}$; $\phi_v = (\text{cm}^3 \text{mol}^{-1})$

Table 2. Apparent molar volume at infinite dilution (ϕ_V^0) and the experimental slope (S_V^*) of electrolytes in 10% (w/w) 2-(OEt) EtOH-H₂O 303.15 K, 308.15 K and 313.15

Salt	303.15 K		308.15 K		313.15 K	
	ϕ_V^0 (cm ³ mol ⁻¹)	S_V^* (cm ³ mol ^{-3/2})	ϕ_V^0 (cm ³ mol ⁻¹)	S_V^* (cm ³ mol ^{-3/2})	ϕ_V^0 (cm ³ mol ⁻¹)	S_V^* (cm ³ mol ^{-3/2})
NaCl	9.55	22.67	9.71	24.01	13.59	12.79
KCl	22.33	15.23	23.56	13.60	23.79	15.50
RbCl	26.08	20.70	24.85	23.87	29.84	10.65
KBr	37.76	-9.184	38.167	-8.87	39.569	-10.459
KI	53.92	-22.03	50.28	-10.65	50.70	-12.37

$$\phi_V = \phi_V^0 + S_V^* C^{1/2} + q_V C \quad (2)$$

Where S_V is the theoretical limiting slope and q_V is a constant. However the calculation of a numerical value for S_V requires knowledge of pressure dependence of dielectric constant, which is not available for the present solvent system under investigation. For this reason, the Masson empirical equation of the form given below has been used for extrapolating the ϕ_V to an infinite dilution where S_V^* is an experimental slope.

$$\phi_V = \phi_V^0 + S_V^* C^{1/2} \quad (3)$$

According to Masson's equation, the apparent molar volumes should vary linearly with square root of concentration of the salt and the data shall fit into Masson's relation.¹⁸ The linear relation has been known to be followed by many small strong electrolytes in dilute solutions and to moderate concentrations for some other salts as well.¹⁹ Values of ϕ_V & S_V^* obtained by the method of least squares are presented in **Table 2**. In all cases studied, ϕ_V vary linearly with \sqrt{C} at all temperatures as shown in **Figures 1-3**. S_V^* values indicate the data available in different solvents including water, leads one to conclude that, in general, negative slope is favored; (i) if the dielectric constant of the medium is high, whether the solvent is hydrogen-bonded or non-hydrogen bonded. (ii) if electrostatic ion-ion interactions are weak due to large ion-size or due to very high dielectric constant.

On the other hand, a positive slope is observed if ion-ion interactions are strong due to the low dielectric constant of the medium or due to small ionic size. S_V^* values were found as positive at all temperatures for NaCl, KCl and RbCl indicating the presence of ion-ion interactions, even though the dielectric constant of the

medium is moderately high. In contrast, the negative slope was observed for KBr and KI salts, which were not unexpected due to the larger ionic size and in a medium of moderately high dielectric constant. This indicates that the strong ion-solvent interactions weaken the ion-ion interactions.

3.1. The limiting partial molar volumes (ϕ_V^0)

The limiting partial molar volume of solutes is regarded as a measure of solute-solvent interactions by many workers.^{20,21} In the present study, ϕ_V^0 values of alkali metal halides exhibit the order $Rb^+ > K^+ > Na^+$ at all temperatures studied. This shows that the structure breaking effect or solute-solvent interactions decrease in the order $Na^+ > K^+ > Rb^+$ for cations. A similar trend has been reported in the study of partial molar volumes of alkali metal halides in tertiary butanol-water mixtures by Desnoyers.²¹

On the other hand, the order of ϕ_V^0 concerning anions follows the $I^- > Br^- > Cl^-$ which in turn indicates that structure breaking effect decreases in the order $Cl^- > Br^- > I^-$. The comparatively small ϕ_V^0 values for sodium chloride can reasonably be explained based on the small size of the cation which causes greater electrostriction and thus gives small ϕ_V^0 values.

Many researchers have inferred that the maxima in plots of ϕ_V^0 versus t (in °C) indicate the presence of strong solute-solvent interactions, while the minima suggest the presence of ion-ion interactions.²⁰⁻²⁶ In the case of rubidium chloride, a deep minima was observed, indicating the presence of ion-ion interaction also supported by positive S_V^* values. For other salts, ϕ_V^0 increased with an increase in temperature.

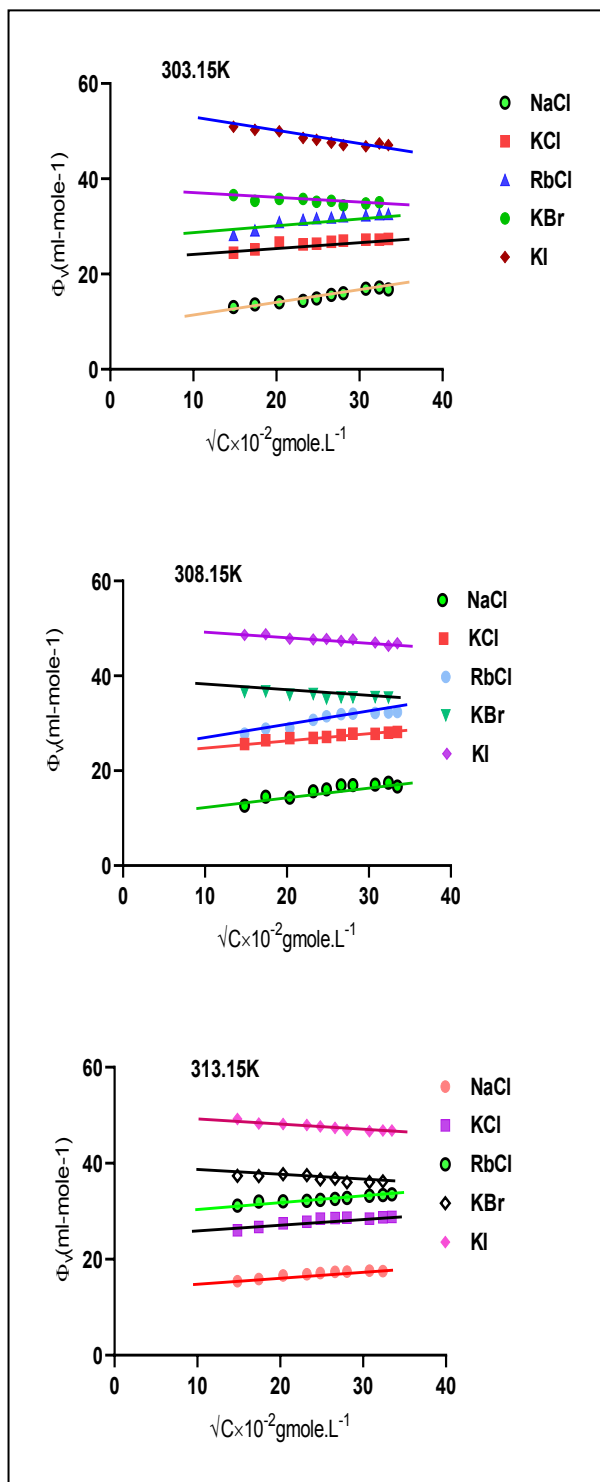


Figure 1. Apparent molar volume (ϕ_V) as a function of \sqrt{C} of Alkali metal halides in 10% (w/w) 2-(Ethoxy) ethanol-water mixture at 303.15 K, 308.15 K and 313.15 K.

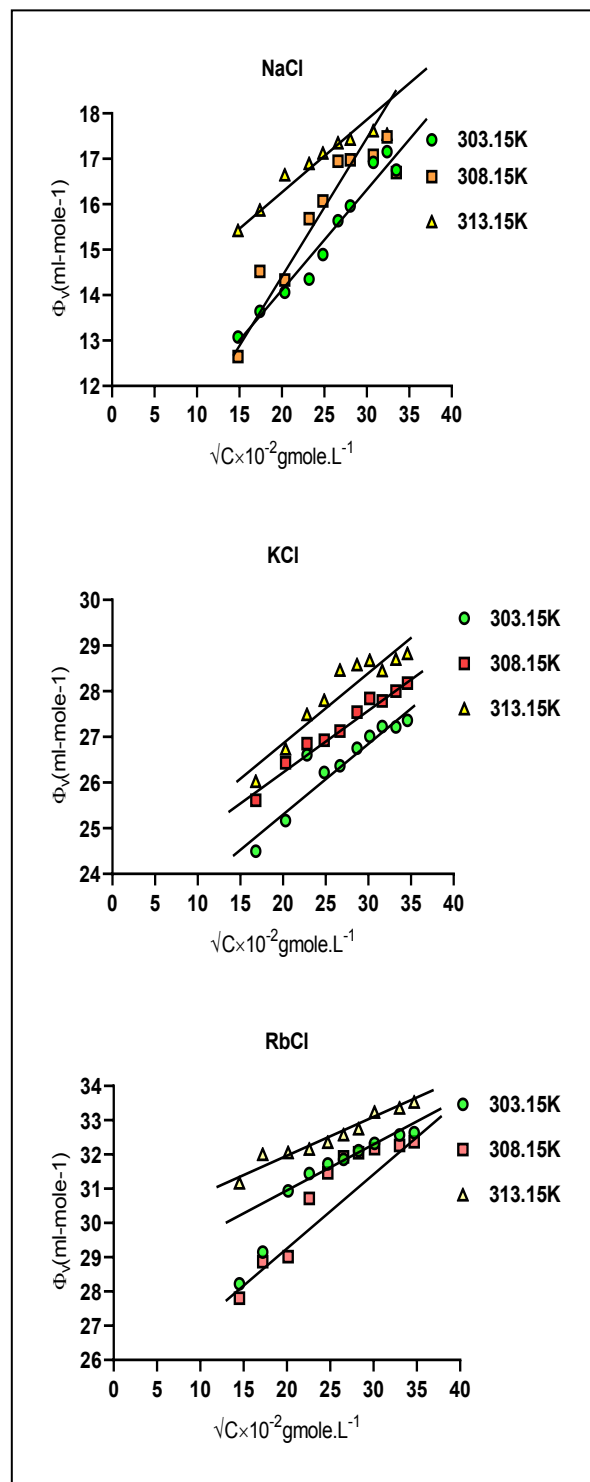


Figure 2. Apparent molar volume (ϕ_V) as a function of \sqrt{C} of NaCl, KCl and RbCl in 10% (w/w) 2-(Ethoxy) ethanol-water mixture at 303.15 K, 308.15 K and 313.15 K.

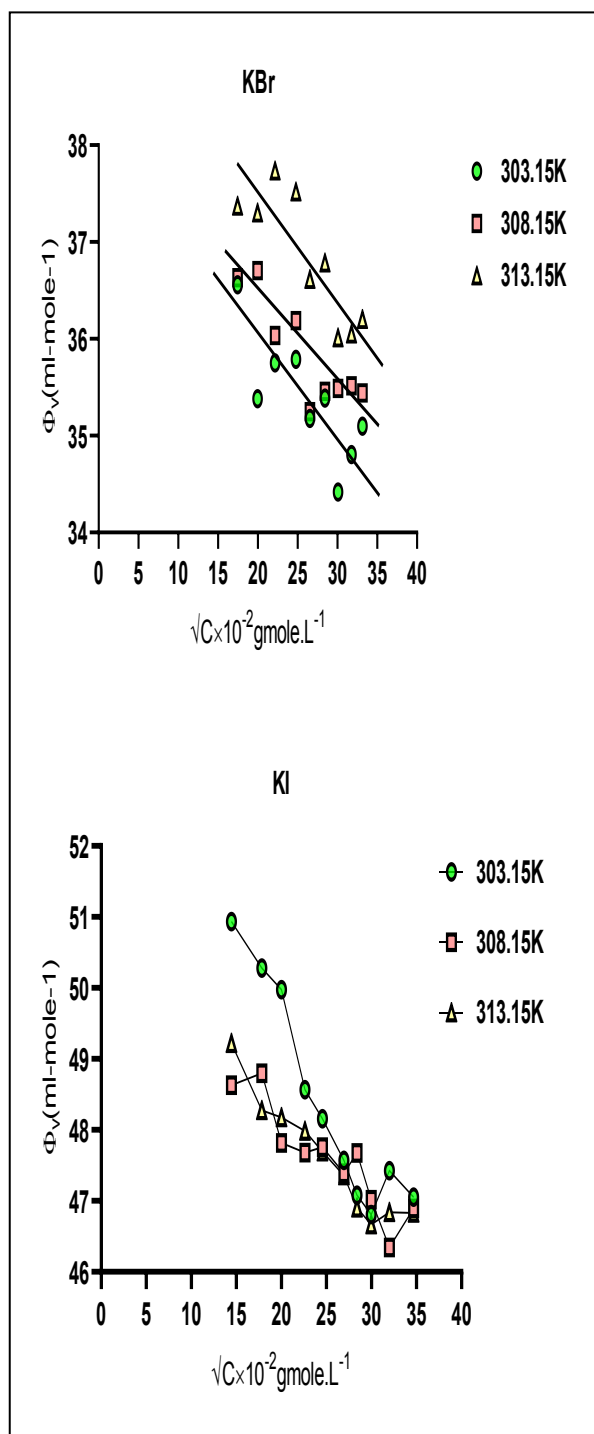


Figure 3. Apparent molar volume (ϕ_V) as a function of \sqrt{C} of KBr and KI in 10% (w/w) 2-(Ethoxy) ethanol-water mixture at 303.15 K, 308.15 K and 313.15 K.

3.2. Limiting ionic partial molar volumes

Ion-solvent interactions manifest themselves in all molar functions obtained by extrapolation to infinite

dilutions. It is possible to assign the contribution of cation and anion by separating the limiting molar functions into ionic contributions. Two methods were used in the current research:²⁷ (i) Convey and co-workers and (ii) Jolicoeur and co-workers for the purpose of comparison. A detailed discussion on the separation of limiting molar volumes is presented in our previous publication.⁹ From the $\bar{V}_{Br^-}^0$ the \bar{V}_{ion}^0 values of other ions were calculated using the additive nature of limiting partial molar volumes of solutes. The data obtained are presented in Table 3.

From Table 3 it can be observed that the $\bar{V}_{Na^+}^0$ is negative at 303.15 K and 308.15 K. The negative partial molar volume of an ion means that, with the addition of the ion, the decrease in the solution volume due to ion-solvent interactions is more than the increase in the solution volume due to the intrinsic ionic volume. From an observation of the $\bar{V}_{Na^+}^0$ values at 303.15 K, 308.15 K and 313.15 K, it is clear that as the temperature increases the sign of $\bar{V}_{Na^+}^0$ becomes positive at 313.15 K, indicating that at this temperature the decrease in solution volume due to ion-solvent interactions is less than the increase in the solution volume due to the intrinsic ionic volume.

The short-range solvating properties of ions have been discussed by considering the sign of the difference $(\bar{V}_{ion}^0 - \bar{V}_{cryst}^0)$.²⁸ An ion is considered as an electrostatic positive solvating (structure making) ion if $(\bar{V}_{ion}^0 - \bar{V}_{cryst}^0)$ is negative, and as a negative solvating (structure breaking) ion if $(\bar{V}_{ion}^0 - \bar{V}_{cryst}^0)$ is positive. It is assumed that this classification is valid even to the present aqua-organic mixed solvent system as it is water rich.

Data in Table 4 show that $(\bar{V}_{ion}^0 - \bar{V}_{cryst}^0)$ is negative for Na^+ and Cl^- ions at all temperatures (except for Na^+ at 313.15 K). It is a proven fact that the small ions with high charge density act as net structure makers.

The negative sign of $(\bar{V}_{ion}^0 - \bar{V}_{cryst}^0)$ agrees with this fact and proves that these ions are structure makers. The other alkali metal and halide ions (i.e. K^+ , Rb^+ , Br^- and I^-) have positive $(\bar{V}_{ion}^0 - \bar{V}_{cryst}^0)$ values showing that these ions are structure breaking ions. These facts are in accordance with the observations of other workers.²⁹

Table 3. Limiting partial molar volumes of various ions in 10% (w/w) 2-(Ethoxy) ethanol-water mixture at 303.15 K, 308.15 K and 313.15 K from I: the method of Convey and co-workers, II: the method of Jolicœur and co-workers

	Method I, ϕ_V (cm ³ mol ⁻¹)			Method II, ϕ_V (cm ³ mol ⁻¹)		
	303.15 K	308.15 K	313.15 K	303.15 K	308.15 K	313.15 K
Na ⁺	-3.04	-1.81	3.97	-23.19	-22.30	-16.72
K ⁺	9.74	12.04	14.17	-10.44	-8.45	-6.52
Rb ⁺	13.49	13.33	20.22	-6.66	-7.16	-0.47
C ^{l-}	12.59	11.52	9.62	32.74	32.01	30.31
Br ⁻	28.02	26.13	25.40	48.17	46.62	46.09
I ⁻	44.18	38.24	36.53	64.36	58.73	57.24

Table 4. ($\bar{V}_{ion}^0 - \bar{V}_{cryst}^0$) values for alkali and halide ions in 10% (w/w) 2-(Ethoxy) ethanol at 303.15 K, 308.15 K and 313.15 K

	$(\bar{V}_{ion}^0 - \bar{V}_{cryst}^0)$		
	303.15 K	308.15 K	313.15 K
Na ⁺	-5.20	-3.97	1.81
K ⁺	3.82	6.11	8.24
Rb ⁺	5.33	5.16	12.05
C ^{l-}	-2.35	-3.42	-5.32
Br ⁻	9.33	7.44	6.71
I ⁻	18.78	12.84	11.13

3.3. Components of limiting ionic molar volumes

Using the multilayer hydration models of Gurney, Frank-Wen and Eigen-Wicke for ion-solvent interactions, Millero^{28,30} has shown that the limiting ionic partial molar volume \bar{V}_{ion}^0 can be attributed to the following components.

$$\bar{V}_{ion}^0 = \bar{V}_{intr}^0 + \bar{V}_{elect}^0 + \bar{V}_{stru}^0 + \bar{V}_{cage}^0 \quad (4)$$

Where $\bar{V}_{(intr)}^0$ is the intrinsic partial molar volume (the positive increment in the \bar{V}_{ion}^0 due to the intrinsic ionic volume). $\bar{V}_{(elect)}^0$ is the electrostriction partial molar volume (the negative increment equals to the decrease in the molar solute volume due to ion-solvent electrostrictive interaction). $\bar{V}_{(intr)}^0$ is the disordered or void space partial molar volume (the increment due to the destruction of solvent structure in the region of ionic co-sphere). \bar{V}_{cage}^0 is the caged partial volume (the

negative increment is characteristic of hydrophobic “Structure making” ions such as R₄N⁺ ions). $\bar{V}_{(intr)}^0$ of the solutes are calculated adopting Padova equation²⁸ that makes use of both the molar volume and compressibility

$$\bar{V}_{intr}^0 = \phi_V^0 + \left(-\phi_K^0 \times \frac{S_V^*}{S_K^*} \right) \quad (5)$$

Where ϕ_V^0 is the partial molar volume of the solute, S_V^* is the experimental slope obtained from ϕ_V^0 versus \sqrt{c} graph, ϕ_K^0 is the partial molar adiabatic compressibility and S_K^* is the experimental slope obtained from the ϕ_K^0 versus \sqrt{c} graph. Using the compressibility data¹² of our work, the $\bar{V}_{(intr)}^0$ for the solutes are calculated only at 303.15 K (Table 5) (Since the compressibility data is available only 303.15 K in the present solvent system.

Table 5. $\bar{V}_{(intr)}^0$ calculated in 10% (w/w) 2-(OEt) EtOH-H₂O at 303.15 K

Salt	NaCl	KCl	RbCl	KBr	KI
$\bar{V}_{(intr)}^0$	28.61	35.80	48.88	28.30	46.04

Assuming that the method of Conway and co-workers for the separation of \bar{V}^0 values into ionic components is equally applicable to separate the $\bar{V}_{(intr)}^0$ values,⁹ the $\bar{V}_{(intr)}^0$ value is calculated to be 26.37 for Br⁻ ion at 303.15K. Applying additive rule the $\bar{V}_{(intr)}^0$ values of the other ions along with the \bar{V}_{ion}^0 are calculated.

Hepler's semi-empirical equation³¹ for the \bar{V}_{ion}^0 calculation in water is

$$\bar{V}_{ion}^0 = Ar^3 - BZ^2 / r \quad (6)$$

Where A, B are constants. Z and r are the charge and crystallographic radius of the ion, respectively. This equation is used to separate the geometric part from the electrostrictive part of the ionic volume.³² The first term of the equation is equal to $\bar{V}_{int}^0 + \bar{V}_{(disord)}^0$ and the second term is equal to $\bar{V}_{(elect)}^0$. For mono valent ions, the equation can be rearranged as

$$\bar{V}_{ion}^0 r = Ar^4 - B \quad (7)$$

To separate the intrinsic size of an ion and the void space effect, the following semi-empirical equations have been proposed by Hepler.³¹

$$\bar{V}_{ion}^0 = 2.52r^3 + (A - 2.52)r^3 - BZ^2 / r \quad (8)$$

$$\bar{V}_{ion}^0 = 2.52r^3 + A'r^2 - B'Z^2 / r \quad (9)$$

In these calculations, the void space is assumed to be equal to the surface of the ion, A' & B' are constants. A, B and A', B' have been determined by plotting $\bar{V}_{ion}^0 \times r$ against r^4 and $(\bar{V}_{ion}^0 r - 2.52r^4)$ against r^3 respectively. From the graphs in Figures 4 and 5, it can be seen that in both cases the cations and the anions fall into two separate straight lines and giving different A, B and A', B' values for the cations and the anions.

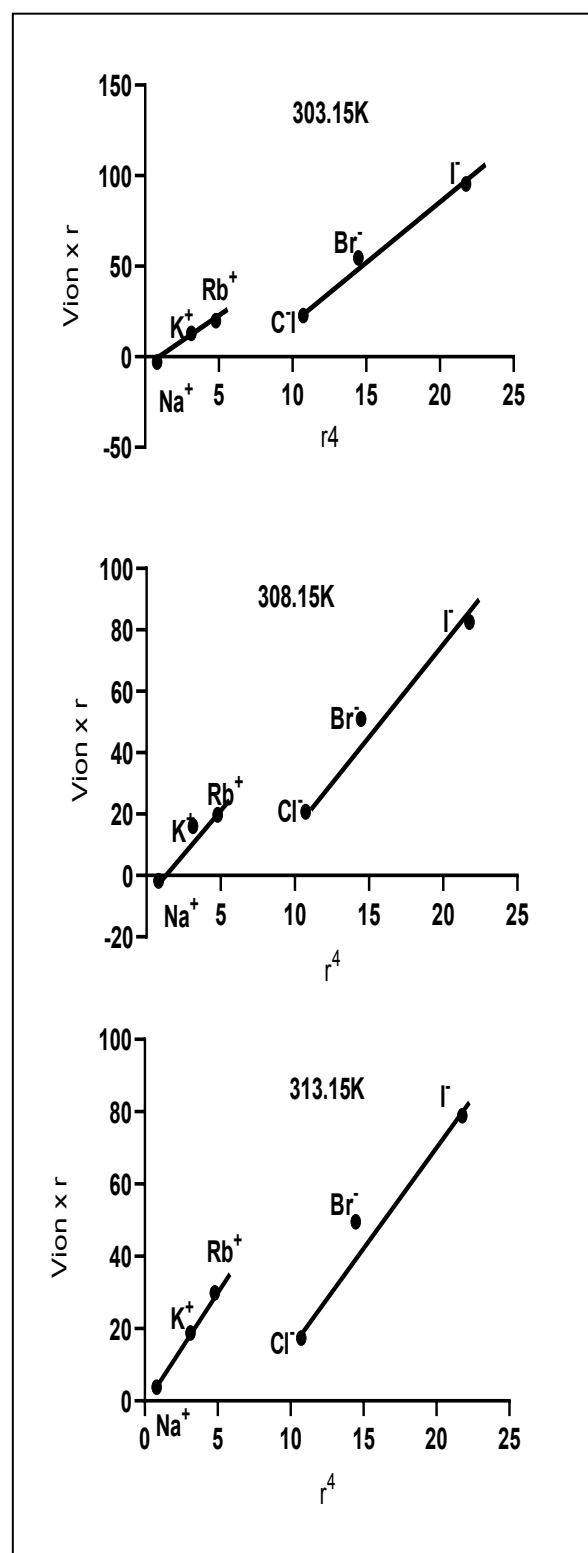


Figure 4. Plot of $V_{ion} \cdot r$ against r^4 for alkali metal and halide ions in 10% (w/w) 2-(OEt) EtOH-H₂O mixture at 303.15 K, 308.15 K, and 313.15 K.

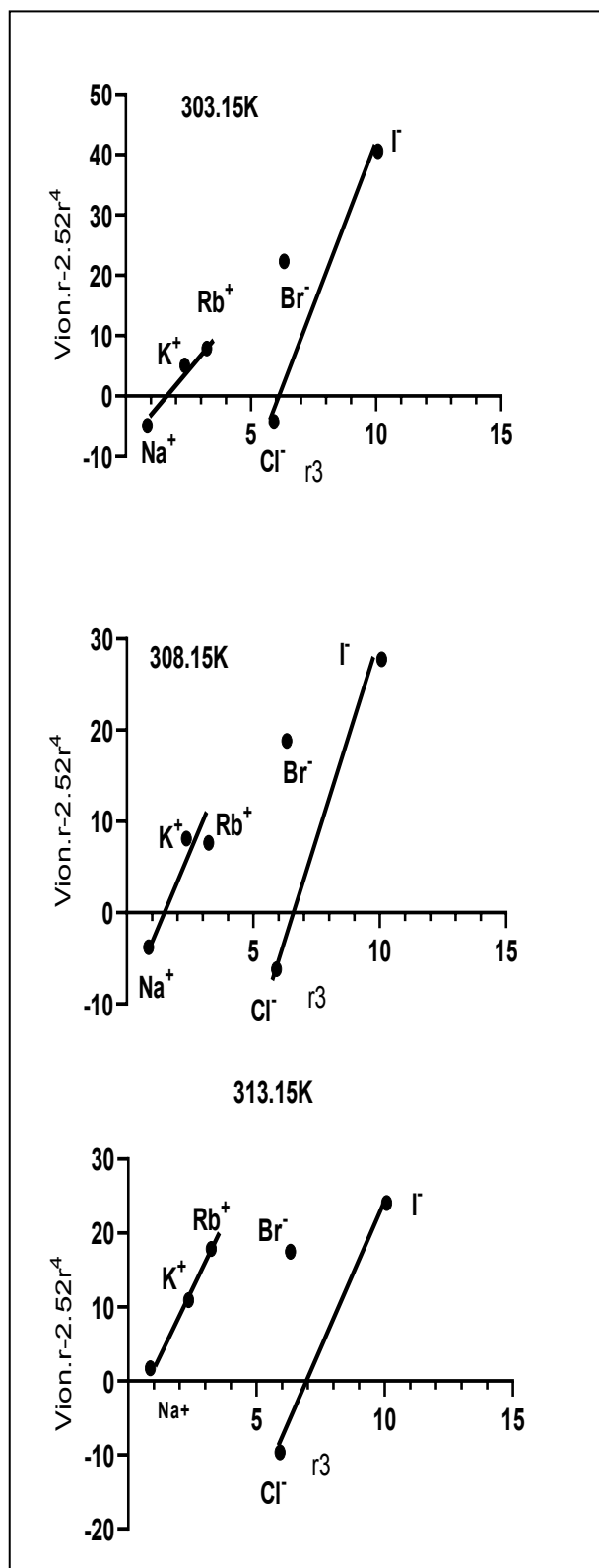


Figure 5. Plot of $(\bar{V}_{ion}r - 2.52r^4)$ against r^3 for alkali metal and halide ions in 10% (w/w) 2-(Ethoxy) ethanol-water mixture at 303.15 K, 308.15 K and 313.15 K.

According to Hepler,³¹ one should not expect plots of various functions of \bar{V}_{ion}^0 , Z and r to give only one line for both cations and anions because radii of ion cavities are larger than corresponding crystal radii and also crystal radii are greater for cations than for anions.

From Table 7, it can be seen that B is larger for anions than cations. The larger B values for anions than cations indicate that the ion-solvent interactions are greater for anions than for cations of the same size and charge.

Table 6. \bar{V}_{int}^0 of various ions along with \bar{V}_{ion}^0 in 10% (w/w) 2-(OEt) EtOH-H₂O at 303.15 K

	$\bar{V}_{(int)}^0$	\bar{V}_{ion}^0
Na ⁺	-5.26	-3.04
K ⁺	1.93	9.74
Rb ⁺	15.01	13.49
Cl ⁻	33.87	12.59
Br ⁻	26.37	28.02
I ⁻	44.11	44.18

Table 7. Values of A ($\text{cm}^3 \text{mol}^{-1} (\text{Å}^0)^{-3}$) and B ($\text{cm}^3 \text{mol}^{-1} \text{Å}^0$) from Eq. 6 and A' ($\text{cm}^3 \text{mol}^{-1} (\text{Å}^0)^{-2}$) and B' ($\text{cm}^3 \text{mol}^{-1} \text{Å}^0$) and from Eq. 9 of ions at 303.15 K, 308.15 K and 313.15 K

Ions	303.15 K	308.15 K	313.15 K	
Alkali Metal Cations	A_+	5.8	4.60	5.2
	A'_+	5.4	7.3	7.2
	B_+	8.0	4.5	1.6
	B'_+	9.5	11.0	7.0
Halide Anions	A_-	6.5	5.4	5.4
	A'_-	10.5	8.0	8.0
	B_-	43.2	33.5	35.2
	B'_-	64.0	49.5	50.0

Table 8. Comparison of values of $\bar{V}_{(disor)}^0$ and $\bar{V}_{(electr)}^0$ of alkali and halide ions by two methods in 10% (w/w) 2-(OEt) EtOH-H₂O at 303.15 K, 308.15 K and 313.15 K

Ion	303.15 K		308.15 K		313.15 K		303.15 K		308.15 K		313.15 K	
	i	ii	i	ii	i	ii	i	ii	i	ii	i	ii
	$\bar{V}_{(disor)}^0$						$\bar{V}_{(electr)}^0$					
Na ⁺	2.81	4.87	1.78	6.59	2.30	6.50	8.42	10.00	4.73	11.58	1.68	7.37
K ⁺	7.72	9.5	4.89	12.91	6.30	12.74	6.01	7.14	3.38	8.27	1.20	5.26
Rb ⁺	10.63	11.83	6.74	15.99	8.69	15.77	5.40	6.42	3.04	7.43	1.08	4.73
Cl ⁻	23.60	39.40	17.08	26.21	17.08	26.21	23.86	35.36	18.51	27.35	19.45	27.62
Br ⁻	29.51	39.92	21.35	30.42	21.35	30.42	22.15	32.82	17.18	25.38	18.05	25.64
I ⁻	40.11	48.99	29.02	37.32	29.02	37.32	20.00	29.63	15.51	22.92	16.29	23.15

Note: i and ii indicate the methods.

Table 9. Dimensions of various ions (Radius in Å) in 10% (w/w) 2-(Ethoxy) ethanol-water mixture

Ion	303.15 K	308.15 K	313.15 K	Pauling's crystallographic radius ³⁶
Na ⁺	1.02	1.08	1.31	0.95
K ⁺	1.50	1.57	1.63	1.33
Rb ⁺	1.64	1.60	1.77	1.48
Cl ⁻	1.58	1.55	1.50	1.81
Br ⁻	1.93	1.90	1.88	1.85
I ⁻	2.20	2.11	2.08	2.16

$\bar{V}_{(disord)}^0$ & $\bar{V}_{(elect)}^0$ are calculated from the constants A, B and Aⁱ and Bⁱ are presented in the table. The $\bar{V}_{(elect)}^0$ values obtained for the ions cannot be compared with the theoretical $\bar{V}_{(elect)}^0$ values from the Drude and Nerst equation³³ since the evaluation of theoretical $\bar{V}_{(elect)}^0$ requires the value of $\frac{\partial(\ln D)}{\partial P}$ which is not available for the solvent system studied.

3.4. Dimensions of ions

Padova and Conway's equations are used to estimate effective radii for various ions^{34,35}

$$(i) \bar{V}_{ion}^0 = 4.48 r_{ion}^3 - 8.0 / r_{ion} \quad (10)$$

$$(ii) \bar{V}_{ion}^0 = 2.51 r_{ion}^3 - 3.15 / r_{ion}^2 \quad (11)$$

Comparison of radius of the ions in the solution with effective crystallographic radius proposed by Pauling³⁶ shows that the cations are solvated to some extent however not much significantly, while the anions are either least solvated or un-solvated in the present solvent system.

4. CONCLUSIONS

The following results are obtained from this study.

- Positive values of the S_V^* for NaCl, KCl, and RbCl at all the temperatures indicate the presence of ion-ion interactions.
- The ϕ_V^0 values for concerning cations are in the order Rb⁺ > K⁺ > Na⁺ and structure breaking effects are in the order Na⁺ > K⁺ > Rb⁺. For anions, the ϕ_V^0 values are in the order I⁻ > Br⁻ > Cl⁻ and structure breaking effect order is Cl⁻ > Br⁻ > I⁻.

- $(\bar{V}_{ion}^0 - \bar{V}_{cryst}^0)$ are negative for Na^+ and Cl^- , which act as net structure makers. $(\bar{V}_{ion}^0 - \bar{V}_{cryst}^0)$ are positive for K^+ , Rb^+ , Br^- and I^- , which act as net structure breakers.

ACKNOWLEDGEMENTS

The author is thankful to Mr. Sanjay ji Ghodawat (Chairman S.G.U), Shri Vinayak Bhosale (Trustee, S.G.U), Mr. Srinivas Konduti (Director SGIMA) and Mr. Sreedhar Gupta (Centre head SGIMA) for their support during this research work. The author express his thanks to his research colleague Mr. Maruthi Kavuri, Personnel Officer, Singareni Collieries Ltd., Telangana. The author records his gratitude to the research supervisor Late Dr. K. Lakshminarayana, Professor, Physico-Chemical Laboratories, Sri Venkateswara University, Tirupathi. (A. P) India.

Conflict of interests

Author declares that there is no a conflict of interest with any person, institute, company, etc.

REFERENCES

- Boruń, A.; Florczak, A.; Bald, A. *J. Chem. Eng. Data* **2010**, 55, 3, 1252-1257.
- Stanozyk, M.; Borun, A.; Jozwiak, M. *J. Mol. Liq. Eng. Data*, **2019**, 278, 247-1252.
- Hedwig, G. R.; Hakin, A. W. *Phys. Chem. Chem. Phys.* **2004**, 6, 4690-4700.
- Das, S.; Das, K.; Roy, N.; Ekka, D.; Roy, M. N. *Int. J. Res. Chem. Environ.* **2018**, 9, 1-10.
- Stanozyk, M.; Borun, A.; Jozwiak, M. *J. Mol. Liq. Eng. Data* **2019**, 278, 247-252.
- Mozo, I.; Gonzalez, J. A.; Garcia delaFuente, I.; Cobos, J. C.; Riesco, N. *J. Mol. Lliq.* **2008**, 140, 87-100.
- Sharma, B.; Sharma, R.; Das, C. *J. Chem. Eng. Data* **2012**, 57, 3375-3384.
- Das, B.; Hazra, D. K. *J. Chem. Eng. Data* **1999**, 44, 865-868.
- Murthy, T. S. *Int. Res. J. Chem. Chem. Sci.* **2019**, 6 (1), 92-103.
- Cobos, J. C.; Garcia, I.; Casanova, C. *Can. J. Chem.* **1988**, 66, 2618-2620.
- De, R.; Guha, C.; Das, B. *J. Solution Chem.* **2006**, 35, 1505-1514.
- Murthy, S. T.; Rambabu, B.; Lakshminarayana, K.; (a) *Acoust. Lett.* **1995**, 19 (6), 120-125. (b) *Acoust. Lett.* **1993**, 17 (6), 111-118.
- Piekarski, H.; Tkaczyk, M. *J. Chem. Soc. Farad. T.* **1995**, 91, 2299-2306.
- Murthy, T. S. *J. Ultra Chem.* **2019**, 15 (3), 30-38.
- CRC Handbook of Chemistry and Physics. 94th Ed.; Haynes, W. M., Ed.; CRC Press LLC, Boca Raton, FL 2013-2014, p. 3-248.
- Sarkar, A.; Dakua, V. K.; Mishra, D. K.; Sinha, B. *Indian J. Adv. Chem. Sci.* **2016**, 4 (2), 180-187.
- Millero, F. J. *Chem. Rev.* **1971**, 71 (2), 147-176.
- Gopal, R.; Singh, K. Z. *Phys. Chem. Neue Fol.* **1970**, 69, 81-87.
- Wen, W. Y.; Saito, S. *J. Phys. Chem.* **1964**, 68, 2639-2644.
- Gopal, R.; Aharwal, D. K.; Kumar, R. *Bull. Chem. Soc. Japan* **1973**, 46 (7), 1973-1976.
- Desnoyers, J.E; Avedikian, L.; Perron, G.J. *Solution Chem.* **1975**, 4, 331-346.
- Gopal, R.; Srivastava, S. K.. *J. Phys. Chem.* **1962**, 66, 2074-2076.
- Dack, M. R. J.; Bird, K. J.; Parker, A. J. *Aust. J. Chem.* **1975**, 26, 955-963.
- Blokhra, R. L.; Agarwal, S. K. *Electro. Chim Acta* **1977**, 22, 141-144.
- Das, S.; Das, K.; Roy, N.; Ekka, D.; Roy, M. N. *Int. J. Res. Chem. Environ.* **2018**, 9, 1-10.
- Stanozyk, M.; Borun, A.; Jozwiak, M. O. *J. Mol. Liq. Eng. Data* **2019**, 278, 247-252.
- Krumgalz, B. S. *J. Chem. Soc. Far. Trans I.* **1980**, 76, 1887-1904.
- Millero, F. J. *Structure and transport process in water and aqueous solutions*, Ed. R. A. Horne, John Wiley, New York, 1972.

29. Jolicoeur, C.; Philip, P. R.; Perron, G.; Leduc, P. A.; Desnoyers, J. E. *Can. J. Chem.* **1972**, 50, 3167-3178.
30. Millero, F. J. *Biophysical properties of skin*, Ed. H. R. Elden, John Wiley, New York, 1971.
31. Hepler, L. G. *J. Phys. Chem.* **1957**, 61, 1426-1429.
32. Kawaizumi, F.; Zana, R. *J. Phys. Chem.* **1974**, 78 (6), 627-634.
33. Drude, P.; Nerst, W.; *Z. Phys. Chem.* **1894**, 15, 79-85.
34. Padova, *J. Chem. Phys.* **1964**, 40 (3), 691-694.
35. Conway, B. E.; Verrall, R. E.; Desnoyers, J. E. *Trans. Far. Soc.* **1966**, 62, 2738-2749.
36. Pauling, L. *The Nature of chemical bond*, 3rd Ed. Oxford and IBH Pub. Co. 1967.



Investigation dissolution behaviours and kinetics parameters of ulexite in boric acid solution

✉ Mehmet Harbi ÇALIMLI^{1,*}, ✉ Mehmet TUNÇ², ✉ Mehmet Muhtar KOCAKERİM³

¹Medical Services and Techniques Department, Tuzluca Vocational School, Iğdir University, 76000 Iğdir, Turkey

²Department of Chemical, Science Faculty, Yuzuncu Yıl University, 65100 Van, Turkey

³Department of Chemical, Science Faculty, Çankırı Karatekin University, Çankırı, Turkey

Received: 10 May 2020; Revised: 20 July 2020; Accepted: 05 August 2020

*Corresponding author e-mail: mharbi.calimli@igdir.edu.tr

Citation: Çalimli, M. H.; Tunç, M.; Kocakerim, M. M. *Int. J. Chem. Technol.* 2020, 4 (2), 121-129.

ABSTRACT

Nowadays, boron and its derivatives are widely used in industrial and technological areas. Boron minerals are the main sources for obtaining pure boron chemicals in the usage of different applications such as the defense industry, health, industry, kitchen equipments, etc. In this paper, for the first time, it has been reported the dissolution behaviors and kinetics parameters of ulexite in the boric acid solution. To solve ulexite by boric acid is important, because boric acid as a solvent prevents the formation of impurities, and therefore our study is a first in the literature. In this context, the dissolution of the ulexite has been investigated under various experimental parameters such as temperatures, acid concentration, solid/liquid ratio, particle size, dissolution rate, and stirring speed. The experimental findings shown that the dissolution kinetics of ulexite increase with an increase in temperature and acid concentration and a decrease in particle size, but decrease with mixing speed in the acid. Moreover, the dissolution of ulexite in boric acid and activation energy were evaluated. As a result, it was found that the dissolution kinetics were compatible with the chemical control model and the activation energy was 22.024 kJ mol⁻¹.

Keywords: Ulexite, boric acid, dissolution, kinetic, activation energy.

1. INTRODUCTION

Many different boron minerals such as borax, tincal, colemanite, and ulexite are present and commercially important. Generally, almost all of these minerals are found in some different salt forms and all of these minerals contain B₂O₃.¹⁻³ The increasing demand for

Uleksitin borik asit çözeltisinde çözünme ve kinetik parametre davranışlarının incelenmesi

ÖZ

Günümüzde bor ve türevleri yaygın olarak endüstri ve teknolojik alanlarda kullanılmaktadır. Bor mineralleri savunma sanayi, sağlık, mutfak ekipmanları vb. alanlarda kullanılan saf bor kimyasallarını elde etmek için ana kaynaklardır. Bu çalışmada, ilk kez, uleksitin borik asit çözeltisindeki çözünme davranışları ve kinetik parametreleri rapor edilmiştir. Uleksiti borik asitte çözmek önemlidir, çünkü bir çözücü olarak borik asit safsızlıkların oluşumunu engeller ve bu nedenle çalışmamız literatürde bir ilktir. Bu bağlamda, uleksitin çözünmesi, sıcaklıklar, asit konsantrasyonu, katı/sıvı oranı, partikül boyutu, çözünme hızı ve karıştırma hızı gibi çeşitli deneysel parametreler altında incelenmiştir. Deneysel bulgular, uleksitin çözünme kinetiğinin sıcaklık ve asit konsantrasyonundaki artış ve partikül boyutundaki azalma ile arttığını, ancak asitteki karıştırma hızı ile azaldığını göstermiştir. Ayrıca, uleksitin borik asitteki çözmesi ve aktivasyon enerjisi değerlendirildi. Sonuçta çözünme kinetiğinin kimyasal kontrol modeli ile uyumlu olduğu ve aktivasyon enerjisinin 22,024 kJ mol⁻¹ olduğu bulundu.

Anahtar Kelimeler: Uleksit, borik asit, çözüme, kinetik, aktivasyon enerjisi.

boron mineral in different fields such as ceramic and glass industries, nuclear technology, refractors, catalysts, polymer production, increases the importance of boron minerals and derivatives. The examples of the current studies on ulexite and boron minerals include solidification of nuclear radioactive wastes, cementite-based composite neutron protection properties, and

effects on borates' portland cement.⁴⁻⁷ These boron minerals mentioned are raw materials and used to produce boron compounds.

Ulexite is one of the raw materials and sources of boron elements used widely to produce boric acid, sodium perborate, etc. Ulexite as a hydrate contain sodium/calcium borate, and its formula has been detected as $\text{Na}_2\text{O}\cdot 2\text{CaO}\cdot 5\text{B}_2\text{O}_3\cdot 16\text{H}_2\text{O}$.⁸⁻¹⁰ Boron oxide, sodium perborate, boric acid are some of the compounds obtained from boron minerals and applied commercially and widely in various applications. Boric acid has a wide usage area to obtain the boron mineral among these boron compounds. For example, various chemicals like boron carbide, boron halides, organic borate, borate carbide are produced using boric acid. Alkaline and alkali borates, metals mixed, acidic minerals, and crystallized boric acid are the other chemicals that are produced from boron minerals. Generally, commercial methods have been preferred to fabricate boric acid^{11,12} So far, various acids have been used by reacted with boron minerals to obtain boric acid.

In a study,¹³ colemanite was tested with sulfuric acid under different experimental parameters to obtain boric acid. However, forming gypsum as a precipitate by-product and the presence of boric acid in the liquid

phase in this reaction are some of the harnesses such as sulfate contamination that cause environmental pollution. Furtherly, gypsum formation in the mentioned reaction exhibits the other adverse effects on soil and groundwater.^{14,15} Therefore, many different methods have been applied in various works. In these works, a lot of reactants such as nitric acid, chlorides, carbonate/sulfate of ammonia and caustic soda have been used to obtain boric acid from different boron minerals.^{2,16-18} To reveal behaviors of leaching, some different acids such as organic acids of citric acid, lactic acid, acetic acid, gluconic acid have been tested on different boron minerals.¹⁹⁻²¹ However, while the selectivity of organic acids is high, they are weak and exhibit low activity.³ Also, some inorganic acids such as ammonium nitrate, sulfur dioxide saturated water, sulfuric acid, hydrogen sulfate, ammonium chloride, and phosphoric acid have also been used in various studies related to ulexite. However, the mentioned inorganic acids cause the formation of undesirable by-products that prevent obtaining pure yield.²²⁻²⁸ For the mentioned reasons, in this study, for the first time, we investigated the behaviors of dissolution boric acid that is a similar substance with B_2O_3 present in the composition of ulexite. Table 1 summarizes some studies conducted on ulexite and their activation energies.

Table 1. Some studies related to ulexite and their kinetic results

Number	Acid and solution	Activation energy (kJ mol ⁻¹)	Reference
1	Acetic acid	55.8	3
2	Ammonium acetate	41.5	16
3	Ammonium acetate	55.7	29
4	Ammonia solution saturated with CO ₂	55	30
5	Ammonium chloride	80	31
6	Oxalic acid	59.8	32
7	Boric acid	22.02	This study

In this study, we investigated the dissolution properties of ulexite in boric acid solution under different experimental parameters such as acid concentration, temperature, solid/liquid ratio, and ulexite particle size. Further, some activation parameters including activation energy and fitting kinetic modes were also determined. There is not available any papers related to boric acid in the literature, so we think the investigation of boric acid effect on ulexite dissolution is a very important issue. Additionally, we think that the current study will add novelties related to the extraction contents of boron mineral, especially for boric acid content.

2. MATERIALS AND METHODS

2.1. Chemicals

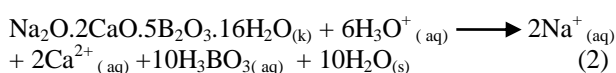
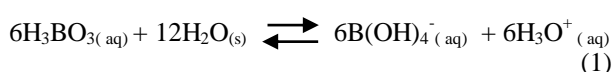
NaOH, HCl, EDTA used in the experiments were of analytical degree and used without any purification, and they were purchased from Sigma Aldrich. All glassware was cleaned with deionized water and ethanol. The ulexite used in the experiments was provided from Balıkesir city in Turkey. Ulexite was cleaned to remove visible impurities and then crushed to obtain the desired particle size for use in experiments.

2.2. Experimental procedure and the calculation of B₂O₃ amount

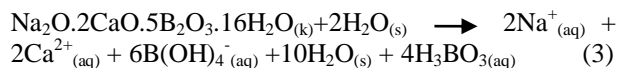
The experimental route is based on that given elsewhere.^{33,34} Ulexite dissolution experiments were carried out in a round bottom 250 ml flask at room temperature and atmospheric pressure. The mixture was

stirred using a thermostat mechanical stirrer to control the temperature of the reaction medium. A typical experiment was performed by transferring a 100 ml boric acid solution into the reaction balloon and mixed for 15 min to reach the equilibrium temperature.

After this time, the desired amount of ulexite was added to this mixture and reaction launched at certain time intervals. The dissolved ulexite at the end reaction was estimated by a complexometric technique conducted using the calcium ion (Ca^{2+}) determination method.³³ In this method, after the interactions of ulexite and boric acid at the end of the experiment, the resulting solution was filtered and then the amount of B_2O_3 in the latest solution was determined by stoichiometric using reactions given below.



Total reaction is summarized as



The calculation procedure of B_2O_3 was carried out like follows.

Firstly, a 10 ml solution taken from 100 ml solution and diluted to 50 ml. 5 ml of the resulting solution was taken and adjusted to pH 1 by adding NaOH solution. This latest solution was titrated using mürecsil indicator and 0.02M EDTA solution.

Due to the equivalent grams of Ca^{2+} and B_2O_3 , the conversion fraction of ulexit according to B_2O_3 was calculated from Eq. (4).

$$X_{\text{B}_2\text{O}_3} = \frac{\text{B}_2\text{O}_3 \text{ amount passed to solution}}{\text{Total B}_2\text{O}_3 \text{ amount in the sample}} \quad (4)$$

The experimental parameters tested in this study are given in Table 2.

Table 2. Experimental parameters tested on the dissolution ulexite in boric acid solutions

Parameters	Value
Acid concentration (% in wt)	1, 3, 4, 6*
Temperature (°C)	30, 40*, 50, 60, 70
Partical size (mm)	0.497, 0.348, 0.273, 0.177*
Stirring speed (rpm)	200, 300, 400*, 500
Solid/liquid ratio (g mL ⁻¹)	0.5/100, 1/100, 2/100, 4/100
Time (min)	3, 5, 10, 15, 20, 30, 40, 50

*Common parameters in all the experiments for dissolution ulexite in boric acid.

3. RESULTS AND DISCUSSION

3.1. The effect of temperature and acid concentration on the dissolution rate

The effect of reaction temperature on the dissolution of ulexite was studied at the temperatures of 30, 40, 50, 60, and 70°C. The results obtained from the experiments are graphed in Figure 1a. As can be seen from this figure, the dissolution kinetics of ulexite increased with increasing temperature. According to the Arrhenius equation, the dissolution kinetics increased in direct proportion to the exponential function of the heat. Arrhenius equation is as follows:

$$k = k_0 \exp(-E/RT) \quad (5)$$

Where, E is activation energy (J mol^{-1}). R is universal gas constant ($\text{J mol}^{-1} \text{K}^{-1}$). T is absolute temperature (in Kelvin). k is reaction rate. k_0 is reaction rate constant and refers to the number of collisions.

The effect of acid concentration on the dissolution of ulexite was investigated by using the acid concentrations of 1, 3, 4 and 6% (w/w) at the reaction temperature of 40°C, the particle size of 0.213 mm, the solid-to-liquid 0.01 g mL⁻¹, and stirring speed of 400 rpm. The results of the experiments are graphed in Figure 1b. As seen in Figure 1b, the dissolution rate increased with rising acid concentration. Because of the increase of acid concentration, the concentration of H_3O^+ increased in the solution. Herein, H_3O^+ acts as a reacting agent. These effects caused an increase in the dissolution rate.

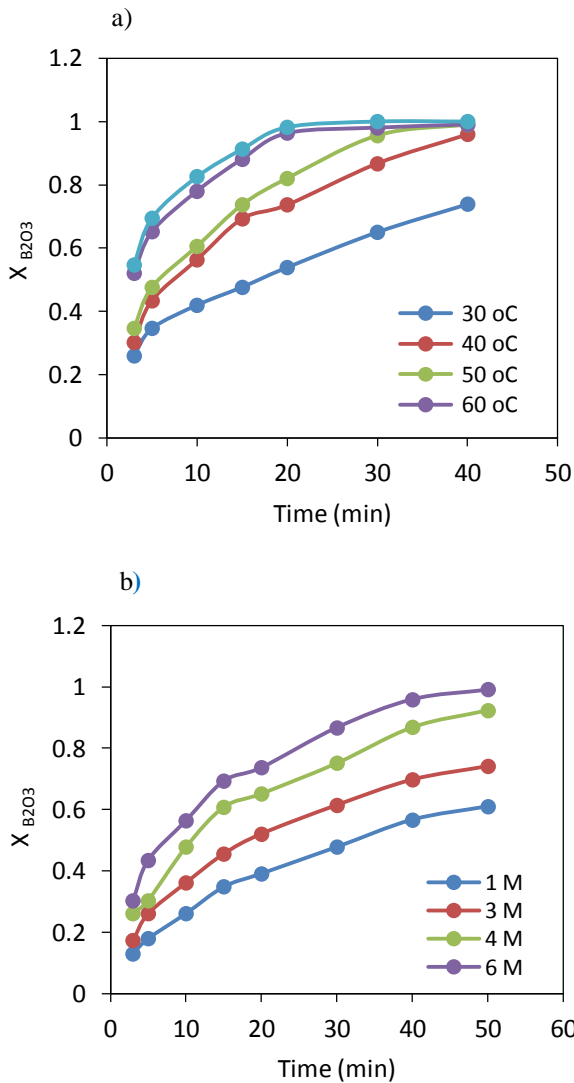


Figure 1. Effects of a) temperature. b) acid concentration on ulexite dissolution

3.2. The effect of particle size and stirring speed on the dissolution rate

To explain the effect of particle size, ulexite particles of 0.497, 0.348, 0.273, 0.177 mm were prepared and tested at 40°C, at a stirring speed of 400 rpm and at a concentration of 6% (w/w) of 0.01 g ml⁻¹. The results obtained are graphed in Figure 2a.

As seen in Figure 2a, the dissolution rate increased with decreasing ulexite size. Effect of stirring speed on the dissolution of ulexite was examined at 200, 300, 400, and 500 rpm at a reaction temperature of 40°C, the particle size of 0.177, solid-to-liquid of 0.01 g ml⁻¹ and boric acid concentration of %6 (w/w).

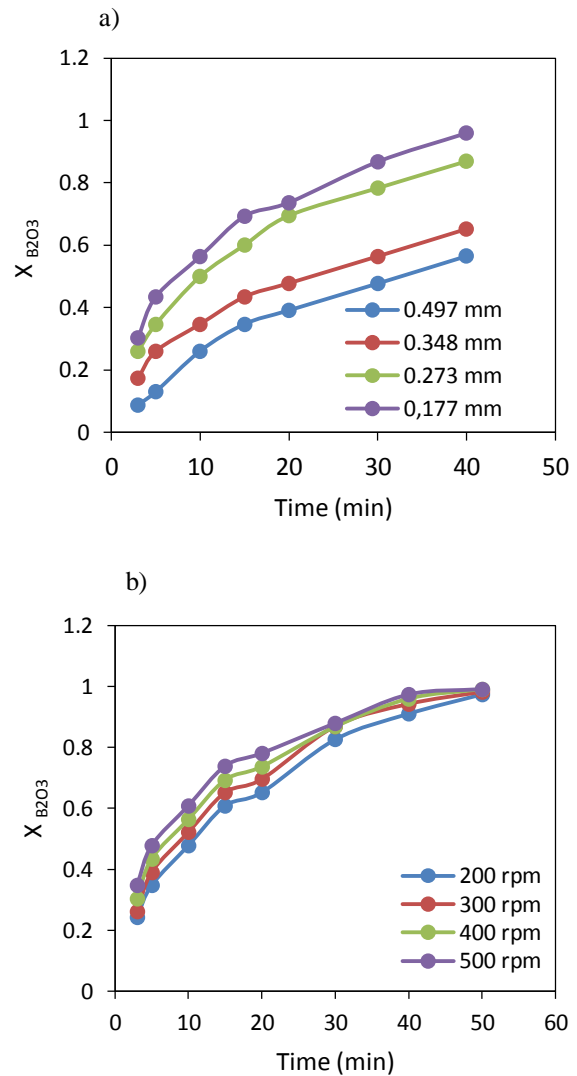


Figure 2. Effects of a) particle size, b) stirring speed on the dissolution of ulexite.

As seen in Figure 2b, the stirring speed had little effect on the dissolution of ulexite. Three different kinetic models were tested of ulexite. Three different kinetic models were teste to detect which parameter fits the dissolution rate of ulexite in the boric acid solution. As a result of these evaluations, the pseudo-homogeneous kinetic models were evaluated. The calculations and experimental results showed that the best kinetic model was found to be a chemical reaction control model as $1 - (1-X)^{1/2} = kt$.

Where, X is $X_{B_2O_3}$ given in Eq. (4). According to this model, the graph of $1 - (1-X)^{1/2}$ versus t at different temperatures is shown in Figure 3.

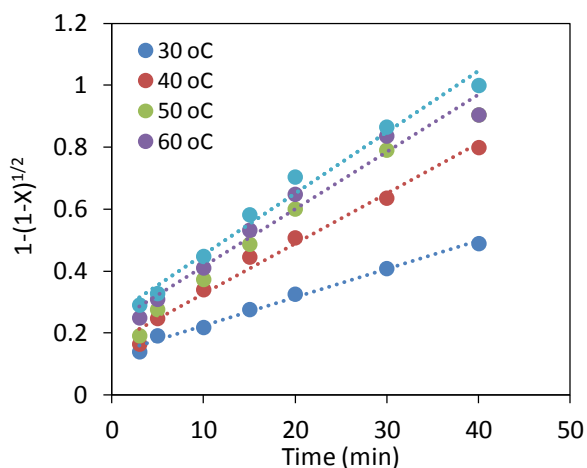


Figure 3. Agreement of experimental data with chemical reaction control model at different temperatures.

3.3. Solid-to-liquid ratio on the dissolution rate

The effect of solid-liquid ratio on dissolution of ulexite was investigated by taking 0.5/100, 1/100, 2/100, 4/100. The results obtained are graphed in Figure 4.

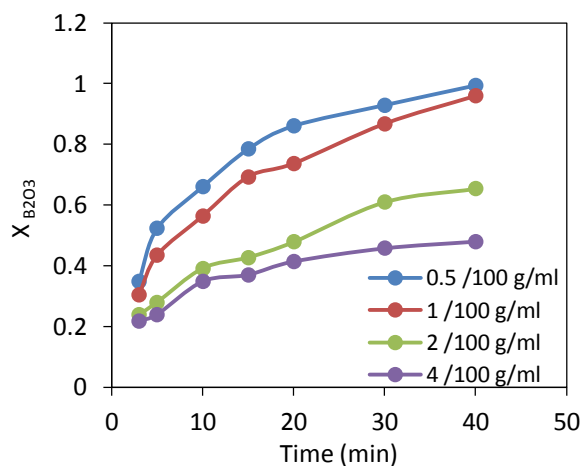


Figure 4. Effects of the solid-to-liquid ration on the dissolution of ulexite.

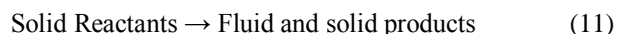
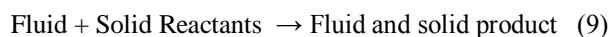
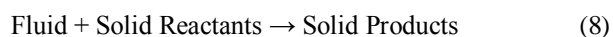
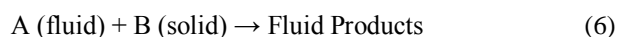
3.4. Kinetic evaluation of ulexite dissolution in boric acid solution

Chemical kinetics explains the progress of reactions, reaction steps, which reaction factors are connected, product formation conditions. Chemical reactions can occur in one phase (homogeneous reactions) or in more phases (heterogeneous reactions). The process used to dissolve the desired or undesirable products in a solution containing more than two phases are called leaching.³⁵⁻³⁸

Reaction systems are divided into two according to their phases as follows.

1. Homogeneous reactions: In such reactions, substances react and form in a single phase. Phases may be solid, liquid or gas. Homogeneous reactions can be studied catalytically or non-catalytically.³⁹⁻⁴¹

2. Heterogeneous reactions: These reactions take place in at least more than two phases. There are some factors such as interface areas, temperature, pressure, the shape of the reaction vessel, fluid-phase diffusion characteristics that affect reaction rate. The systems used heterogeneous reactions have some properties such as solid-liquid compositions, the formation of a product surrounding solid yield, the variation of volume and shape of a solid product during the reaction. The variation shape of solid products and solid/ liquid interaction can cause undesired results.⁴²⁻⁴⁷ The reactions that will occur are listed below.



In reactions with the excessive liquid phase, the concentration is considered to remain constant during the reaction.^{33,35,38,41,47} The equations that is applied to systems where such a liquid component is constant and our evaluations of the results for different models are given in Table 3.

The kinetics of the reaction between ulexite ore and boric acid were analyzed graphically and statistically using homogeneous and heterogeneous reaction models. The value of R^2 was found as 0.9821 for the diffusion controlled kinetic model (Table 3), and this indicated that the diffusion control model from the fluid film was valid.

3.4.1. Dependence on particle size and acid concentration

Using the results of experiments with particle sizes of 0.497, 0.348, 0.273, 0.177 mm, affecting the conversion speed, $1 - (1 - X)^{1/2}$ values are obtained graph against t . From the slope of the plot in Figure 5a, the apparent rate constant (k_f) values for each fraction were calculated.

Table 3. Integer rate equations and regression coefficients for reaction kinetics

Rate equations	Rate control types	R ²
$kt = -\ln(1-X)$	The homogeneous first phase reaction model	0.7277
$kt = 1 - 3(1-X)^{2/3} + 2(1-X)$	Ash (or product) for fixed-size particle diffusion-controlled from the film.	0.9447
$kt = 1 - (1-X)^{1/3}$	Controlled chemical reaction model.	0.9799
$kt = 1 - (1-X)^{1/2}$	Diffusion from the fluid film for the shrinking sphere controlled.	0.9821
$kt = 1 - (1-X)^{2/3}$	Diffusion from the fluid film for shrinking sphere controlled (small ones).	0.9818

The relation between the initial rate and particle size,

$$k_1 = k_2 [C]_0^b \quad (16)$$

$$k = k_1 (Rp)^a \quad (12)$$

where, k is reaction rate. k_1 is reaction rate constant. Rp indicates particle size. a is a constant depending on the number of particles. k_1 can be expressed as follows:

$$k_1 = k_0 [C]_0^b (S/L)^c (St.speed)^d e^{-E/RT} \quad (13)$$

where k_1 is reaction rate, k_0 is the reaction rate constant depends on stirring speed, $[C]_0$ indicates initial acid concentration (M). S/L is solid-liquid ratio. $St.speed$ indicates mixing speed. E is activation energy. R is universal gas constant ($8.314 \text{ J mol}^{-1} \text{ K}^{-1}$). T is temperature (K). b , c , and d are constants.

On the other hand, the linear form of Eq. (12) can be given as follows:

$$\ln k = \ln k_1 + a \ln Rp \quad (14)$$

The plot of $\ln k$ versus $\ln (Rp)$ is shown in Figure 5a. From the slope of this plot, The value of a was found to be -0.9412.

The results calculated in Eq. (12) gives Eq. (15).

$$k = k_1 (Rp)^{-0.9412} \quad (15)$$

While analyzing the effect of acid concentration on conversion rate and the values of $1-(1-X)^{1/2}$, the plot of $\ln(k_1)$ versus $\ln(C_0)$ was obtained by using boric acid solutions of 1%, 3%, 4%, and 6% (Figure 5b).

Relationship between reaction rate constant (k_1) and acid concentration can be given as follows

From the linear form of this equation, the values of $\ln k_1$ against $\ln[C]_0$ values were plotted (Figure 5b) and the value of b was found as 0.4420 from the slope of the obtained plot. Accordingly, Eq. (17) can be obtained as:

$$k_1 = k_2 (Rp)^{-0.9412} [C]_0^{0.4420} \quad (17)$$

Here k_2 is independent of particle size and acid concentration.

3.4.2. Dependence on solid/liquid ratio and stirring speed

Using the values of $1-(1-X)^{1/2}$ and the results of experiments performed on the conversion rate with solid/liquid ratios of 0.5 / 100, 1/100, 2/100, 4/100 g ml^{-1} , Figure 6a was obtained according to the linear equation of Eq. (18).

$$k_2 = k_3 (S/L)^c \quad (18)$$

where, k_2 is the reaction rate, k_3 is the reaction constant and c is a constant depends on solid/liquid rate. Figure 6a shows the plot of $\ln(S/L)$ against $\ln k_2$. The value of c from the slope of the plot in Figure 6a was found -0.6450. According to this, the following equation can be obtained

$$k_2 = k_3 (Rp)^{-0.9412} [C]_0^{0.4420} (S/L)^{-0.6450} \quad (19)$$

Where k_2 is reaction rate, k_3 is the reaction rate constant, Rp is particle size, $[C]$ is concentration, S/L is solid/liquid ratio.

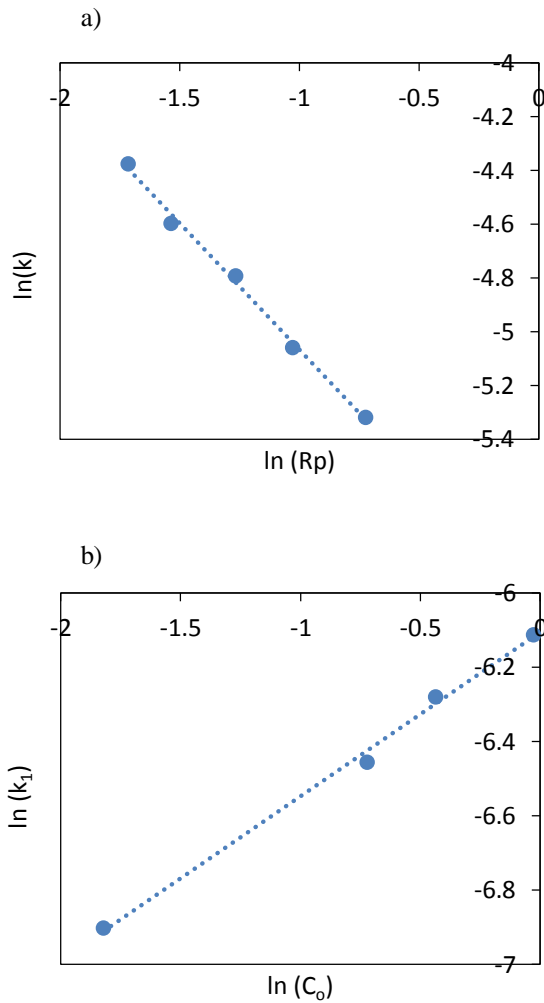


Figure 5. a) The plot of $\ln(k)$ versus $\ln Rp$, b) the plot of $\ln(k_1)$ against $\ln C_0$.

The data of $1 - (1-X)^{1/2}$ values and the results of the experiments of mixing speeds of 20.9439, 31.4159, 41.8879, 52.3598 radians / second of the conversion speed change were used in obtaining of Figure 6a using the linear form of Eq. (20).

$$k_3 = k_4 (St.speed)^d \quad (20)$$

Where, k_3 is reaction rate. k_4 is a rate constant independent of the mixing speed. d is the exponential constant. Figure 6b shows the plot of $\ln k_3$ against $\ln (St.speed)$. The value of d was determined as 0.0582 from the slope of the plot in Figure 6b.

According to this, Eq. (21) can be obtained.

$$k_3 = k_4(Rp)^{-0.9412} [C]^{0.4420} (S/L)^{-0.6450} (St.speed)^{0.05809} \quad (21)$$

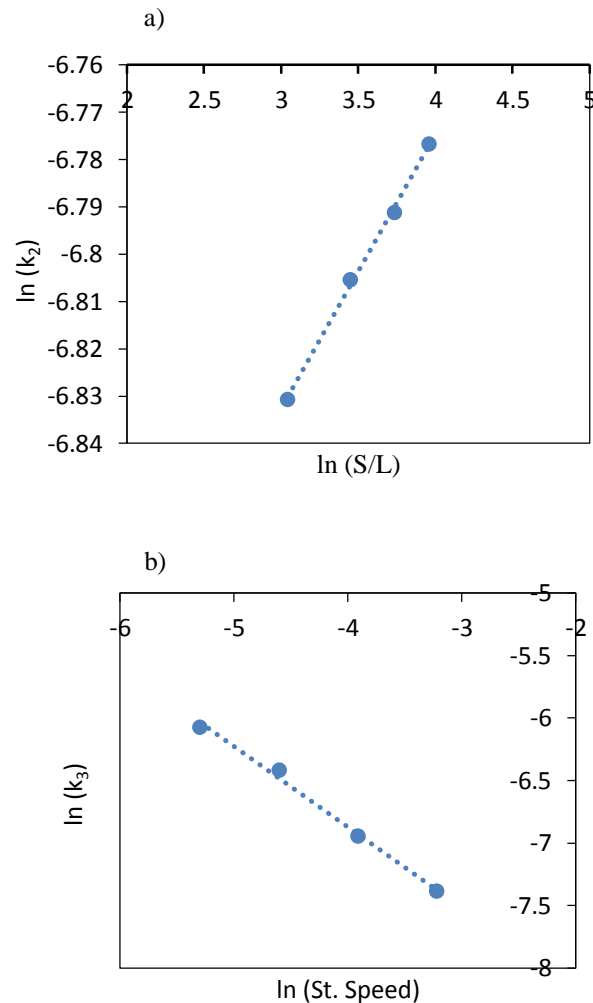


Figure 6. The plot of $\ln a(k_2)$ against $\ln S/L$ ratio, b) The plot of $\ln(k_3)$ versus $\ln (St. speed)$.

Where, k_e is reaction rate. k_4 is a rate constant in dependent of particle size. $[C]$ is acid concentration, S/L is solid/liquid ratio. $St.speed$ is mixing speed.

3.4.3. Dependence on reaction temperature

While examining the effect of reaction temperature on the conversion rate, the results of experiments with temperatures of 303, 313, 323, 333, and 343 K were obtained. Reaction rates obtained from the result of the experiments at different temperatures were used to obtain the Arrhenius graph in Figure 7. Arrhenius equation gives the change between reaction rate constant k_4 and reaction temperature (Eq. 22).

$$k_4 = k_0 \cdot e^{-E/RT} \quad (22)$$

Assuming that there is a relation of the shape, $1/T$ values are graphed against $\ln k_d$ values (Figure 7) and activation energy and Arrhenius constant were found from the slope of the plot obtained.

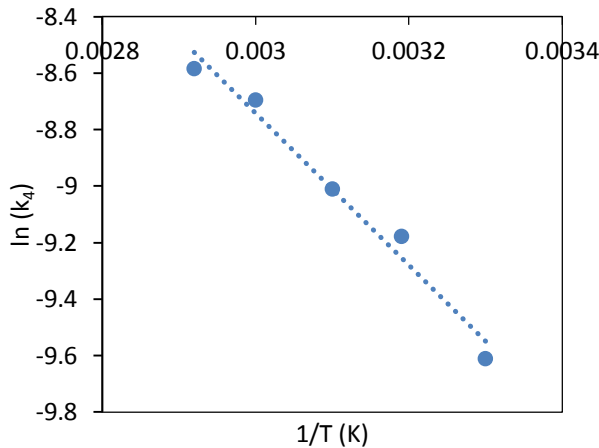


Figure 7. The plot of $\ln k_d$ versus $1/T$ for ulexite reaction in boric acid.

The speed expression representing the transformation of the ulexite ore in the boric acid solutions by replacing the a , b , c , d , E and k_0 values that show the effect of the parameters examined according to these results, a mathematical model was obtained as given below:

$$1 - (1-X)^{1/2} = k_d(Rp)^{-0.9412} [C]_0^{0.4420} (S/L)^{-0.6450} (St.speed)^{0.05809} e^{-2649.1226/T} \quad (23)$$

Where k_d is independent of particle size. Rp is particle size. $[C]_0$ is initial acid concentration, S/L is solid/liquid ratio. $St.speed$ is mixing speed.

4. CONCLUSIONS

In summary, the findings of this study can be expressed as follows:

The common values of the parameters used in the experiments are: particle size 0.177 mm, boric acid concentration 6%, mixing speed 400 rpm, solid/liquid ratio 1/100 g ml⁻¹, reaction temperature 40°C. And the following equations can be revealed

$$1 - (1-x)^{1/2} = kt \quad (24)$$

$$k = k_0 (Rp)^a [C]_0^b (S/L)^c (St.speed)^d e^{-E/RT} \quad (25)$$

Herein, the values of a , b , c , d and $-E/R$ values were found as a : -1.013, b : 0.4579, c : -0.650, d : 0.0545, E/R : -2649.1226, respectively.

By replacing these values, the speed expression representing the transformation of ulexite ore in boric acid solutions can be given as follows:

$$1 - (1-X)^{1/2} = [2.02(Rp)^{-1.013} [C]_0^{0.4579} (S/L)^{-0.650} (St.speed)^{0.0545} e^{-2649.12/T}]_t \quad (26)$$

Herein, it has been obtained as a mathematical model.

In this study, it was found that the dissolution rate increased with the decrease in the particle size, the solid/liquid ratio, the acid concentration, and the reaction temperature. The mixing rate did not change the dissolution rate much. In all the experiments in which common parameters were kept constant, it was found that the best dissolution occurred at a temperature of 70°C for 40 min.

ACKNOWLEDGEMENTS

The authors are grateful to YYÜ Scientific Research Projects Presidency for their financial support for project numbered 2013-FBE-D058.

Conflict of interests

Authors declare that there is no a conflict of interest with any person, institute, company, etc.

REFERENCES

1. Çavuş, F.; Kuşlu, S. *Ind. Eng. Chem. Res.* **2005**, *44*, 8164-8170.
2. Alkan, M.; Doğan, M.; Namli, H. *Ind. Eng. Chem. Res.* **2004**, *43*, 1591-1598.
3. Ekmekyapar, A.; Demirkiran, N.; Künkül, A. *Chem. Eng. Res. Des.* **2008**, *86*, 1011-1016.
4. Wei, C.; Ling, X.; Li, Q.; Yuan, B.; Li, B.; Ma, H. *Constr. Build. Mater.* **2019**, *215*, 777-785.
5. Piotrowski, T.; Glinicka, J.; Glinicki, M. A.; Prochoń, P. *Constr. Build. Mater.* **2019**, *195*, 583-589.
6. Sokol, E. V.; Sanderman, J.; Bradford, M.A. *Chem. Geol.* **2019**, *525*, 58-81.
7. Li, B.; Ling, X.; Liu, X.; Li, Q.; Chen, W. *Cement Concrete Comp.* **2019**, *102*, 94-104.
8. Temur, H.; Yartaşı, A.; Çopur, M.; Kocakerim, M. *M. Ind. Eng. Chem. Res.* **2000**, *39*, 4114-4119.

9. Xia, Y. K.; Peng, F. F. *Int. J. Miner. Process.* **2007**, *83*, 68-75.
10. Demirkiran, N.; Künkül, A. *Int. J. Miner. Process* **2007**, *83*, 76-80.
11. Taylan, N.; Gürbüz, H.; Bulutcu, A. N. *Ultrason. Sonochem.* **2007**, *14*, 633-638.
12. Ruecroft, G.; Hipkiss, D.; Ly, T.; Maxted, N.; Cains, P. W. *Org. Process Res. Dev.* **2005**, *9*, 923-932.
13. Mergen, A.; Demirhan, M.H; Bilen, B. *Adv. Powder Technol.* **2003**, *14*(3), 279-293.
14. Kurtbaş, A.; Kocakerim, M. M.; Küçük, Ö.; Yartaşı, A. *Ind. Eng. Chem. Res.* **2006**, *45*, 1857-1862.
15. Ekinci, Z.; Şayan, E.; Beşe, A. V.; Ata, O. N. *Int. J. Miner. Process* **2007**, *82* (4), 187-194.
16. Demirkiran, N.; Bayrakçi, N.; Asin, C. T. *Nonferr. Met. Soc.* **2013**, *23*, 1797-1803.
17. Ekmekyapar, A.; Künkül, A.; Demirkiran, N. *Min. Proc. Ext. Met. Rev.* **2010**, *31*, 250-255.
18. Künkül, A.; Aslan, N. E.; Ekmekyapar, A.; Demirkiran, N. *Ind. Eng. Chem. Res.* **2012**, *51*, 3612-3618.
19. Bayrak, B.; Laçin, O.; Bakan, F.; Saraç, H. *Chem. Eng. J.* **2006**, *117*, 109-115.
20. Laçin, O.; Dönmez, B.; Demir, F. *Int. J. Miner. Process* **2005**, *75*, 91-99.
21. Demir, F.; Laçin, O.; Dönmez, B. *Ind. Eng. Chem. Res.* **2006**, *45*, 1307-1311.
22. Demirkiran, N. *Hydrometallurgy* **2009**, *95*, 198-202.
23. Küçük, Ö.; Kocakerim, M. M. *Chem. Eng. Process* **2005**, *44*, 1005-1011.
24. Tunc, M.; Kocakerim, M. M.; Yapici, S.; Bayrakçeken, S. *Hydrometallurgy* **1999**, *51*, 359-370.
25. Kavci, E.; Çalban, T.; Çolak, S.; Kuşlu, S. *J. Ind. Eng. Chem.* **2014**, *20* 2625-2631.
26. Kuşlu, S.; Dişli, F. Ç.; Çolak, S. *J. Ind. Eng. Chem.* **2010**, *16*, 673-678.
27. Elbeyli, İ. Y. *Hydrometallurgy* **2015**, *158*, 19-26.
28. Doğan, H. T.; Yartaşı, A. *Hydrometallurgy* **2009**, *96*, 294-299.
29. Demirkiran, N. A. *Chem. Eng. J.* **2008**, *141*, 180-186.
30. Künkül, A.; Yapici, S.; Kocakerim, M. M.; Copur, M. *Hydrometallurgy* **1997**, *44*, 135-145.
31. Tekin, G.; Onganer, Y.; Alkan, M. *Can. Metall. Quart.* **1998**, *37*, 91-97.
32. Alkan, M.; Doğan, M. *Chem. Eng. Process* **2004**, *43*, 867-872.
33. Çalban, T.; Çolak, S.; Yeşilyurt, M. *Chem. Eng. Commun.* **2005**, *192*, 1515-1524.
34. Ekmekyapar, A.; Demirkiran, N.; Künkül, A. *Chem. Eng. Res. Des.* **2008**, *86*, 1011-1016.
35. Künkül, A.; Yapici, S.; Kocakerim, M. M.; Copur, M. *Hydrometallurgy* **1997**, *44*, 135-145.
36. Hubli, R. C.; Mittra, J.; Suri, A. K. *Hydrometallurgy* **1997**, *44*, 125-134.
37. Crundwell, F. K.; Godorr, S. A. *Hydrometallurgy* **1997**, *44*, 147-162.
38. Alkan, M.; Oktay, M.; Kocakerim, M. M.; Karagölge, Z. *Hydrometallurgy* **1991**, *26*, 255-262.
39. Maurice, D.; Hawk, J. A. *Hydrometallurgy* **1999**, *51*, 371-377.
40. Herreros, O.; Quiroz, R.; Viñals, J. *Hydrometallurgy* **1999**, *51*, 345-357.
41. Tunc, M.; Kocakerim, M. M.; Yapici, S.; Bayrakçeken, S. *Hydrometallurgy* **1999**, *51*, 359-370.
42. El-Cheikh, F. M.; Khalil, S. A.; El-Manguch, M. A.; Omar, H. A. *J. Chem. Educ.* **1985**, *62*, 761.
43. Bancroft, W. D. *J. Phys. Chem.* **1924**, *28*, 973-983.
44. Abu-Eishah, S. I.; Anabtawi, M. J. J.; Isaac, S. L. *Chem. Eng. Process* **2004**, *43*, 1085-1094.
45. Onal, E. D.; Usluogullari, A. *Eur. J. Integr. Med.* **2012**, *23*, 12.
46. Li, P.; Rao, Q. H.; Li, Z.; Jing, J. T. *Nonferr. Met. Soc.* **2014**, *24*, 499-508.
47. Demir, H.; Özmetin, C.; Kocakerim, M. M.; Yapici, S.; Çopur, M. *Chem. Eng. Process* **2004**, *43*, 1095-1100.



Preparation and characterization of activated carbon from almond shell by microwave-assisted using $ZnCl_2$ activator

Şirin Özlem TEĞİN, Ömer ŞAHİN, Orhan BAYTAR*, Mehmet Sait İZGİ

Department of Chemical Engineering, Faculty of Engineering, Siirt University

Received: 4 June 2020; Revised: 26 August 2020; Accepted: 27 August 2020

*Corresponding author e-mail: baytarorhan@gmail.com

Citation: Teğın, Ş. Ö.; Şahin, Ö.; Bayraktar, O.; İzgi, M. S. *Int. J. Chem. Technol.* 2020, 4 (2), 130-137.

ABSTRACT

Microwave-assisted activated carbon was synthesized from almond shell by chemical activation method using $ZnCl_2$ activator. The effects of the microwave gas medium, microwave power, microwave time, activation temperature, activation time and impregnation ratio on the synthesis were investigated. Activated carbon was also synthesized in the same way without the microwave treatment. The characterization of the synthesized activated carbons was performed by SEM, FTIR and BET devices. The iodine number of the microwave assisted activated carbon (70% activator/raw material ratio, 250 W microwave power, 15 min microwave time, 500°C activation temperature and 45 min activation time) and activated carbon without microwave (70% activator/raw material ratio, 500°C activation temperature and 45 min. activation time) were determined to be 1141 mg/g and 190 mg g^{-1} , respectively. The BET surface areas of microwave assisted activated carbon and without microwave were determined as 1057 $m^2 g^{-1}$ and 50 $m^2 g^{-1}$, respectively. The methylene blue numbers of the microwave assisted activated carbon and activated carbon without microwave were determined to be 201.40 mg g^{-1} and 97.14 mg g^{-1} , respectively. According these values, it can be said that the microwave process has a significant effect on activated carbon production.

Keywords: Microwave, activated carbon, chemical activation, iodine number.

ZnCl₂ kullanılarak badem kabuğundan mikrodalga destekli aktif karbon üretimi ve karakterizasyonu

ÖZ

$ZnCl_2$ aktifleştiricisi kullanılarak kimyasal aktivasyon yöntemiyle badem kabuğundan mikrodalga destekli aktif karbon sentezlenmiştir. Sentez üzerine mikrodalga gaz ortamı, mikrodalga gücü, mikrodalga süresi, aktivasyon sıcaklığı, aktivasyon süresi ve impragnasyon oranı etkisi incelenmiştir. Aynı yöntemle mikrodalga olmaksızın aktif karbon da sentezlenmiştir. Sentezlenen aktif karbonların karakterizasyonu SEM, FTIR ve BET cihazlarıyla gerçekleştirilmiştir. Mikrodalga destekli aktif karbon (%70 aktifleştirici/hammadde oranı, 250 W mikrodalga gücü, 15 dk. mikrodalga süresi, 500 oC aktivasyon sıcaklığı ve 45 dk. aktivasyon süresi) ve mikrodalga olmaksızın aktif karbon (%70 aktifleştirici/hammadde oranı, 500°C aktivasyon sıcaklığı ve 45 dk. aktivasyon süresi) iyot sayıları sırasıyla 1141 mg g^{-1} ve 190 mg g^{-1} olduğu belirlenmiştir. Mikrodalga destekli ve mikrodalga olmaksızın aktif karbonların BET yüzey alanları nın sırasıyla 1057 $m^2 g^{-1}$ ve 50 $m^2 g^{-1}$ olduğu belirlenmiştir. Mikrodalga destekli ve mikrodalga olmaksızın aktif karbonların metilen mavisi sayılarının sırasıyla 201,40 mg g^{-1} ve 97,14 mg g^{-1} olduğu belirlenmiştir. Bu değerlere göre, mikrodalga işleminin aktif karbon üretiminde ciddi bir etkiye sahip olduğu söylenebilir.

Anahtar Kelimeler: Mikrodalga, aktif karbon, kimyasal aktivasyon, iyot sayısı.

1. INTRODUCTION

Activated carbon is an excellent adsorbent used to remove various impurities. It has various advantages such as possessing high surface area, well developed

internal structure and various functional groups.¹ Despite the advantages of the activated carbon adsorption process, the greatest obstacle in its wider applications is the long pyrolysis time and the provision of large devices that require high energy for biomass

types.² The inclination of unsuitable heating rates impedes active carbon quality. Therefore, a fast and easy method must be developed to prepare activated carbon.³

Two different methods are generally used to synthesize activated carbon. These methods are known as physical activation and chemical activation. Physical activation is the activation of raw material with carbon dioxide (CO₂) or water vapor.⁴ Chemical activation consists of a single step and involves the usage of activators such as zinc chloride (ZnCl₂), potassium hydroxide (KOH), potassium carbonate (K₂CO₃) and phosphoric acid (H₃PO₄). The carbon percentage of the chemical activation method is higher than that of the physical activation.⁵ In addition, the best developed porous activated carbons are obtained via chemical activation.⁶ Activated carbon can be produced from many raw materials. Examples include pistachio shell,⁷ *Elaeagnus angustifolia* seeds,⁸ carob bean seed husk,⁹ almond shell,¹⁰ and sunflower husk.¹¹

Almond (*Prunus amygdalus* L.), a hard-shelled fruit that is grown in almost every region of the world, belongs to the genus *Prunus* of the Rosaceae family of Rosales.¹² There are approximately 40 different types of almonds. The almond fruit has an important place in human nutrition due to its high nutritional value. In addition, almond shells, which are abundant and low-cost residues, are suitable for being used as raw materials.¹³ As it is consumed for its nourishing oil, rich minerals and vitamins, its production is increasing day by day. The average annual production of almonds is 80,000 tons in Turkey.¹⁴

Microwave technology has attracted attention because it provides homogeneous and fast thermal reactions.

Microwave heating provides many advantages such as improved reaction rates and yields, performing reactions at lower temperatures, obtaining better structural properties, rapid temperature rise and uniform temperature distribution.¹⁵ In addition, microwave technology has been used successfully to synthesize activated carbon. Impregnation process in the microwave environment in the production of activated carbon from almond shell is not available in the literature, and was first performed in this study. In the microwave-assisted activated carbon studies given in the literature, the activation process takes place in the microwave environment. In this study, the impregnation process was carried out in the microwave environment.

In our study, activated carbon synthesized by the microwave assisted chemical activation method was obtained from almond shells. The BET surface areas of microwave assisted activated carbon and without microwave were determined respectively. When the iodine number, methylene blue number and BET surface area numbers were taken into consideration, it was observed that microwave treatment had a significant effect on the production of activated carbon.

2. MATERIALS AND METHODS

2.1. Materials

All chemical materials used in the experimental studies were obtained from Merck and were of analytical purity. Deionized pure water was used in the experimental studies. Almond shells were obtained from the province of Siirt, Turkey. The system used to synthesize the activated carbon is given in Figure 1. The system consists of a microwave and horizontal ash oven.

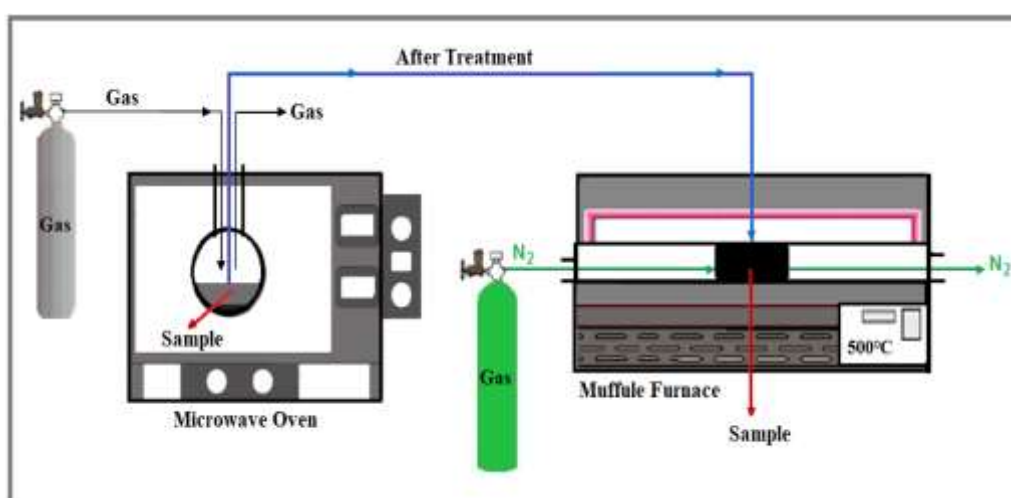


Figure 1. System used for the production of activated carbon.

2.2. Synthesis of activated carbon

The almond shells were milled and sieved, then washed with distilled water and dried at 80°C. Activated carbon was synthesized by the microwave assisted chemical activation method. For the synthesis of the activated carbon, 3 g of ground almond shells were mixed with 3 g of ZnCl₂ activator dissolved in 2 ml of distilled water and the impregnation of the activator into the almond shells was carried out in a microwave. In the microwave environment, the activated carbon was synthesized by subjecting the activation time to 45 min at 500°C in the presence of nitrogen (N₂). The activated carbon washed with 0.5 M hydrogen chloride (HCl) and then hot distilled water until the pH value was 6-7.

2.3. Characterization of activated carbon

The iodine number of the active carbons obtained was determined. Iodine adsorption is performed to learn more about the porous structure of activated carbon. Iodine adsorption in the liquid phase is considered as a simple and rapid test. The iodine number is determined by the surface area of the pores with a radius greater than 1 nm. The iodine number is accepted as a basic parameter used to characterize the performance of activated carbon.⁷ The method used by the International American Society of Testing and Materials was used to determine the iodine number (ASTM, 2006). The iodine number was calculated using Eq. (1).

$$\text{Iodine number} = \frac{(B-A) \times 127 \times N \times 40}{m \times B} \quad (1)$$

Where, A is the amount of Na₂S₂O₃·5H₂O spent in titration after activated carbon iodine adsorption (ml). B is amount of Na₂S₂O₃·5H₂O spent in titration for 0.1 N iodine solution (ml). N is iodine solution concentration. m is the amount of activated carbon (g).

In the synthesis of activated carbon, iodine number is used as an alternative to the BET surface area in the laboratory environment. For this reason, the iodine number of all activated carbons obtained was determined and plotted. The activated carbon with the highest iodine number was sent to BET analysis

The BET surface area of the activated carbons with high iodine number was determined by the Quantachrome Nova 1200 series device. The characterization of the activated carbon with the highest surface area, pure almond shell and non-microwave activated activated carbon, scanning electron microscopy (SEM), and fourier-transform infrared spectroscopy (FTIR) devices were performed and methylene blue number were determined. The methylene blue number was used to estimate mesoporosity of activated carbons. A good quality activated carbon should have high iodine number and methylene blue number.⁷

The number of methylene blue was calculated from Eq. (2).

$$q_e = \frac{(C_0 - C_e)}{w} V \quad (2)$$

Where, q_e is the amount of methylene blue adsorbed per unit adsorbent (mg g⁻¹). C_0 is solution initial concentration (mg l⁻¹). C_e is the concentration of solution in equilibrium state (mg l⁻¹). V is solution volume (ml). w is the amount of adsorbent (g).

3. RESULTS AND DISCUSSIONS

The SEM images of the almond shell, microwave assisted activated carbon and without the microwave treatment are given in Figure 2 (a-c), respectively.

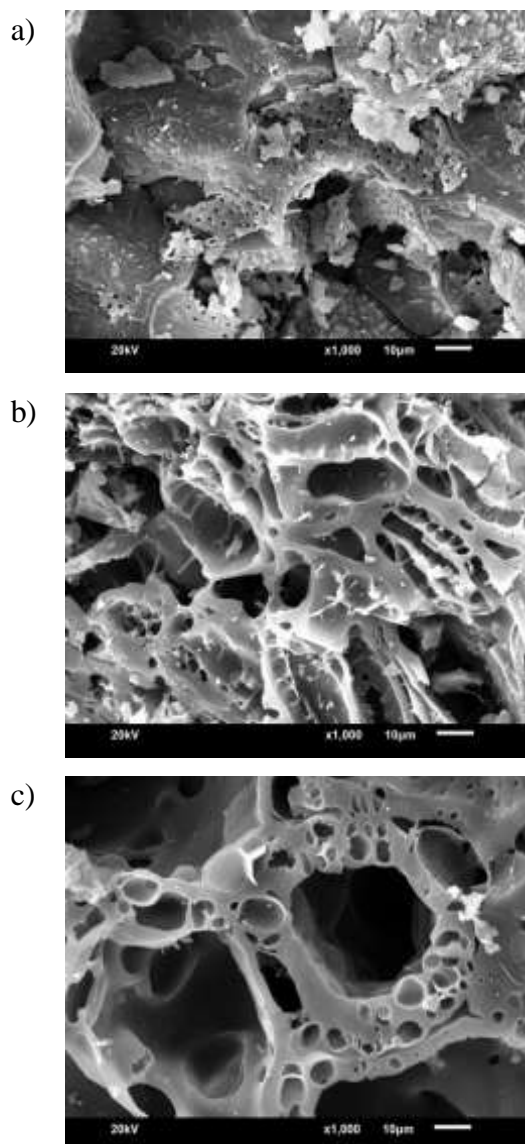


Figure 2. SEM image of: a) Pure almond shell, b) Microwave assisted activated carbon, c) Activated carbon without the microwave treatment.

As can be seen from Figure 2a, the surface of the pure almond shell was rough, although not very porous. The surface of the microwave assisted activated carbon appears to be porous and flat (Figure 2b). It is seen from Figure 2b that the microwave-assisted activated carbon surface was more porous and smooth compared to the almond shell. As can be seen from Figure 2, the microwave causes the activated carbon to form a micropore structure. In addition, it was observed that the micropores of the microwave-assisted activated carbon were greater than those of the activated carbon without the microwave treatment.

The BET surface area analysis of the synthesized activated carbon with high iodine numbers was performed and the results obtained are given in Figure 3.

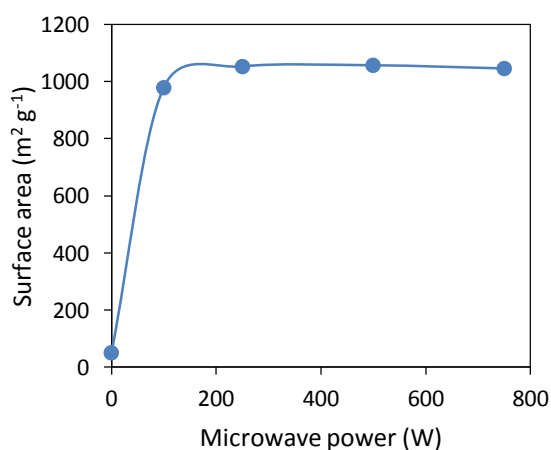


Figure 3. Variation of microwave power with surface area.

Figure 3 shows that the surface area of the activated carbon impregnated in the microwave was $1057 \text{ m}^2 \text{ g}^{-1}$, while the surface area of the activated carbon not impregnated in the microwave was $50 \text{ m}^2 \text{ g}^{-1}$. The effect of the microwave power on the impregnation of activated carbon is clearly seen from the BET surface area data.

The FTIR spectra of almond shell, microwave assisted and without microwave activated carbon are given in Figures 4a-c, respectively.

It is seen that there are more than one functional group in the structure of the almond shell. Figure 4 shows the presence of the OH-functional group connected to the peak hydrogen bonds at 3700 cm^{-1} wavenumber. It shows the presence of C-H functional group due to peak methyl groups at 3000 cm^{-1} .^{2, 16} The peak at 2300 cm^{-1} indicates the presence of the -COOH functional group. It shows the presence of C-C bonds due to peak olefinic groups at $2000\text{-}1800 \text{ cm}^{-1}$. It shows the presence of the peak CH_2 functional group at 1500 cm^{-1} .

The peak at 1266 cm^{-1} shows the presence of C-C and C-O functional groups. The peaks smaller than 1000 cm^{-1} indicate the presence of functional groups resulting from the aromatic ring.

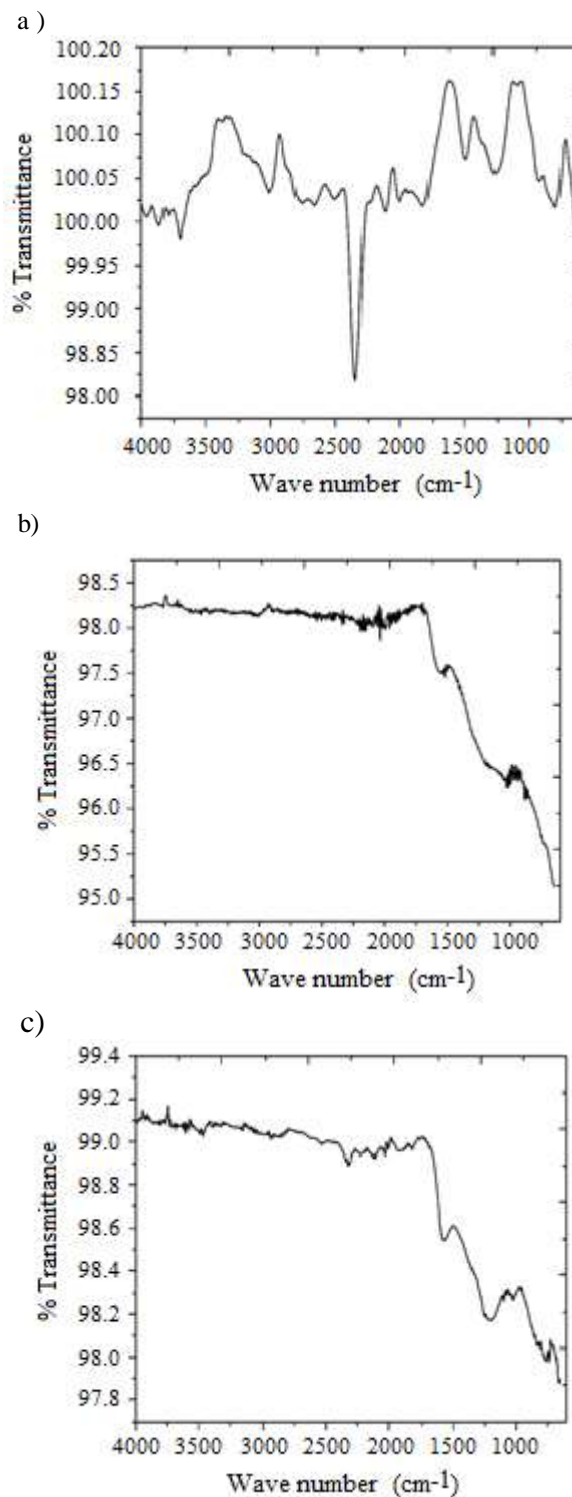


Figure 4. FTIR graphs: a) Raw material, b) Microwave assisted activated carbon; c) Activated carbon without microwave.

It can be seen from Figure 4 that although there are many functional groups in the structure of the pure almond shell, there are not many functional groups in the structure of the activated carbon synthesized with microwave treatment. The probable reason for this is that the microwave power weakens the bonds formed between the activator and the raw material. The functional groups in the activated carbon structure, which were synthesized without microwave treatment, are more than the functional groups in the microwave-assisted activated carbon structure. These results support the idea that microwave power weakens the bonds between the raw material and the activator.

Methylene blue number of microwave assisted activated carbon and without microwave was determined as 201.40 mg/g and 97.14 mg g⁻¹, respectively. The high methylene blue number indicates that activated carbon is mesoporous.¹⁷ Microwave-assisted activated carbon seems mesoporous in the SEM images also.

Impregnation ratio is one of the most important parameters in the preparation of activated carbon. The effect of impregnation ratio was investigated under the conditions of 750 W microwave power, 15 min microwave time, 500°C activation temperature and 45 min activation time. The experiments were performed at impregnation ratios of 20%, 50%, 70%, 100% and 150%. The variation of iodine numbers with the ratio of impregnation is given in Figure 5.

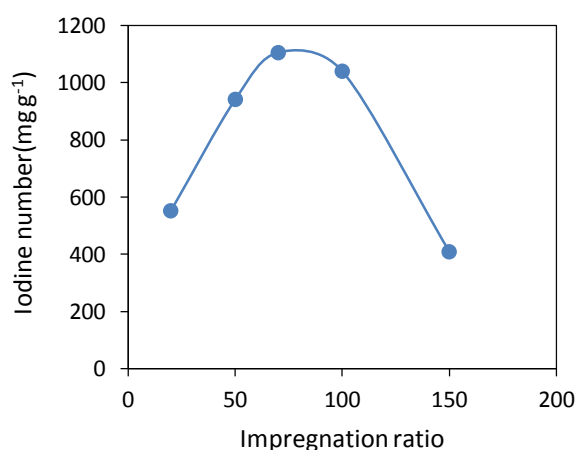


Figure 5. Variation of iodine number according to impregnation ratio (microwave power 750 W; microwave time 15 min.; activation temperature 500°C; activation time 45 min. and CO₂).

It is seen that iodine number increases with the increase of the impregnation ratio from 20% to 70%, while the iodine number decreases when the impregnation ratio become greater than 70%. There are two possible reasons for this. First, when the amount of activator is low, it does not fully activate with raw material.

Secondly, when the amount of activator is high, the activated carbon causes the pores to have a macro structure. Şahin and co-workers⁸ have found the same result on the activated carbon obtained by the chemical activation method using the ZnCl₂ activator from the spindle nucleus. In their studies, the best impregnation ratio has been determined to be 70% and used in subsequent experiments. Liu and co-workers have found that the impregnation rate of activated carbon which they have obtained from bamboo using phosphoric acid, was 100%.¹⁸

After determining the best impregnation ratio, the effect of different gases on the microwave environment was investigated under 70% impregnation ratio, 750 W microwave power, 15 min microwave time, 500°C activation time and 45 min activation time. The iodine numbers of activated carbons obtained are given in Table 1.

Table 1. The effect of different gases on iodine number

Gas	Iodine number
CO ₂	1105
N ₂	1011
Ar	1024

The iodine number of the activated carbon obtained in the presence of CO₂ was higher. The possible reason for this is thought to be the weakening of the bonds between the activator and the raw material in the presence of CO₂ by the microwave. The CO₂ gas was used to examine the effect of other parameters. Sharif and co-workers have found that CO₂ gas in microwave environment is effective in the activated carbon they have obtained from sesame stem with microwave support. The probable cause of this situation is that they have stated that carbon dioxide has reacted with more pores formed during the pyrolysis process.¹⁹

The effect of microwave power was investigated under 15 min microwave time, CO₂ gas environment, 500°C activation temperature and 45 min activation time. The variation of iodine number of activated carbons by microwave power is given in Figure 6.

It is observed that the iodine number increases when the microwave power increases from 100 W to 250 W. However, when the microwave power became greater than 250 W, the iodine number decreased. This may be due to the fact that the bond between the activator and the raw material is completely weakened when the microwave power is 250 W.

It is also thought that the viscosity of the activator was reduced with microwave heat and therefore, better penetration into the interior of the activating raw

material occurred. When the microwave power was below 250 W, the activator did not penetrate well into the inner side of the raw material as it did not reduce the viscosity of the activator. When the microwave power is low, it is thought that it does not weaken the bonds between the activator and the raw material. For these reasons, the iodine number was chosen to be low. When the microwave power was above 250 W, the viscosity of the activator greatly increased and, as a result, the pore structure of the raw material caused macro formation.

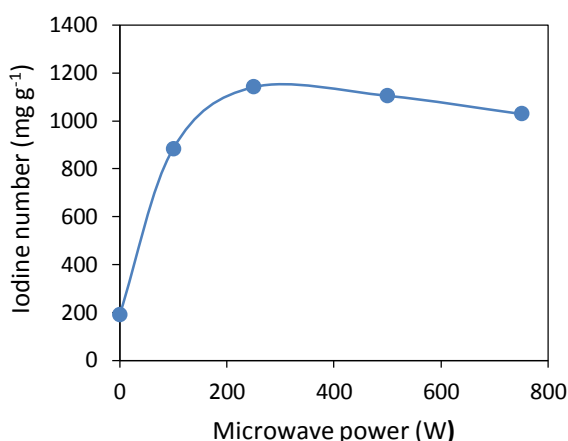


Figure 6. Variation of iodine number according to microwave power (impregnation ratio 1:1; microwave time 15 min; activation temperature 500°C; activation time 45 min and CO₂).

The effect of the microwave time was investigated under the 250 W microwave power, CO₂ gas environment, 500 °C activation temperature and 45 min activation time. The change in the iodine numbers of activated carbons with microwave power is graphed in Figure 7.

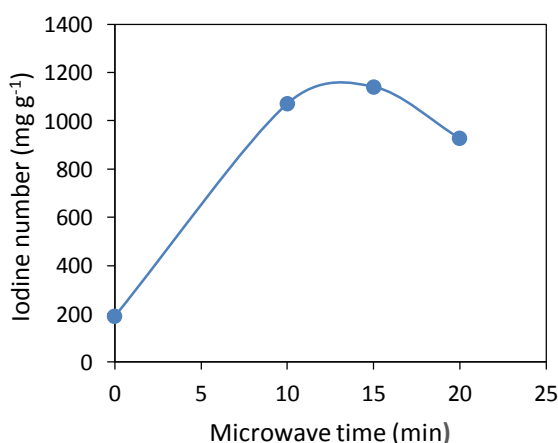


Figure 7. The change in the iodine numbers of activated carbons with microwave time (impregnation ratio 1:1; microwave power 250 W; activation temperature 500°C; activation time 45 min and CO₂).

When the microwave time was 10 and 15 min, the iodine number was observed as 1071 mg g⁻¹ and 1141 mg g⁻¹, respectively. However, when the microwave time was 20 min, the iodine number was 927 mg g⁻¹. The reason for this is thought to be that the microwave time of 10 min did not weaken the bonds between the activator and the raw material and did not diminish the viscosity of the activator sufficiently. When the microwave time is 20 min, it is thought that the activator disrupted the structure of the raw material. In other words, the viscosity of the activator was extremely reduced and consequently the pore structure of the raw material deteriorated. The best microwave duration was determined as 15 min.

After determining the best microwave parameters, the activation parameters were determined. The effect of the activation temperature was investigated under the conditions of 250 W microwave power, CO₂ gas medium in the microwave and 45 min activation time. The variation of the iodine numbers of activated carbons with the activation temperature is graphed in Figure 8.

When the activation temperature increased from 400°C to 500°C, it can be seen that the iodine number increases and then decreases. The possible cause of this is thought to be that the activation temperature of 400°C is not sufficient to open the pores in the activated carbon structure and 500°C is suitable to open the pores. It is thought that the activation temperature of 600°C causes to transform into the micropores of the macropores of the activated carbon. The best activation temperature was determined to be 500°C. Li and co-workers had found that the activation temperature was 500°C better in the synthesis of the active they obtained from rice husk. They stated that the pore structures collapsed at 600°C.¹⁷

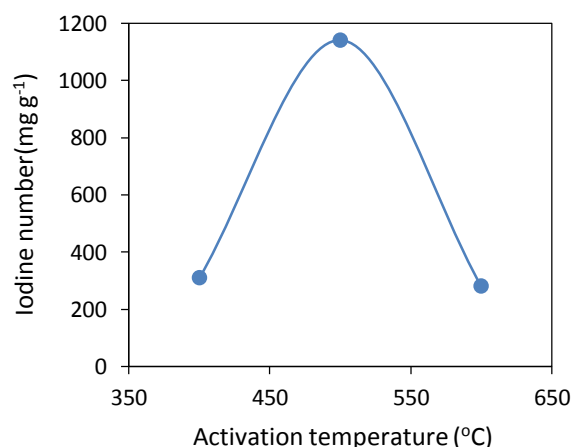


Figure 8. The variation of the iodine numbers of activated carbons with the activation temperature (impregnation ratio 1:1; microwave power 250 W; microwave time 15 min; activation time 45 min and CO₂).

The effect of activation time was investigated under 250 W microwave power, CO₂ gas environment and 500°C activation temperature. The change in the iodine number of the activated carbons with the activation time is graphed in Figure 9.

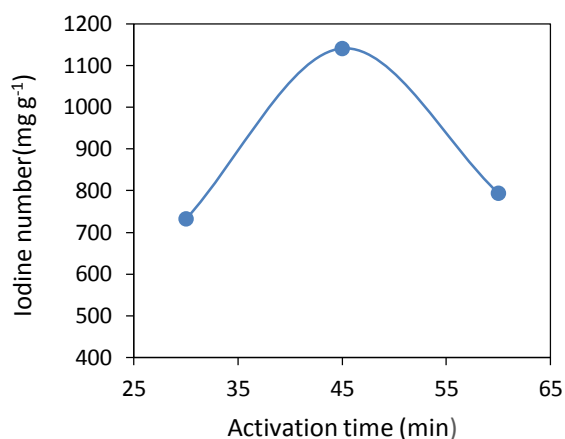


Figure 9. The change in the iodine number of the activated carbon with the activation time (impregnation ratio 1:1; microwave power 250 W; microwave time 15 min; activation temperature 500°C and CO₂).

When the activation time was 30, 45 and 60 min, the iodine number was determined to be 732 mg g⁻¹, 1141 mg g⁻¹ and 794 mg g⁻¹, respectively. This may be due to the fact that the activation time of 30 min is not sufficient to fully open the pores of activated carbon. When the activation time is 60 min, it is thought that the activated carbon pores turns into mesopores and the pore structure of activated carbon collapse. Özdemir and co-workers have found that the activation time in the activated carbon they obtained from grape stem using ZnCl₂ activator was 120 minutes at best.²⁰

4. CONCLUSIONS

In this study, microwave assisted activated carbon was synthesized from almond shell. In the synthesis of the activated carbon, the effects of different parameters such as gas medium, microwave power, microwave time, activation temperature, activation time and impregnation ratio in the microwave were investigated. The characterization of the synthesized activated carbons was carried out by SEM, BET and FTIR. The iodine numbers and methylene blue numbers of the synthesized activated carbons were determined. The iodine number of the microwave assisted activated carbon (70% activator/raw material ratio, 250 W microwave power, 15 min. microwave time, 500°C activation temperature and 45 min activation time) and activated carbon without microwave (70% activator/raw

material ratio, 500°C activation temperature and 45 min activation time) were determined to be 1141 mg/g and 190 mg/g, respectively. The BET surface area values of microwave assisted (70% activator/raw material ratio, 250 W microwave power, 15 min. microwave time, 500°C activation temperature and 45 min activation time) and without microwave activated carbon (70% activator/raw material ratio, 500°C activation temperature and 45 min. activation time) were determined to be 1105 m² g⁻¹ and 190 m² g⁻¹, respectively. The optimum conditions required to obtain activated carbon with the highest surface area can be listed as follows: CO₂ gas medium, 250 W microwave power, 15 min microwave time, 500°C activation temperature, 45 min activation time and 70% impregnation ratio. In previous studies in the literature, the microwave activation process was used in the synthesis of activated carbon with and without microwave treatment. Unlike these studies, microwave impregnation was applied in the present study. The BET surface area and iodine numbers show that microwave had a significant effect on the impregnation process.

ACKNOWLEDGEMENTS

This study was supported by Siirt University's Scientific Research Projects (BAP) Coordination Unit (Project No. 2017-SİÜFEB-95).

Conflict of interests

Authors declare that there is no a conflict of interest with any person, institute, company, etc.

REFERENCES

- Guo, J.; Luo, Y.; Lua, A. C.; Chi, R.-a.; Chen, Y.-l.; Bao, X.-t.; Xiang, S.-x. *Carbon* **2007**, 45 (2), 330-336.
- Al Bahri, M.; Calvo, L.; Gilarranz, M. A.; Rodríguez, J. J. *Chem. Eng. J.* **2012**, 203, 348-356.
- Crini, G. *Bioresour. Technol.* **2006**, 97 (9), 1061-1085.
- Baytar, O.; Şahin, Ö.; Horoz, S.; Kutluay, S. *Environ. Sci. Pollut. Res.* **2020**, 27 (21), 26191-26210.
- Karim, M. M.; Das, A. K.; Lee, S. H. *Anal. Chim. Acta* **2006**, 576 (1), 37-42.
- Kutluay, S.; Baytar, O.; Şahin, Ö. *J. Environ. Chem. Eng.* **2019**, 7 (2), 102947.
- Baytar, O.; Şahin, Ö.; Saka, C.; Ağrak, S. *Anal. Lett.* **2018**, 51 (14), 2205-2220.

8. Şahin, Ö.; Saka, C.; Ceyhan, A. A.; Baytar, O. *Sep. Sci. Technol.* **2015**, 50 (6), 886-891.
9. Şahin, Ö.; Saka, C.; Ceyhan, A. A.; Baytar, O. *Energ. Source. Part A* **2016**, 38 (12), 1756-1762.
10. İzgi, M. S.; Saka, C.; Baytar, O.; Saraçoğlu, G.; Şahin, Ö. *Anal. Lett.* **2019**, 52 (5), 772-789.
11. Baytar, O.; Şahin, Ö.; Saka, C. *Appl. Therm. Eng.* **2018**, 138, 542-551.
12. Şahin, Ö.; Saka, C.; Kutluay, S. *J. Ind. Eng. Chem.* **2013**, 19 (5), 1617-1623.
13. Kutluay, S.; Baytar, O.; Şahin, Ö. *Res. Eng. Struct. Mater.* **2019**, 5 (3), 279-298.
14. Şimşek, M.; Gülsoy, E. *Iğdır Üni. Fen Bilimleri Enst. Der.* **2017**, 7 (3), 19-29.
15. Saka, C.; Şahin, Ö.; Kutluay, S. *Energ. Source. Part A* **2016**, 38 (3), 339-346.
16. Temel, F.; Kutluay, S. *New J Chem* **2020**, 44 (30), 12949-12961.
17. Li, Y.; Ding, X.; Guo, Y.; Wang, L.; Rong, C.; Qu, Y.; Ma, X.; Wang, Z. *Mater. Chem. Phys.* **2011**, 127 (3), 495-500.
18. Liu, Q.-S.; Zheng, T.; Wang, P.; Guo, L. *Ind Crops Prod* **2010**, 31 (2), 233-238.
19. Sharif, Y. M.; Saka, C.; Baytar, O.; Şahin, Ö. *Anal. Lett.* **2018**, 51 (17), 2733-2746.
20. Ozdemir, I.; Şahin, M.; Orhan, R.; Erdem, M. *Fuel Process. Technol.* **2014**, 125, 200-206.



Natural bond orbital (NBO) population analysis and non-linear optical (NLO) properties of 2-(azepan-1-yl(naphthalen-1-yl)methyl)phenol

Yeliz ULAŞ*

Department of Chemistry, Faculty of Arts and Sciences, Bursa Uludağ University, Bursa, Turkey

Received: 11 June 2020; Revised: 15 August 2020; Accepted: 18 August 2020

*Corresponding author e-mail: yelizulas@uludag.edu.tr

Citation: Ulaş, Y. *Int. J. Chem. Technol.* 2020, 4 (2), 138-145.

ABSTRACT

All electronic properties of 2-(Azepan-1-yl (naphthalen-1-yl) methyl) phenol compound were investigated using the density functional theory (DFT) B3LYP method and 6-311 G(d, p) set. Natural bond orbital (NBO) analysis was used to learn the intermolecular and intermolecular binding interaction. Electron distribution was determined by natural population analysis. Nonlinear optical properties (dipole moment μ , polarizability α , and hyperpolarizability β) were investigated to determine the optical properties of the compound. Also, the effect of temperature on thermodynamic parameters (capacity, molar entropy, enthalpy) was reported.

Keywords: NBO, NLO, alkylaminophenol, DFT.

2- (Azepan-1-il (naftalen-1-il) metil) fenolün doğal bağ orbital (NBO) popülasyon analizi ve doğrusal olmayan optik (NLO) özellikleri

ÖZ

2-(Azepan-1-il (naftalin-1-il) metil) fenol bileşiğinin tüm elektronik özellikleri yoğunluk fonksiyonel teori (DFT) B3LYP yöntemi ve 6-311 G (d, p) seti kullanılarak araştırıldı. Moleküller arası ve moleküller arası bağlanma etkileşimini öğrenmek için doğal bağ orbital (NBO) analizi kullanıldı. Elektron dağılımı doğal popülasyon analizi ile belirlendi. Bileşiğin optik özelliklerini belirlemek için doğrusal olmayan optik özellikler (dipol moment μ , polarizabilite α , ve hiperpolarizabilite β) incelendi. Ayrıca, sıcaklığın termodinamik parametreler (kapasite, molar entropi, entalpi) üzerindeki etkisi rapor edildi.

Anahtar Kelimeler: NBO, NLO, alkilaminofenol, DFT.

1. INTRODUCTION

Alkylaminophenol compounds form a class of heterocyclic compounds used in various fields from pharmacology to polymer chemistry.¹⁻⁶ Generally, they are used as drug active material. Also, the phenolic groups have enabled them to have antioxidant activities too. Usually, they are used in chemotherapy for bone cancer treatment. These compounds are obtained generally by the petasis reaction. The reaction takes place by the removal of boric acid from the boronate complex formed by the boronic acid added to the medium after the amine and carbonyl compounds form iminium ion. The fact that the reaction conditions have mild provides it has been preferred in many applications. Although there are many publications on synthesized alkylaminophenols, there are limited studies

on its natural bond orbital (NBO), non-linear optical (NLO) and other physical properties. It has been observed in the literature that these compounds are not used outside of medical applications. Besides NBO, NLO is the most useful concept area because of their importance in optoelectronic applications. According to the literature survey, in an earlier study, 2-(Azepan-1-yl(naphthalen-1-yl)methyl)phenol compound which is an alkylaminophenol compound has been synthesized and calculated some of its properties.⁷

However, no any study has been reported on the NBO and NLO properties of 2-(Azepan-1-yl(naphthalen-1-yl)methyl)phenol compound so far. Therefore, this study has aimed to determine a NBO analysis of 2-(azepan-1-yl(naphthalen-1-yl)methyl) phenol compound using high-level theoretical methods. Herein, thermodynamic

parameters, standard molar heat capacity, standard molar enthalpy and standard molar entropy have been examined at different temperatures. Moreover NLO

parameters (linear polarizability, anisotropic polarizability and hyperpolarizability) have also been studied using the same method.

2. MATERIALS AND METHODS

2.1. Experimental and calculation methods

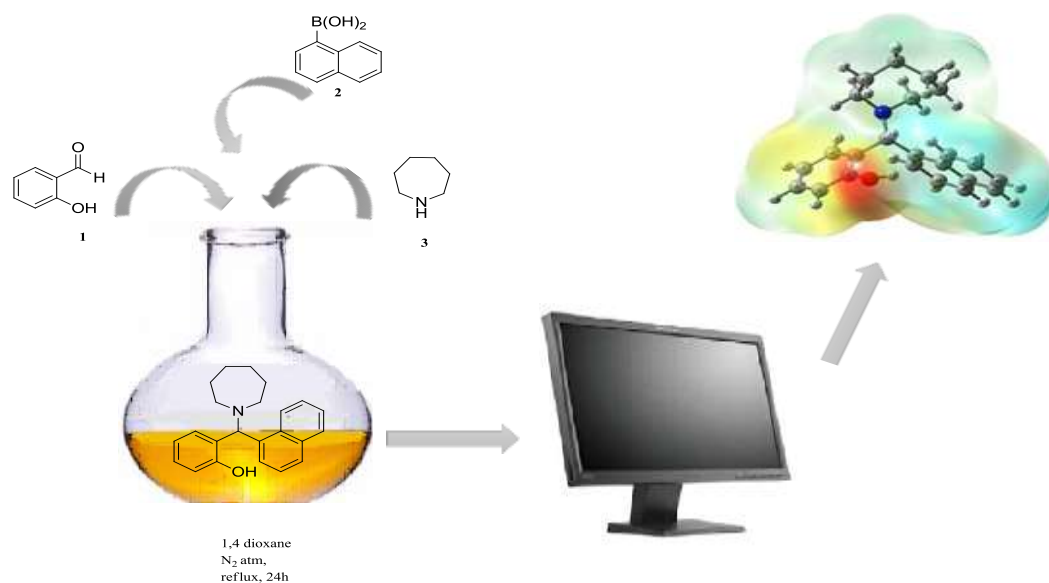


Figure 1. Synthesis and molecular electrostatic surface of 2-(Azepan-1-yl(naphthalen-1-yl)methyl)phenol.⁷

2-(Azepan-1-yl(naphthalen-1-yl)methyl)phenol compound was synthesized with petasis reaction. This reaction is a three-component reaction that takes place between aldehyde, amine and boronic acid and used in the previous study.⁷ After the experimental characterization of structural, some properties of the compound was determined using theoretical methods. Calculations include the B3LYP theory and 6-311 ++ G (d,p) set which is composed of Becke's three-parameter energy-functional hybrid approach and Lee-Yang and Parr's correlation function⁸ in the Gaussian 09W program. Gauss-View 5.0 program was used for molecular modelling.⁹

3. RESULTS AND DISCUSSION

3.1. Natural population analysis

NBO analysis provides all orbital information about electronic density and explains intra-and intermolecular interactions.¹⁰ Also, it gives us an idea of the electron

distributions in the lower shells of atomic orbitals. The distributions of electrons in the shells of atoms is as indicated in Table 1.

Considering Table 1, the highest electronegative charge is observed that is on the atoms of O11 and N33 with the values of -0.69040e and -0.57169e, and the highest electropositive charge is on H12 and C2 atoms with the values of 0.48133e and 0.31362e, Core: 49.97867 (99.9573% of 50), Valence: 127.39280 (99.5256% of 128), Rydberg: 0.61931 (0.3479% of 178).

3.2. Natural bond orbital (NBO) analysis

NBO analysis gives detailed information about the electron density of all orbitals of the molecule. This information is valuable in that it determines the most accurate Lewis structure for the compound, as well as explains both intermolecular and intermolecular interactions.¹¹⁻¹⁸ In this study; in the NBO analysis, a second-order Fock matrix was used to evaluate donor-acceptor interactions.¹⁹

Table 1. Natural charges and distribution of electrons to orbitals for selected atoms in the alkylaminophenol compound

Atom No	Natural Charge	Natural population (e)			
		Core	Valence	Rydberg	Total (e)
C1	-0.23941	1.99905	4.22253	0.01782	6.23941
C2	0.31362	1.99864	3.66366	0.02407	5.68638
C3	-0.09462	1.99889	4.07011	0.02562	6.09462
H8	0.21732	0	0.77935	0.00333	0.78268
H7	0.21603	0	0.78213	0.00184	0.78397
O11	-0.69040	1.99975	6.67768	0.01296	8.69040
H12	0.48133	0	0.51399	0.00467	0.51867
C34	0.08434	1.99903	3.88651	0.03012	5.91566
C35	0.03428	1.99901	3.93808	0.02863	5.96572
C36	-0.22711	1.99914	4.19483	0.03314	6.22711
C38	-0.10426	1.99909	4.07030	0.03487	6.10426
H42	0.20465	0	0.79129	0.00405	0.79535
H40	0.21538	0	0.78065	0.00397	0.78462
C13	-0.07347	1.99909	4.02393	0.05045	6.07347
H14	0.18465	0	0.81060	0.00475	0.81535
N33	-0.57169	1.99944	5.54474	0.02751	7.57169
C15	-0.16835	1.99920	4.14972	0.01943	6.16835
C16	-0.17097	1.99922	4.15126	0.02048	6.17097
H19	0.20578	0	0.79213	0.00209	0.79422
H22	0.20035	0	0.79751	0.00213	0.79965

The second-order Fock-matrix was carried out to evaluate the donor-acceptor interactions within the NBO basis. The interactions result in a lack of occupancy from the localized NBO of the idealized Lewis shape into an empty non-Lewis orbital. For every donor (i) and acceptor (j) the stabilization energy (E2) associated with the delocalization $i \rightarrow j$ is decided by the subsequent equation:

$$E(2) = \Delta E_{i,j} = q_i [F_{(i,j)}^2] / [E_i - E_j] \quad (1)$$

Looking at Table 2, it is seen that s-type and p-type subshells contribute to all orbitals. p-type subshell was contributed to C2-C3 antibonding orbital. Also, p-type subshell was contributed to LP N33 orbital, s and p subshell was contributed to LP O11 orbital too. When the occupancy values are examined, it is seen that sp hybridization is dominant in the binding orbitals for the compound.

Table 2. Natural atomic orbital occupancies of most interacting NBOs of alkylaminophenol compound along with their percentage of some selected hybrid atomic orbitals

Bonds	Occupancies (e)	Hybrids	AO (%)
σ N33-C13	1.97937	$sp^{3.27}$	s(23.4%) p(76.5%) d(0.10%)
σ C13-H14	1.97170	$sp^{3.44}$	s(22.52%) p(77.4%) d(0.08%)
σ C2-O11	1.99352	$sp^{3.15}$	s(24.03%) p(75.74%) d(0.22%)
σ O11-H12	1.98303	$sp^{3.52}$	s(22.09%) p(77.81%) d(0.09%)
σ C3-C13	1.96326	$sp^{2.20}$	s(31.2%) p(68.77%) d(0.04%)
σ C2-C3	1.97340	$sp^{1.59}$	s(38.54%) p(61.42%) d(0.04%)
σ C13-C34	1.95385	$sp^{2.66}$	s(27.31%) p(72.65%) d(0.04%)
σ C34-C35	1.94128	$sp^{1.87}$	s(34.77%) p(65.15%) d(0.08%)
σ N33-C15	1.98281	$sp^{3.20}$	s(23.8%) p(76.07%) d(0.13%)
LP N33	1.86844	$sp^{11.2}$	s(8.32%) p(91.66%) d(0.02%)
LP O11	1.97721	$sp^{1.39}$	s(41.84%) p(58.12%) d(0.03%)
σ^* N33-C13	0.03966	$sp^{3.27}$	s(23.4%) p(76.5%) d(0.10%)
σ^* C13-H14	0.03932	$sp^{3.44}$	s(22.52%) p(77.4%) d(0.08%)
σ^* C2-O11	0.02418	$sp^{3.15}$	s(24.03%) p(75.74%) d(0.22%)
σ^* O11-H12	0.01053	$sp^{3.52}$	s(22.09%) p(77.81%) d(0.09%)
σ^* C3-C13	0.03650	$sp^{2.20}$	s(31.20%) p(68.77%) d(0.04%)
σ^* C2-C3	0.39261	$sp^{1.0}$	s(0%) p(99.95%) d(0.04%)
σ^* C13-C34	0.02957	$sp^{2.66}$	s(27.31%) p(72.65%) d(0.04%)
σ^* C34-C35	0.02433	$sp^{1.87}$	s(34.77%) p(65.15%) d(0.08%)
σ^* N33-C15	0.02661	$sp^{3.20}$	s(23.8%) p(76.07%) d(0.13%)

In NBO analysis, the large $E(2)$ value indicates the intense interaction between electron donors and receptors. The O11-H12 bond in the phenyl ring has been found to interact strongly with the naphthalene ring and heterocyclic structure. As seen in Table 3, the molecule; the O11-H12 donor has the highest energy value with $486.90 \text{ kcal mol}^{-1}$ where C41-C46 is the acceptor, the O11 donor has the lowest value for the C1-C2 acceptor with $0.51 \text{ kcal mol}^{-1}$.

3.3 Non-linear optical (NLO) analysis

Nonlinear optical (NLO) properties of materials plays

an important role in the design of electronic structure.

NLO properties of a compound are originated from π electrons. Increased conjugation or inclusion of donor groups changes NLO properties. In general, quantum chemical calculations explain the relationship between the electronic structure and NLO properties.^{16,20-24} One of the compounds used for investigation of NLO properties of molecular systems is p-nitroaniline, thus p-nitroaniline was chosen for the reference compound in this work. NLO properties of alkylaminophenol compounds have never been studied in the literature before.

Table 3. Second-order perturbation theory analysis of Fock matrix in NBO basis for selected chemical bonds

NBO(i) (Donor Lewis)	NBO(j) (Acceptor non Lewis)	E(2) kcal mol ⁻¹	E(j)-E(i) a.u	F(i,j) a.u	NBO(i) (Donor Lewis)	NBO(j) (Acceptor non Lewis)	E(2) kcal mol ⁻¹	E(j)-E(i) a.u	F(i,j) a.u	
σC2-O11	σ*C1-C2	0.57	1.48	0.026	σO11-H12	σ*C35-C37	8.30	1.11	0.086	
	σ*C1-C6	1.31	1.59	0.041		σ*C41-C46	486.90	0.12	0.216	
	σ*C2-C3	1.02	1.49	0.035		σC13-C34	σ*C2-C3	1.62	1.30	0.041
	σ*C3-C4	1.55	1.48	0.043		σ*C3-C13	0.53	1.10	0.022	
σC3-C13	σ*C1-C2	2.31	1.19	0.047	σ*C13-C34	0.55	1.02	0.021		
	σ*C2-C3	1.50	1.20	0.038	σ*C16-C21	0.58	0.79	0.019		
	σ*C4-C5	2.42	1.20	0.048	σ*C16-N33	0.59	1.04	0.022		
	σ*C13-N33	0.71	0.82	0.022	σ*C34-C36	0.79	0.67	0.022		
	σ*C34-C36	1.82	0.58	0.031	σ*C41-C46	1.93	0.04	0.008		
σO11-H12	σ*C1-C2	1.57	1.36	0.041	nO11	σ*C1-C2	0.51	1.16	0.022	
	σ*C13-N33	9.40	0.99	0.087	σ*C2-C3	6.12	1.18	0.076		
	σ*C13-C34	3.77	1.10	0.058	σ*C2-C3	18.32	0.43	0.086		
	σ*C15-H19	4.14	1.50	0.070	nN33	σ*C3-C13	2.67	0.65	0.038	
	σ*C16-N33	1.25	1.12	0.033	σ*C15-H19	1.25	0.97	0.032		
	σ*C16-H21	18.21	0.86	0.120	σ*C16-C20	9.81	0.58	0.069		
	σ*C20-H28	10.94	0.98	0.092	σ*C16-H21	2.00	0.33	0.024		
	σ*C23-C26	140.71	0.31	0.185	σ*C16-H22	3.07	0.68	0.042		
	σ*C26-H32	30.41	0.73	0.133						

Isotropic linear polarizability $\langle\alpha\rangle$, anisotropic linear polarizability $\Delta\alpha$, first-order hyperpolarizability $\langle\beta\rangle$ and total dipole moment (μ) values were calculated by B3LYP method.

(μ), $\langle\alpha\rangle$, $\Delta\alpha$ (β) values were calculated by the use of the subsequent equations:²⁵

$$\mu = (\mu_x^2 + \mu_y^2 + \mu_z^2)^{1/2}$$

$$\langle\alpha\rangle = 1/3(\alpha_{xx} + \alpha_{yy} + \alpha_{zz})$$

$$\Delta\alpha = [1/2((\alpha_{xx} - \alpha_{yy})^2 + (\alpha_{yy} - \alpha_{zz})^2 + (\alpha_{zz} - \alpha_{xx})^2)]^{1/2}$$

$$\langle\beta\rangle = [(\beta_{xxx} + \beta_{xvy} + \beta_{xzz})^2 + (\beta_{yyy} + \beta_{xyy} + \beta_{yzz})^2 + (\beta_{zzz} + \beta_{xzz} + \beta_{yyz})^2]^{1/2}$$

NLO data by the DFT / B3LYP / 6-311 ++ G (d, p) method of p-NA selected as standard with alkylaminophenol compound were shown in Table 4.

Linear polarizability values are negative, indicating that there is a dipole in the opposite direction of the electrical field. Linear polarizability value of selected alkylaminophenol is 2.5 times of p-NA. In anisotropic linear polarizability value is higher than p-NA. When the first order hyperpolarizability values are examined, it is seen that the alkylaminophenol compound is lower than the hyperpolarizability value of p-NA.

Table 4. NLO values of the alkylaminophenol compound

Property	p-NA	B3LYP	Property	p-NA	B3LYP
μ_x	-7.4519	-1.5179	β_{xxx}	-99.4560	-35.7077
μ_y	-0.001	1.3048	β_{yyy}	16.7004	18.5251
μ_z	0.6869	1.0776	β_{zzz}	12.9992	-13.0982
μ	7.4835 Debye	2.2733 Debye	β_{yyz}	-0.0012	16.9110
α_{xx}	-58.7480	-141.5996	β_{xxy}	-0.0004	-29.8279
α_{yy}	-53.2767	-150.3433	β_{yzz}	0.0001	2.6038
α_{zz}	-60.6128	-148.7810	β_{zzz}	0.4969	12.0045
$\langle\alpha\rangle$	-8.52×10^{-24} esu	-2.18×10^{-23} esu	β_{xzz}	12.9100	-2.9584
			β_{yyz}	0.4172	3.7631
$\Delta\alpha$	9.79×10^{-25} esu	1.20×10^{-24} esu	$\langle\beta\rangle$	8.99×10^{-31} esu	2.98×10^{-31} esu

Alkylaminophenol compound can be considered worthy of study as a material for NLO applications according to results and suggested for the second-order non-linear optical research.

3.4 Thermodynamic properties

Some thermodynamic parameters of alkylaminophenol compound have been calculated in the previous study.⁷

In our study, the heat capacity, $C_{p,m}^0$, entropy, S_m^0 and enthalpy, H_m^0 values were calculated^{26,27} under 1 atm pressure at different temperature values varying from 100 to 500 K) and the results obtained are listed in Table 5.

Correlation dependencies are also given in Figure 2.

Table 5. Temperature dependence of thermodynamic properties of the alkylaminophenol compound

Temperature (K)	Heat Capacity (C)	Entalpy (H)	Entropy (S)
100	30.947	-1021.3010	91.857
200	56.727	-1021.2937	122.353
298.15	86.184	-1021.2823	151.194
400	116.700	-1021.2655	181.437
500	142.635	-1021.2443	210.796

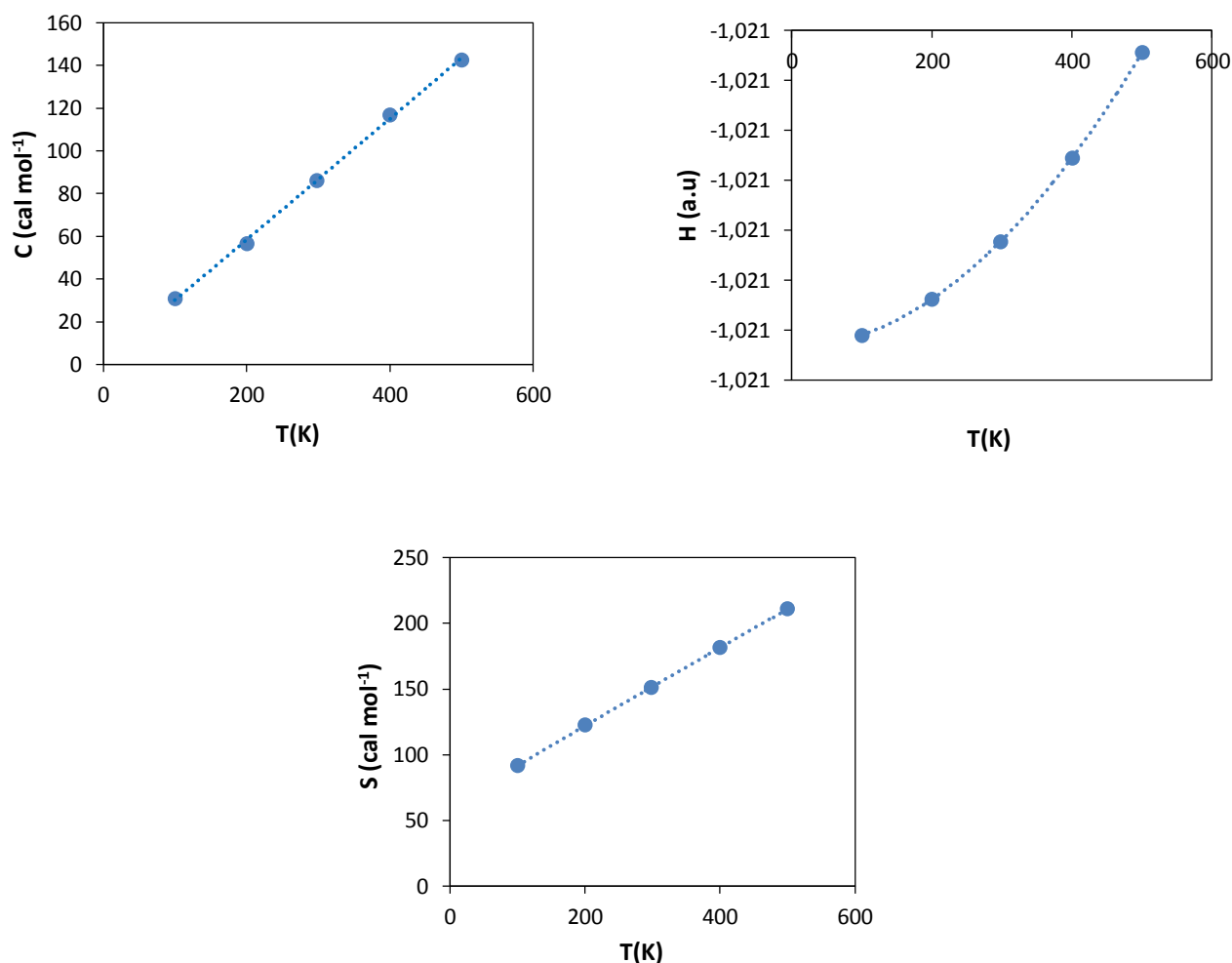


Figure 2. Correlation graph for thermodynamic parameters of 2-(Azepan-1-yl(naphthalen-1-yl)methyl)phenol compound.

Additionally, the correlation equations as functions of temperature and corresponding correlation coefficients are given below in follows for the 2-(Azepan-1-yl(naphthalen-1-yl)methyl)phenol compound.

$$C (\text{Cal mol}^{-1} \text{K}^{-1}) = 1.8991 + 0.282 T + 2 \times 10^{-6} T^2 \quad (R^2 = 0.999)$$

$$H (\text{a.u.}) = -1021.3 + 2 \times 10^{-6} T + 2 \times 10^{-7} T^2 \quad (R^2 = 1)$$

$$S (\text{Cal mol}^{-1} \text{K}^{-1}) = 61.562 + 0.3054 T + 1 \times 10^{-5} T^2 \quad (R^2 = 1)$$

4. CONCLUSIONS

In this study, NPA, NBO, NLO and thermodynamic parameters of the alkylaminophenol compound were calculated by DFT/B3LYP/6-311++G(d,p) method. The

natural population analysis has given information about the distribution of electrons to orbitals to understand the structure. The NBO analysis has provided the details of the type of hybridization and the nature of bonding in alkylaminophenol compound. Also, the dipole moment, polarizability, first-order hyperpolarizability values were calculated. A standard material p-NA (p-nitroaniline) was used for NLO properties. Alkylaminophenol compounds can be considered as a material for NLO applications according to the results. In addition, it has been seen with correlations that the temperature is effective on thermodynamic parameters such as enthalpy, entropy, and heat capacity.

ACKNOWLEDGEMENTS

This study was supported with KUAP(F)-2016/5 project by Bursa Uludag University Scientific Research Projects Unit.

Conflict of interests

Author declares that there is no a conflict of interest with any person, institute, company, etc.

REFERENCES

1. Wang, R.; Xu, J.. *Arkivoc* **2010**, 2010 (9), 293-299.
2. Ulaş, Y.; Özkan, A. İ.; Tolan, V. *Eur. J. Sci. Technol.* **2019**, 16, 701-706.
3. Ulaş, Y. *Eur. J. Sci. Technol.* **2019**, 16, 242-246.
4. Doan, P.; Anufrieva, O.; Yli-Harja, O.; Kandhavelu, M. *Eur. J. Pharmacol.* **2018**, 820, 229-234.
5. Doan, P.; Nguyen, T.; Yli-Harja, O.; Kandhavelu, M.; Yli-Harja, O.; Doan, P.; Nguyen, T.; Yli-Harja, O.; Candeias, N. R. *Eur. J. Pharm. Sci.* **2017**, 107, 208–216.
6. Neto, Í.; Andrade, J.; Fernandes, A. S.; Pinto Reis, C.; Salunke, J. K.; Priimagi, A.; Candeias, N. R.; Rijo, P. *ChemMedChem* **2016**, 11, 2015-2023.
7. Ulaş, Y. *Eur. J. Sci. Technol.* **2020**, 18, 574-582.
8. Becke, A. D. *Phys. Rev. A* **1988**, 38 (6), 3098-3100.
9. Eryilmaz, S.; Gül, M.; Kozak, Z.; Inkaya, E. *Acta Phys. Pol. A* **2017**, 132 (3), 738-741.
10. Theivarasu, C.; Murugesan, R. *Int. J. Chem. Sci* **2016**, 14 (4), 2029-2050.
11. Gladis Anitha, E.; Joseph Vedhagiri, S.; Parimala, K. *Spectrochim. Acta - Part A Mol. Biomol. Spectrosc.* **2015**, 140, 544-562.
12. Demircioğlu, Z.; Albayrak, Ç.; Büyükgüngör, O. *J. Mol. Struct.* **2014**, 1065–1066 (1), 210-222.
13. Prasad, M. V. S.; Chaitanya, K.; UdayaSri, N.; Veeraiah, V. *J. Mol. Struct.* **2013**, 1047, 216-228.
14. Soliman, S. M. *J. Mol. Struct.* **2013**, 1048, 308-320.
15. Govindarajan, M.; Karabacak, M. *Spectrochim. Acta - Part A Mol. Biomol. Spectrosc.* **2012**, 96, 421-435.
16. Gültekin, Z.; Demircioğlu, Z.; Frey, W.; Büyükgüngör, O. *J. Mol. Struct.* **2020**, 1199, 126970-126988.
17. Mathammal, R.; Sudha, N.; Guru Prasad, L.; Ganga, N.; Krishnakumar, V. *Spectrochim. Acta - Part A Mol. Biomol. Spectrosc.* **2015**, 137, 740-748.
18. Subashini, K.; Govindarajan, R.; Surendran, R.; Mukund, K.; Periandy, S. *J. Mol. Struct.* **2016**, 1125, 576-591.
19. Pir, H.; Günay, N.; Avcı, D.; Atalay, Y. *Spectrochim. Acta - Part A Mol. Biomol. Spectrosc.* **2012**, 96, 916-924.
20. Sharma, K.; Melavanki, R.; Patil, S. S.; Kusanur, R.; Patil, N. R.; Shelar, V. M. *J. Mol. Struct.* **2019**, 1181, 474-487.
21. Balachandran, V.; Parimala, K.. *Spectrochim. Acta - Part A Mol. Biomol. Spectrosc.* **2013**, 102, 30-51.
22. Nalini, H.; Vincent, V. C.; Bakiyaraj, G.; Kirubavathi, K.; Selvaraju, K. *Physica B: Phys. Condens. Matter* **2020**, 592, 412245.
23. Sylaja, B.; Gunasekaran, S.; Srinivasan, S. *Optik (Stuttg.)* **2016**, 127 (12), 5055-5064.
24. Pandey, M.; Muthu, S.; Nanje Gowda, N. M. *J. Mol. Struct.* **2017**, 1130, 511-521.
25. Uludağ, N.; Serdaroğlu, G. *J. Mol. Struct.* **2018**, 1155, 548-560.
26. Küçük, İ.; Kaya, Y. *J. Inno Sci. Eng;* **2018**; 2 (2), 81-96.
27. Kucuk, I.; Kaya, Y.; Kaya, A. A. *J. Mol. Struct.* **2017**, 1139, 308-318.



Synthesis of magnetic Fe₃O₄/AC nanoparticles and its application for the removal of gas-phase toluene by adsorption process

Sinan KUTLUAY^{1,*}, Mehmet Şakir ECE², Ömer ŞAHİN¹

¹Department of Chemical Engineering, Faculty of Engineering, Siirt University, Siirt 56100, Turkey

²Vocational High School of Health Services, Mardin Artuklu University, Mardin 47100, Turkey

Received: 21 June 2020; Revised: 04 September 2020; Accepted: 05 September 2020

*Corresponding author e-mail: sinankutluay@siirt.edu.tr

Citation: Kutluay, S.; Ece, M. Ş.; Şahin, Ö. *Int. J. Chem. Technol.* 2020, 4 (2), 146-155.

ABSTRACT

In this study, we present the first application of magnetic Fe₃O₄ functionalized with activated carbon (Fe₃O₄/AC) as nano-adsorbent for the removal of gas-phase toluene by adsorption process. Magnetic Fe₃O₄/AC was synthesized via co-precipitation method within the framework of nanotechnology principles. Then, the effects of process conditions such as contact time, initial toluene concentration, and temperature on the adsorption capacity of toluene by the magnetic Fe₃O₄/AC were investigated using the response surface methodology (RSM). The obtained magnetic Fe₃O₄/AC was characterized using scanning electron microscopy (SEM), fourier transform infrared spectroscopy (FTIR) and thermogravimetric (TG) analysis. The maximum adsorption capacity of the magnetic Fe₃O₄/AC for the adsorption of the toluene was determined as 312.99 mg g⁻¹ under optimal process conditions such as 59.48 min contact time, 17.21 mg l⁻¹ initial toluene concentration, and 26.01°C temperature. The adsorption by the magnetic Fe₃O₄/AC indicated the best fit with the Langmuir isotherm model, and obeyed the pseudo-second-order (PSO) kinetic model. This study indicated that magnetic Fe₃O₄/AC could be applied as an adsorbent for the removal of gas-phase toluene.

Keywords: Nanotechnology, magnetic nano-adsorbents, response surface methodology, adsorption, toluene.

Manyetik Fe₃O₄/aktif karbon nanoparçacıklarının sentezlenmesi ve adsorpsiyon prosesi ile gaz-fazındaki toluenin giderilmesi için uygulanması

ÖZ

Bu çalışmada, gaz-fazı toluenin adsorpsiyon prosesi ile giderilmesi için nano-adsorbent olarak aktif karbon ile fonksiyonelleştirilmiş manyetik Fe₃O₄ (Fe₃O₄/AC)'nin ilk uygulamasını sunuyoruz. Manyetik Fe₃O₄/AC, nanoteknoloji prensipleri çerçevesinde birlikte çöktürme yöntemi ile sentezlendi. Daha sonra, temas süresi, başlangıç toluen konsantrasyonu ve sıcaklık gibi proses koşullarının toluenin manyetik Fe₃O₄/AC ile adsorpsiyonu üzerindeki etkileri yanıt yüzeyi yöntemi (RSM) kullanılarak incelendi. Elde edilen manyetik Fe₃O₄/AC, taramalı elektron mikroskopisi (SEM), fourier dönüşümü kızılötesi spektroskopisi (FTIR) ve termogravimetrik (TG) analiz kullanılarak karakterize edildi. Toluenin adsorpsiyonu için manyetik Fe₃O₄/AC' nin maksimum adsorpsiyon kapasitesi, 59,48 dakika temas süresi, 17,21 mg l⁻¹ başlangıç toluen konsantrasyonu ve 26,01°C sıcaklıktaki proses koşulları altında 312,99 mg g⁻¹ olarak belirlendi. Manyetik Fe₃O₄/AC tarafından adsorpsiyon, Langmuir izoterm modeli ile en iyi uyumu gösterdi ve sözde ikinci dereceden (PSO) kinetik modele uydu. Bu çalışma, manyetik Fe₃O₄/AC'nin, gaz-fazı toluenin giderilmesi için bir adsorbent olarak uygulanabileceğini gösterdi.

Anahtar Kelimeler: Nanoteknoloji, manyetik nano-adsorbentler, yanıt yüzey metodu, adsorpsiyon, toluen.

1. INTRODUCTION

Volatile organic compounds (VOCs), which cause even adverse health problems such as cancer, are a major component of atmospheric pollutants. VOCs are important air pollutants because of such detrimental

effects as allergic reactions, nausea, throat irritation, nose, eye and headache. Besides, they cause dangerous environmental problems such as photochemical smog, suspended particulate matter, stratospheric ozone depletion and global warming. Among VOCs, toluene pollutes the air because of tanning processes, some

printing processes, adhesives, paints, wastewater, industrial activities and automobiles. Also, toluene is a chemical with high motility, toxicity, carcinogenicity, and teratogenicity. The accumulation of toluene in the air, food chain and groundwater endangers the security of both people and the ecosystem. World Health Organization (WHO) has declared in 1986 that because of its chronic effect on human health, the toluene concentration should not exceed 0.2–0.4 mg l⁻¹. Hence, toluene needs to be eliminated in order to preserve both human health and the environment.¹⁻⁴

Industrial sectors considerably intrude the gas rates in the air. Adverse effects on air quality affect health negatively. It is a vital requirement to decrease the infiltration of poisonous gases in the atmosphere and to develop reduction strategies. Therefore, pollutant removal methods have become indispensable. There are various techniques have been widely used for the removal of VOC pollutants.⁵⁻⁶ Among these techniques, the adsorption is one of the least harmful process as well as high yield, cheap, simplicity, and renewable properties.⁷⁻⁹ In this sense, nanotechnology offers more unusual and impressive solutions than other traditional methods in adsorption technology, as in all other fields. Fe₃O₄ is a common material widely examined in nanotechnological researches. It has attracted considerable attention because of its magnetic properties such as biocompatibility, low-toxicity, low cost and high surface area. It efficiently solves different analytical and industrial problems. Fe₃O₄ presents high surface areas for adsorption, helps recovery due to its magnetic property, and most importantly, it has low toxicity. It is a green and secure option for environmental improvement because of its unique properties such as size, surface area, absorptivity, electronic and catalytic properties.¹⁰

This study focused on the application of the toluene adsorption by the magnetic Fe₃O₄/AC as nano-adsorbent. In this context, the effects of process conditions such as contact time, initial toluene concentration, and temperature on the adsorption capacity of toluene were investigated. The obtained magnetic Fe₃O₄/AC was characterized using scanning electron microscopy (SEM), fourier transform infrared spectroscopy (FTIR) and thermogravimetric (TG) analysis. Also, the kinetics process of toluene adsorption was evaluated using kinetic models. Equilibrium adsorption data of toluene were defined by isotherm models.

2. MATERIALS AND METHODS

2.1. Materials

Iron (III) chloride hexahydrate (FeCl₃·6H₂O) and

activated carbon (AC, Z29CO045) were supplied from Merck Chemical. Iron (II) chloride tetrahydrate (FeCl₂·4H₂O) was bought from ALFA AESAR Chemical Company. Ethanol (CH₃CH₂OH) from Sigma-Aldrich Chemical Companies. Ammonia (NH₃) from VWR Chemicals. All chemicals and solvents and toluene (99.0%) used as adsorbate provided from Sigma Aldrich, and they have analytical purity.

2.2. Synthesis of the magnetic Fe₃O₄/AC

The magnetic Fe₃O₄/AC was synthesized applying the co-precipitation method, which is a straight forward and convenient approach. In magnetic Fe₃O₄/AC synthesis, a mixture of 4 mmol FeCl₃·6H₂O and 2 mmol FeCl₂·4H₂O was distributed stoichiometrically in a mixture of 50 ml deionized-distilled water in a way that Fe⁺²/Fe⁺³ ratio would be 1/2, and AC was added in the mixture with an amount that the mass ratio of (Fe⁺²+Fe⁺³)/(AC) would be 4/1. It was sonicated for 10 min. 10 ml NH₃ solution was added drop by drop to obtain co-precipitation. Amalgamating was continued under argon at 50°C for 30 min. The Fe₃O₄/AC obtained as a product was isolated from the medium by magnetic separation. Then Fe₃O₄/AC washed several times with deionized-distilled water and ethanol. Immediately after, the Fe₃O₄/AC was dried in a vacuum oven for 20 h at 50°C.¹¹ The synthesis of magnetic Fe₃O₄/AC is displayed schematically in Figure 1.

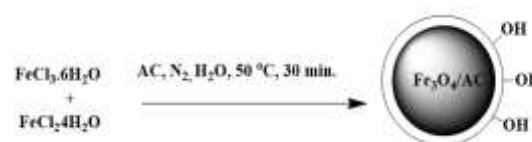


Figure 1. Schematic representation of the synthesis of magnetic Fe₃O₄/AC.

2.3. Gas-phase adsorption of toluene

Detailed information for the dynamic adsorption of toluene by the magnetic Fe₃O₄/AC was presented in the previously published procedure.¹² The capacity of the magnetic Fe₃O₄/AC to adsorb toluene was estimated at atmospheric pressure. The flow rate of the gas (N₂) employed as the carrier during the adsorption process was 100 ml min⁻¹. The optimum amount of magnetic Fe₃O₄/AC was 80 mg.

The adsorption capacity was estimated with Eq. (1) presented below:¹³

$$q = \frac{F}{m} \int_0^t (C_{in} - C_{eff}) dt \quad (1)$$

In this situation, m (g) is the amount of the magnetic

$\text{Fe}_3\text{O}_4/\text{AC}$. F (l min^{-1}) is the gas flow rate, t (min) is the contact time. C_{in} and C_{eff} (mg l^{-1}) are the initial and out toluene concentrations, respectively, q (mg g^{-1}) is the adsorption capacity.

2.4. Characterization

The surface characteristics of the synthesized magnetic $\text{Fe}_3\text{O}_4/\text{AC}$ were recorded with an FTIR (Bruker Vertex 70) spectrometer in the range of $4000\text{-}400\text{ cm}^{-1}$. The magnetic $\text{Fe}_3\text{O}_4/\text{AC}$ surface morphology was characterized by SEM (Zeiss EVO 50 Model) analysis. TG thermogram accomplished with Shimadzu DTG-60 was conducted to define the formation of the magnetic $\text{Fe}_3\text{O}_4/\text{AC}$ and the number of functional groups appended to the surface. Mathematical modeling, statistical analysis, and optimization studies for experimental data were conducted by employing Design Expert 12.0.8.0 Software (Free Trial Version).

3. RESULTS AND DISCUSSION

3.1. Characterization of the magnetic $\text{Fe}_3\text{O}_4/\text{AC}$

Characterization of the magnetic $\text{Fe}_3\text{O}_4/\text{AC}$ was conducted by FTIR, TG, and SEM analysis. SEM images, FTIR spectra, and TG thermogram of the synthesized magnetic $\text{Fe}_3\text{O}_4/\text{AC}$ were presented in Figures 2-4, respectively.

3.1.1. SEM analysis

The SEM microstructure image of AC was presented in Figure 2a. As observed in Figure 2a, AC has surface roughness. Various sizes of heterogeneous pores and cavities are clearly noticeable on the AC surface. The SEM microstructure image of the magnetic $\text{Fe}_3\text{O}_4/\text{AC}$ is presented in Figure 2b. When the magnetic $\text{Fe}_3\text{O}_4/\text{AC}$ microstructure image was analyzed, it was observed that the general pore formation was rough and spongy. It was understood that the intrusions, protrusions, and roughness increased the surface area in the magnetic $\text{Fe}_3\text{O}_4/\text{AC}$ microstructure compared to the microstructure of AC.

3.1.2. FT-IR analysis

FTIR spectrum of the magnetic $\text{Fe}_3\text{O}_4/\text{AC}$ is presented in Figure 3. As observed in Figure 3, the peak at 550 cm^{-1} which is the characteristic for Fe_3O_4 , indicates the presence of Fe-O bonds. Still, the peaks at 3448 cm^{-1} and 1404 cm^{-1} indicate the stress and vibration peaks of O-H, respectively. The peak at 1656 cm^{-1} shows the vibration peak of the C-C bond, and the peak at 1118 cm^{-1} shows the vibration peak of the C-O bond.

The determined peak values are in accordance with the values presented in the literature.¹⁴

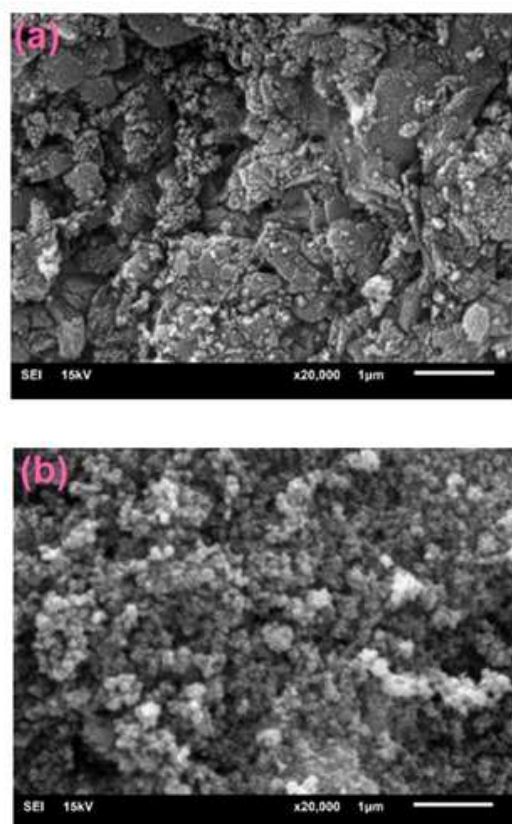


Figure 2. SEM images of a) AC, b) Magnetic $\text{Fe}_3\text{O}_4/\text{AC}$.

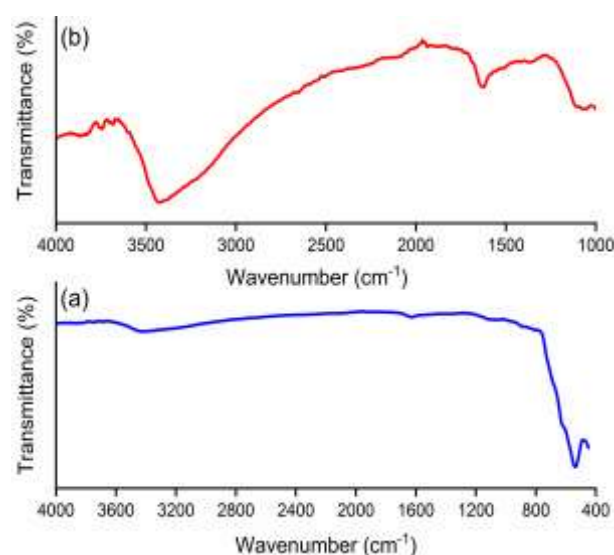


Figure 3. FT-IR spectra of a) the magnetic $\text{Fe}_3\text{O}_4/\text{AC}$, b) $\text{Fe}_3\text{O}_4/\text{AC}$.

3.1.3. TG analysis

TG analysis is a technique, as a function of temperature under a controlled atmosphere, applied to determine the weight changes of a sample. The thermal stability of a sample can also be observed practicing TG analysis. The TG curve of the magnetic Fe₃O₄/AC is presented in Figure 4.

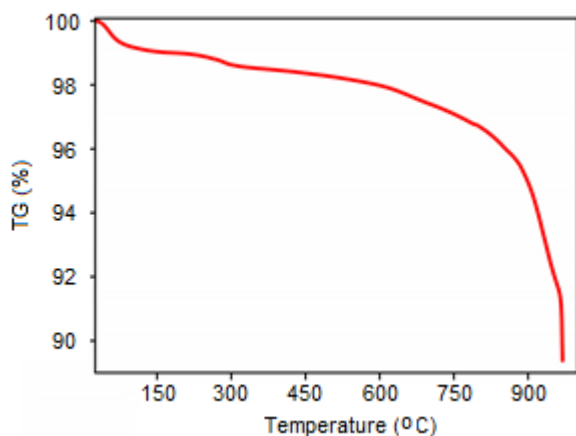


Figure 4. TG curve of the magnetic Fe₃O₄/AC.

As seen in Figure 4, the percentage of magnetic Fe₃O₄/AC's TG temperature-weight loss graph is approximately 10.6%. This percentage summarized the magnetic Fe₃O₄/AC residue after the decomposition stage in the thermogram, with a limited reduction in thermal stability. The loss between 25-540°C is a consequence of volatile organic compounds and water loss remaining in the sample. The loss between 500-970°C is related to low decomposition.

3.2. Experimental design, statistical analysis and optimization for the adsorption of toluene

In this study, RSM, which is an experimental method for the development, improvement, and optimization of the design process, was applied to determine the importance of the potential interactions of the functioning parameters. The approach of RSM-based central composite design (CCD) was employed to perform statistical analyses and obtain the regression model. Statistically significant model parameters were determined by using the variance analysis (ANOVA). For the study, the effects of parameters such as contact time (A), initial toluene concentration (B), and temperature (C) were analyzed. The values of the design points of the parameters are presented in Table 1. Table 2 show the parameter values for 17 experiments in the CCD experimental design and the capacities of the

magnetic Fe₃O₄/AC for the toluene adsorption obtained according to the experimental and predicted model.

The adsorption capacity of the magnetic Fe₃O₄/AC for the toluene adsorption was statistically analyzed employing ANOVA, and the results obtained are presented in Table 3. ANOVA shows which factor is most significant in an experimental design. It also defines the relationship between the factors studied and provides information about whether the results of the experiment are significant.¹⁵ The validity and reliability of the proposed model are assessed according to p-value, F-value, correlation coefficients (R²), and adeq precision results. In other words, the proposed model was suitable in the situation indicating p < 0.05, F > 4, R² > 0.95, and adeq precision > 4. As seen in Table 3, when the ANOVA results obtained for the magnetic Fe₃O₄/AC capacity for the toluene adsorption were analyzed, it was observed that A, B, and C were important model terms (p < 0.05). The high value of the correlation coefficient (R² = 0.98) for the adsorption capacity signified evidence of a good fit between the experimental data and the model. The R² value of 98% means that 99% of the total variation for the adsorption capacity was represented by variable factors.¹⁶ Besides, the F-value of 49.96 and adeq precision results of 22.44 indicated that the proposed model well defined experimental data. Moreover, the fact that the experimental and model adsorption capacity values presented in Table 2 were very close to each other verified the validity and reliability of the proposed model.

The contour (2D) plots of the interaction effects of the two factors on the capacity of the magnetic Fe₃O₄/AC for the toluene adsorption are presented in Figure 5. As seen in Figure 5a, adsorption capacity increased with increasing contact time. The number of active sites on the nano-adsorbent surface can be regarded as the reason for this situation.¹⁷ It was seen that the adsorption capacity did not significantly change with increasing initial toluene concentration. Figure 5b presents the relationship between contact time and temperature. The highest adsorption capacity was seen at a high contact time and low temperature. Notably, the amount of temperature had an essential effect on the adsorption capacity. ANOVA results supported this situation. When the surface plot for the initial toluene concentration versus temperature (Figure 5c) was considered, it was evident that the initial toluene concentration did not have a meaningful effect on the adsorption capacity, while the highest adsorption capacity was seen when the temperature was close to approximately 25°C.

Table 1. Operating factors and properties in experimental design

Factors	Operating ranges and values				
	- α (-1.682)	-1	0	+1	+ α (+1.682)
A: Contact time (min)	6.36	20	40	60	73.64
B: Concentration (mg l ⁻¹)	6.59	10	15	20	23.41
C: Temperature (°C)	19.88	25	32.5	40	45.11

Table 2. Experimental design and CCD approach results for the adsorption of toluene by the magnetic Fe₃O₄/AC

Run	A	B	C	Actual	Predicted
	Contact time (min)	Concentration (mg l ⁻¹)	Temperature (°C)	Adsorption capacity (mg g ⁻¹)	Adsorption capacity (mg g ⁻¹)
1	60	20	25	313	310
2	20	20	40	174	177
3	40	15	45.11	191	185
4	60	10	25	252	247
5	20	10	40	71	68
6	40	15	32.5	264	260
7	60	10	40	238	232
8	20	10	25	132	130
9	6.36	15	32.5	86	82
10	40	15	32.5	262	255
11	40	15	32.5	263	269
12	20	20	25	212	209
13	40	6.59	32.5	134	129
14	40	15	19.88	295	290
15	73.64	15	32.5	276	271
16	40	23.41	32.5	266	260
17	60	20	40	239	245

Process conditions were optimized to define the maximum adsorption capacity value for toluene. In the optimization process, the values such as the contact time, initial toluene concentration, and temperature were analyzed in the operating range. Optimum adsorption conditions were defined applying the desirability program for maximum adsorption capacity of toluene

by the magnetic Fe₃O₄/AC, and the optimum results obtained are presented in Figure 6. The maximum adsorption capacity of the magnetic Fe₃O₄/AC for the toluene adsorption was determined as 312.99 mg g⁻¹ under optimal process conditions such as 59.48 min contact time, 17.21 mg l⁻¹ initial toluene concentration, and 26.01°C temperature.

Table 3. ANOVA for the quadratic model surface

Source	F-value	p-value	
Model	49.96	< 0.0001	significant
A-Contact time	235.33	< 0.0001	
B-Concentration	85.99	< 0.0001	
C-Temperature	51.64	0.0002	
AB	9.86	0.0164	
AC	0.0814	0.7836	
BC	0.9215	0.3691	
A ²	51.64	0.0002	
B ²	30.59	0.0009	
C ²	3.19	0.1174	

R² = 0.9847, Adeq precision = 22.44

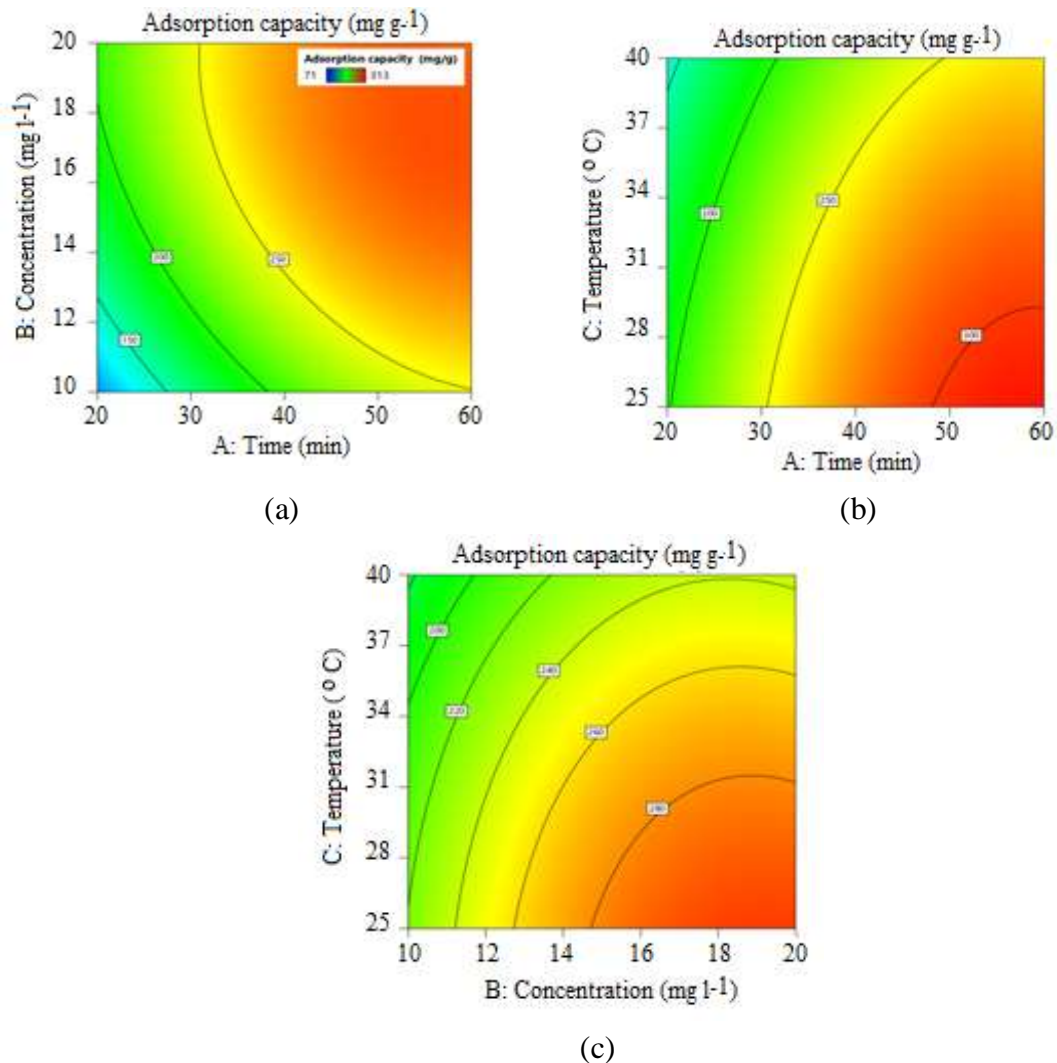


Figure 5. Interactive effects of contact time and initial toluene concentration (a), contact time and temperature (b), initial toluene concentration and temperature (c) on the adsorption capacity of toluene by the magnetic Fe₃O₄/AC.

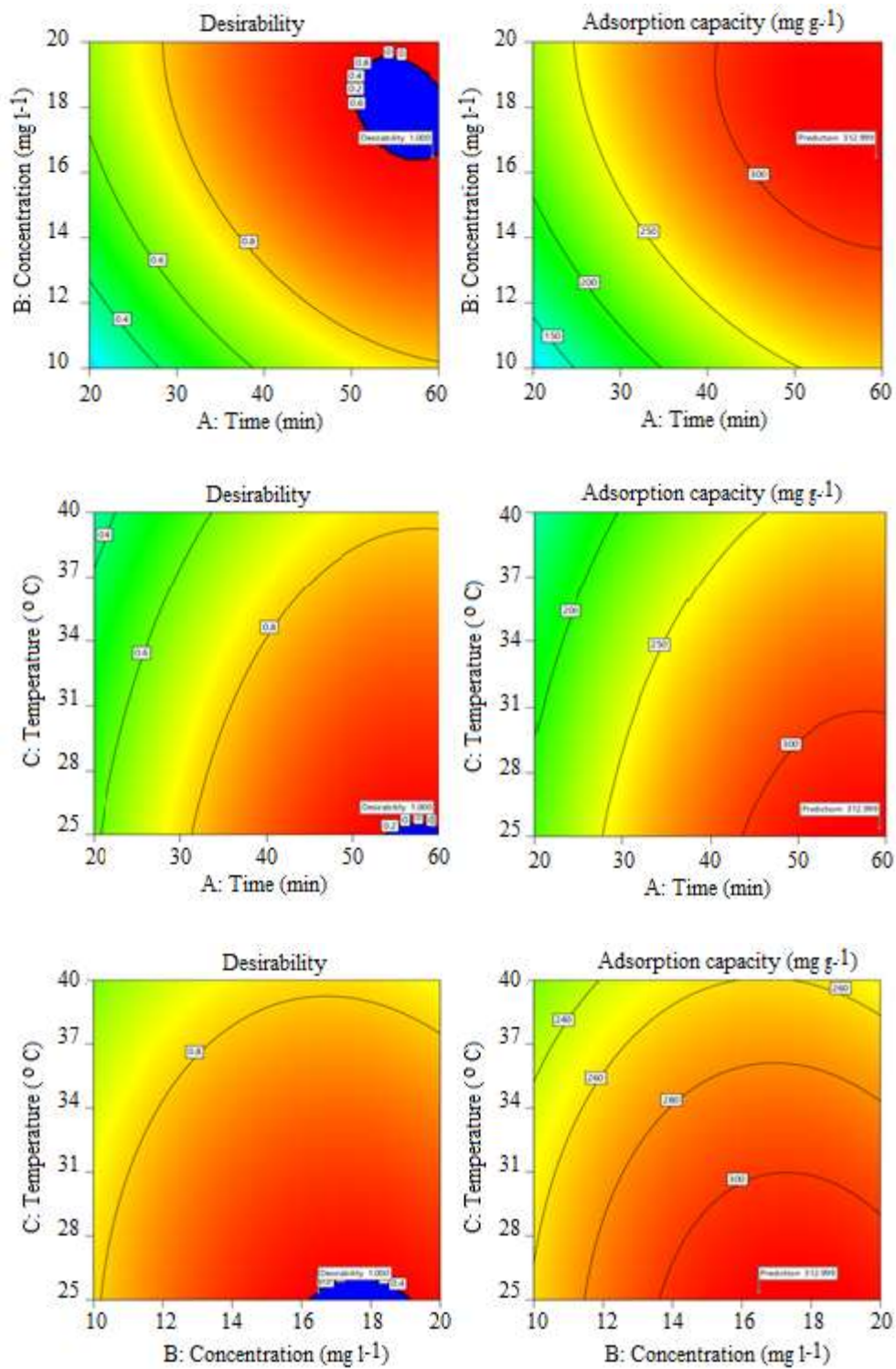


Figure 6. Optimum adsorption conditions of toluene by the magnetic Fe₃O₄/AC.

3.3. Adsorption kinetics

Under the conditions defined by RSM optimization, pseudo-first-order (PFO) and pseudo-second-order (PSO) kinetic models were used to determine the process mechanism and potential speed control steps in the adsorption of toluene by the magnetic Fe₃O₄/AC. PFO model defines the adsorption rate proportional to the number of empty sites.¹⁸ The non-linear form of the PFO kinetic model is presented with Eq. (2):

$$q_t = q_e(1 - e^{-k_1 t}) \quad (2)$$

Where, q_e and q_t (mg g⁻¹) indicate the amounts of adsorbent adsorbed at equilibrium and any t time (min), respectively. k_1 (1/min) represents the rate constant of the PFO model. This equation is valid for gas/solid adsorption depending on the adsorbent's capacity. It assumes that the change rate in adsorbate absorption over time is proportional to the difference in time and the saturation concentration and adsorbent amount.

The PSO equation, based on the capacity of the adsorption equilibrium, suggests that the fill rate of the adsorption areas is proportional to the square of the number of empty areas. The rate of adsorption is related to the concentration of active sites on the surface of the adsorbent.¹⁸ The non-linear form of the PSO kinetic model is given with Eq. (3) below:

$$q_t = \frac{k_2 q_e^2 t}{1 + k_2 q_e t} \quad (3)$$

Where, q_e (mg g⁻¹) is the adsorption capacity at equilibrium, k_2 (g mg⁻¹ min⁻¹) is the rate constant of the PSO model. It was determined that the PSO model better defined the adsorption kinetic data for toluene (Figure 7 and Table 4).

Table 4. Adsorption kinetic parameters of toluene by the magnetic Fe₃O₄/AC.

Kinetic models	Parameters	Values
PFO	q_e (mg g ⁻¹)	317.287
	k_1 (1/min)	0.0584
	R ²	0.985
PSO	q_e (mg g ⁻¹)	331.675
	k_2 (g mg ⁻¹ min ⁻¹)	0.0006
	R ²	0.992

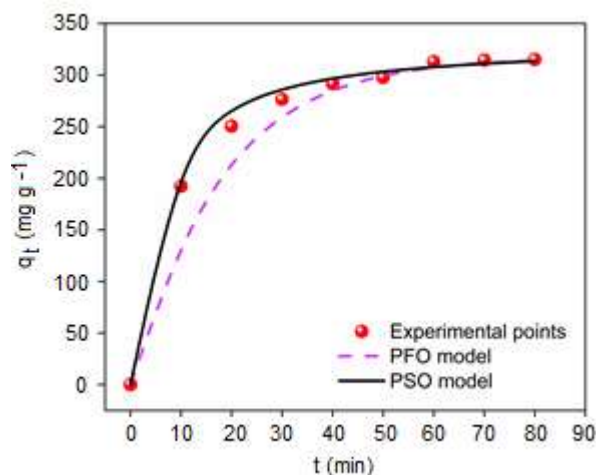


Figure 7. Adsorption kinetics of toluene by the magnetic Fe₃O₄/AC.

3.4. Adsorption isotherms

Under the conditions determined by RSM optimization, Langmuir, Freundlich, and Dubinin-Radushkevich (D-R) models were used to evaluate the equilibrium isotherms for the adsorption of toluene by the magnetic Fe₃O₄/AC.

The Langmuir adsorption isotherm applies to single-layer surface adsorption, including a limited number of identical regions. This model assumes that the adsorption energies on the surface are the same and that there is no adsorbate migration from the surface. Based on these assumptions, the Langmuir model is formulated in the following equation.¹⁹

$$q_e = \frac{q_{max} K_L C_e}{1 + K_L C_e} \quad (4)$$

Where, C_e (mg l⁻¹) is the equilibrium concentration of the adsorbate, q_e (mg g⁻¹) is the adsorption capacity at equilibrium, q_{max} (mg g⁻¹) is the maximum monolayer adsorption capacity. K_L (l mg⁻¹) is Langmuir isotherm constant.

The main characteristic of the Langmuir isotherm is that the equilibrium parameter, which is a dimensionless constant called the separation factor or equilibrium parameter, can be expressed as R_L :¹⁹

$$R_L = \frac{1}{1 + K_L C_{in}} \quad (5)$$

In this equation, C_{in} (mg l⁻¹) is the initial concentration.

K_L is the constant related to adsorption energy. R_L value indicates the inconvenience of adsorption nature if R_L is > 1 . If $R_L = 1$, it is linear. If $0 < R_L < 1$, it is suitable.¹⁹ The Freundlich adsorption isotherm is often used to describe the adsorption properties of a heterogeneous surface. This isotherm is formulated with the empirical equation proposed by Freundlich:¹⁹

$$q_e = K_F C_e^{1/n} \quad (6)$$

In this equation, K_F [(mg g⁻¹) (l mg⁻¹)^{1/n}] is the Freundlich isotherm constant. n is the adsorption density. C_e (mg l⁻¹) is the equilibrium concentration of adsorbate. q_e (mg g⁻¹) is the adsorption capacity at equilibrium. $1/n$ is a function of adsorption power in the adsorption process. The smaller $1/n$, the higher expected heterogeneity. This expression is reduced to the linear adsorption isotherm in the situation where $1/n$ is 1. If n is between 1 and 10, this situation indicates a suitable adsorption process.¹⁹

The D-R isotherm model was developed to describe the effect of the porous structure of adsorbent. It is based on the theory of the adsorption potential and suggests that in contrast to the layered adsorption on pore walls, the adsorption process is associated with the filling of the microporous volume. It is argued that the model of the D-R isotherm is superior to the Langmuir isotherm because the Langmuir isotherm takes into account a homogeneous surface or a constant adsorption potential. The non-linear form of this model is described by Eq. (7).

$$q_e = q_s \exp(-\beta \varepsilon^2) \quad (7)$$

In this equation, q_e (mg g⁻¹) is the adsorption capacity at equilibrium. q_s (mg g⁻¹) is theoretical isotherm saturation capacity. β (mol² (kJ)⁻¹) is the adsorption energy, and ε (J mol⁻¹) is the adsorption potential. The adsorption potential is described by Eq. (8).²⁰

$$\varepsilon = RT \ln \left(1 + \frac{1}{C_e} \right) \quad (8)$$

In this equation, R (8.314 J mol⁻¹ K⁻¹), T (K), and C_e (mg l⁻¹) represent gas constant, absolute temperature, and adsorbate equilibrium concentration, respectively. Adsorption energy is expressed by Eq. (9).

$$E = \frac{1}{\sqrt{2\beta}} \quad (9)$$

Numerical value of E provides about the adsorption mechanism. If $E < 8$ kJ mol⁻¹, physical adsorption is

dominant. However, in the situation indicating 8 kJ mol⁻¹ $< E < 16$ kJ mol⁻¹ and $E > 16$ kJ mol⁻¹, adsorption occurs by ion exchange and diffusion, respectively.²¹

According to the isotherm data calculated in Table 5, R_L was 0.362, indicating that the Langmuir isotherm model was suitable. In this study, the maximum monolayer adsorption capacity (q_{max}) obtained from the Langmuir isotherm model was 385.208 mg g⁻¹, K_L (Langmuir Constant) was 0.200 l mg⁻¹. The value of R^2 was 0.999, indicating that experimental data was better defined by Langmuir isotherm model in the adsorption of toluene by the magnetic Fe₃O₄/AC. The E value in this study was determined to be 0.446 kJ mol⁻¹, indicating that the adsorption was a physical process (Figure 8 and Table 5).

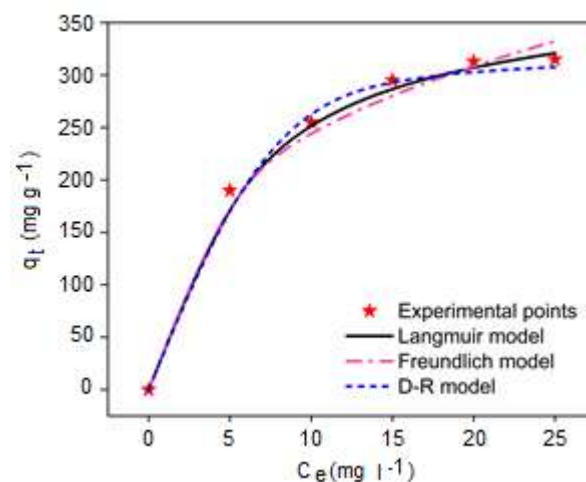


Figure 8. Adsorption isotherms of toluene by the magnetic Fe₃O₄/AC.

Table 5. Adsorption isotherm parameters of toluene by the magnetic Fe₃O₄/AC.

Isotherm models	Parameters	Values
Langmuir	q_{max} (mg g ⁻¹)	385.208
	K_L (l mg ⁻¹)	0.200
	R_L	0.362
	R^2	0.999
Freundlich	K_F [(mg g ⁻¹) (l mg ⁻¹) ^{1/n}]	116.396
	n	3.067
	R^2	0.996
	q_s (mg g ⁻¹)	315.135
D-R	β (mol ² (kJ) ⁻¹)	2.507*10 ⁻⁶
	E (kJ mol ⁻¹)	0.446
	R^2	0.997

4. CONCLUSIONS

In this study, we presented the first application of magnetic Fe₃O₄ functionalized with AC as nano-adsorbent for the removal of gas-phase toluene by adsorption process. Firstly, the magnetic Fe₃O₄/AC was synthesized via co-precipitation method within the framework of nanotechnology principles. Then, the effects of process conditions such as contact time, initial toluene concentration, and temperature on the adsorption of toluene by the magnetic Fe₃O₄/AC were investigated using the RSM. The obtained magnetic Fe₃O₄/AC was characterized using SEM, FTIR, and TG analysis. The maximum adsorption capacity for the toluene by the magnetic Fe₃O₄/AC was determined as 312.99 mg g⁻¹ under optimal process conditions such as 59.48 min contact time, 17.21 mg l⁻¹ initial toluene concentration, and 26.01°C temperature. The adsorption was in the best fit with the Langmuir isotherm model. The adsorption followed by the PSO kinetic model. This study indicated that magnetic Fe₃O₄/AC could be applied as a promising adsorbent for the removal of gas-phase toluene.

ACKNOWLEDGEMENTS

The authors are grateful to the Mardin Artuklu University Research Fund (MAUBAP, Project No. MAÜ.BAP.18.SHMYO.030) for their financial support.

Conflict of interests

Authors declare that there is no a conflict of interest with any person, institute, company, etc.

REFERENCES

- Kumar, M.; Giri, B. S.; Kim, K.-H.; Singh, R. P.; Rene, E. R.; López, M. E.; Rai, B. N.; Singh, H.; Prasad, D.; Singh, R. S. *Bioresour. Technol.* **2019**, 285, 121317.
- Kutluay, S.; Baytar, O.; Şahin, Ö. *Res. Eng. Struct. Mater.* **2019**, 5 (3), 279-298.
- Ryu, H. W.; Song, M. Y.; Park, J. S.; Kim, J. M.; Jung, S. C.; Song, J.; Kim, B. J.; Park, Y. K. *Environ. Res.* **2019**, 172, 649-657.
- Xu, P.; Wei, Y.; Cheng, N.; Li, S.; Li, W.; Guo, T.; Wang, X. *J. Hazard. Mater.* **2019**, 366, 105-113.
- Temel, F.; Kutluay, S. *New J. Chem.* **2020**, 44 (30), 12949-12961.
- Temel, F.; Tabakci, M. *Talanta* **2016**, 153, 221-227.
- Şahin, Ö.; Saka, C.; Kutluay, S. *J. Ind. Eng. Chem.* **2013**, 19 (5), 1617-1623.
- Saka, C.; Şahin, Ö.; Kutluay, S. *Energ. Source. Part A* **2016**, 38 (3), 339-346.
- Tor, A.; Aydın, M. E.; Aydın, S.; Tabakci, M.; Beduk, F. *J. Hazard. Mater.* **2013**, 262, 656-663.
- Connie, Z. Y.; Ariya, P. A. *Int. J. Environ. Sci.* **2015**, 31, 164-174.
- Bhatia, D.; Datta, D.; Joshi, A.; Gupta, S.; Gote, Y. *J. Chem. Eng.* **2018**, 63 (2), 436-445.
- Kutluay, S.; Baytar, O.; Şahin, Ö. *J. Environ. Chem. Eng.* **2019**, 7 (2), 102947.
- Zhao, Z.; Wang, S.; Yang, Y.; Li, X.; Li, J.; Li, Z. *Chem. Eng. J.* **2015**, 259, 79-89.
- Juang, R. S.; Yei, Y. C.; Liao, C. S.; Lin, K. S.; Lu, H. C.; Wang, S. F.; Sun, A. C. *J. Taiwan. Inst. Chem. Eng.* **2018**, 90, 51-60.
- Kutluay, S.; Baytar, O.; Şahin, Ö.; Arran, A. *Eur. J. Tech.* **2020**, 10 (1), 131-142.
- Baytar, O.; Şahin, Ö.; Horoz, S.; Kutluay, S. *Environ. Sci. Pollut. Res.* **2020**, 27, 26191-26210.
- Vohra, M. S. *Arab. J. Sci. Eng.* **2015**, 40 (11), 3007-3017.
- Ali, R. M.; Hamad, H. A.; Hussein, M. M.; Malash, G. F. *Ecol. Eng.* **2016**, 91, 317-332.
- Dada, A.; Olalekan, A.; Olatunya, A.; Dada, O. *IOSR J. Appl. Chem.* **2012**, 3 (1), 38-45.
- Hu, Q.; Zhang, Z. *J. Mol. Liq.* **2019**, 277, 646-648.
- Sadeghalvad, B.; Azadmehr, A.; Hezarkhani, A. *RSC Adv.* **2016**, 6 (72), 67630-67642.



Calculation of the infrared spectrum of 4-Cyanostyrene by Hartree-Fock (HF) and Density Functional Theory (DFT)

Kani ARICI^{1,*}, Rafet Yılmaz²

¹Department of Physics, Faculty of Science and Arts, Kilis 7 Aralık University, Kilis, Turkey

²Department of Physics, Faculty of Science and Arts, Yüzüncü Yıl University, Van Turkey

Received: 23 June 2020; Revised: 08 September 2020; Accepted: 09 September 2020

*Corresponding author e-mail: arici@kilis.edu.tr

Citation: Arıcı, K.; Yılmaz, R. *Int. J. Chem. Technol.* 2020, 4 (2), 156-161.

ABSTRACT

In this study, the molecular geometry of 4-Cyanostyrene molecule was optimized by using the Hartree-Fock (HF) and density functional theory (DFT/B3LYP) with 6-311G(d,p) basis set in the ground state. After the optimization, infrared vibration bands of 4-Cyanostyrene molecule were calculated by using the Hartree-Fock (HF) and density functional theory (DFT/B3LYP) with 6-311G(d,p) basis set. The theoretically calculated vibrational frequencies were multiplied by a scalar factor to correlate to experimental results. These theoretically obtained frequencies were compared exactly with the experimental results of 4-Cyanostyrene. All calculated frequencies were discussed. Finally, the correlation graphs of the theoretical and experimental results were obtained. The results were seen to be quite compatible with each other.

Keywords: 4-Cyanostyrene, Hartree-Fock (HF), density functional theory (DFT), infrared (IR).

4- Siyanostirenin infrared spektrumunun Hartree-Fock (HF) ve yoğunluk fonksiyon teorisiyle (DFT) hesaplanması

ÖZ

Bu çalışmada, 4-Siyanostiren molekülünün temel halde moleküler geometrisi, Hartree-Fock (HF) ve 6-311G (d, p) temel sete sahip yoğunluk fonksiyonel teorisi (DFT/B3LYP) kullanılarak optimize edildi. Optimizasyondan sonra 4-Siyanostiren molekülünün infrared titreşim bantları, Hartree-Fock (HF) ve 6-311G (d, p) temel sete sahip yoğunluk fonksiyonel teorisi (DFT/B3LYP) kullanılarak hesaplandı. Teorik olarak hesaplanan titreşim frekansları, deneysel sonuçlarla ilişkilendirmek için bir skale faktör ile çarpıldı. Teorik olarak elde edilen bu frekanslar, 4-Siyanostirenin deneysel sonuçlarıyla tam olarak birebir karşılaştırıldı. Hesaplanan tüm frekanslar tartışıldı. Son olarak teorik ve deneysel sonuçların korelasyon grafikleri elde edildi. Sonuçların birbiriyle oldukça uyumlu olduğu görüldü.

Anahtar Kelimeler: 4-siyanostiren, Hartree-Fock (HF), yoğunluk fonksiyon teorisi (DFT), kızılötesi (IR).

1. INTRODUCTION

Styrene is most commonly found in cigarette smoke, polluted atmosphere and working areas. Styrene and styrene-7,8-oxide are used in plastic reinforcement and rubber industry. Styrene-7,8-oxide molecule is the basic metabolite of styrene in the human body.¹ Many researchers have revealed that styrene and styrene-7,8-oxide substances cause various cancers, and increase risk of cancer in groups working in the plastics industry.²⁻¹⁰ Styrene model is studied on the rotation of a vinyl group attached to the benzene ring. Thus, many scientists have worked on this topic. Hollas and co-

workers have accepted the structure of styrene as planar and determined its vibrations with the help of the electronic absorption spectrum.¹¹ Zilberg and Haas have studied the fluorescence spectra of the styrene, and also they have investigated trans- β -methyl styrene substances in both the ground state and twice-excited state, finally carried out the theoretical ab initio study.¹² The rotational constant of the vinyl group in the planar structure of the styrene has been calculated by Bock and co-workers based on ab initio calculations.¹³ In the literature, although there are many experimental and theoretical studies about styrene and trans- β -methyl

styrene, it is seen that 4-Cyanostyrene, a derivative of styrene, has not been studied both experimentally and theoretically. Therefore, in this study, it is aimed to calculate the infrared vibration frequencies of the planar 4-Cyanostyrene molecule using HF and DFT methods.

2. CALCULATIONS

Infrared vibration calculations were carried out using the Gaussian 09 software on a windows system.¹⁴ As mentioned above, the shape of the molecule was considered as plane, and the input data was created by using Gauss View molecular visualization program.¹⁵ The data created above was reused in HF/6-311G (d, p) and DFT/B3LYP/6-311G (d, p) to find optimization, that is, the lowest energy level of the molecule. In this case, bond lengths, bond angles and dihedral angles in the molecule were calculated. Thus, by optimizing the molecule, negative vibrations were prevented. All the vibration frequencies in the basic state of the molecule were obtained using the same HF/6-311G (d, p) and DFT/6-311G (d, p) calculation methods. The theoretically calculated number of vibrations is considerably greater than that observed experimentally. This means that the compound is large and the calculations are done in gas phase. Since the 4-Cyanostyrene molecule is planar and has a C_s symmetry, all vibrations are both raman and infrared active. Considering the method mentioned above, a total of 45 vibrations were calculated as 31 in-plane (A') and 14 out-of-plane (A''). The frequencies obtained were multiplied by scalar factors of 0.9085 and 0.9669, respectively. All the frequencies are assigned in terms of fundamental, overtone and combination bands. As shown in Figure 1, the 4-Cyanostyrene molecule has 17 atoms.

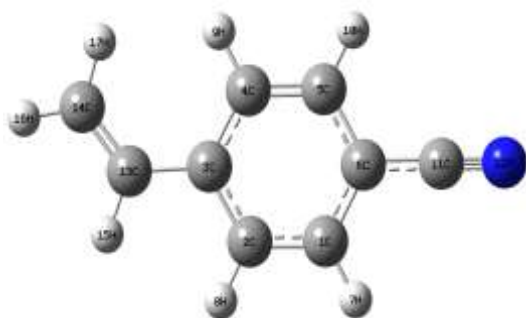


Figure 1. 4-Cyanostyrene molecule.

3. RESULTS AND DISCUSSION

3.1. Combination and overtone bands

The experimental infrared vibrational spectra of 4-Cyanostyrene molecule are shown in Figure 2.¹⁶

The infrared vibration frequencies obtained from the calculations and the experimental data are given in Table 1. As seen in Figure 2, the bands between 2100 cm^{-1} - 1700 cm^{-1} are the combinations of the benzene ring. For example, in Figure 2, the band at 1846 cm^{-1} is determined as the sum of the 536 cm^{-1} and 3100 cm^{-1} bands. The bands between 3100 cm^{-1} - 4000 cm^{-1} are the overtone bands. The band at 3392 cm^{-1} is designated as the overtone band, which is four times the 848 cm^{-1} band.

3.2. Vinyl group vibrations

Asymmetric and symmetric C-H stretch vibrations in the vinyl group appear between the regions 3090 cm^{-1} - 3075 cm^{-1} and 3050 cm^{-1} - 3000 cm^{-1} , respectively.¹⁷ The 3090 cm^{-1} band observed in the spectrum was marked as asymmetric C-H stretch and was calculated as 2991.3675 cm^{-1} in HF and 3120.3907 cm^{-1} in DFT. Symmetrical C-H stress vibration at the spectrum was observed at 3012 cm^{-1} and calculated as 2861.8122 cm^{-1} in HF and 342.5710 cm^{-1} in DFT. The C-H tensile vibration band in vinyl appears around 3000 cm^{-1} .¹⁸ Looking at the spectrum, this band was observed at 2994 cm^{-1} as medium and was calculated as 2839.0217 cm^{-1} in HF and 3033.3085 cm^{-1} in DFT. The calculation of HF deviated from the experimental value by approximately 150 cm^{-1} . In general, in the infrared spectrum, C = C tensile vibration bands of vinyl, vinylidene and cis alkenes are observed in the range of 1600 cm^{-1} to 1635 cm^{-1} .¹⁷ However, this C = C tensile vibration band was observed at 1627 cm^{-1} with medium intensity. This band was calculated as 1677.4357 cm^{-1} in HF and 1634.5753 cm^{-1} in DFT.

In-plane bending vibrations of the vinyl molecule appear between 1075 cm^{-1} and 1415 cm^{-1} .¹⁸ In the spectrum, the band observed at 1423 cm^{-1} with medium intensity was marked as symmetrical in-plane bending (scissoring) vibration of the CH_2 group in vinyl. In Figure 2, the band that appears to be rather weak at 1310 cm^{-1} was marked as the C-H in-plane bending vibration. The band observed at 1014 cm^{-1} with medium intensity was marked as rocking in the plane. It is understood from Table 1 that these three bands marked are in harmony with the calculated values.

The out-of-plane C-H bending vibrations in the vinyl group are generally observed in the range of 985 cm^{-1} to 915 cm^{-1} .¹⁷ A closer look at the spectrum revealed that the band at 991 cm^{-1} was very intense and marked as out-of-plane C-H bending vibration. Likewise, the band which was observed to be very strong at 922 cm^{-1} was marked as out-of-plane wagging. It is understood from Table 1 that these bands are in agreement with the theoretically calculated results. As a consequence, these values are compatible with many experimental and theoretical results.¹⁹⁻²⁶

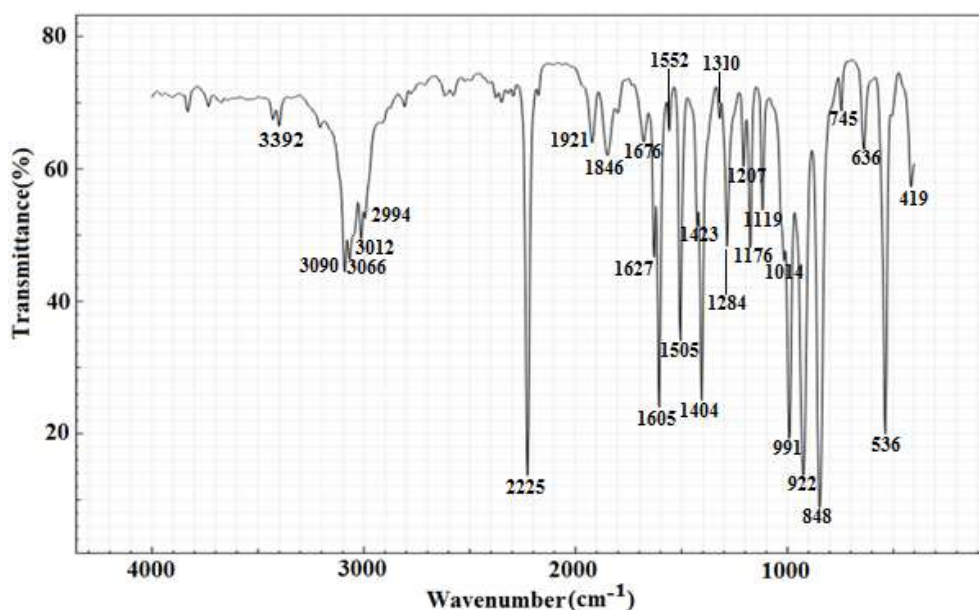


Figure 2. The experimental infrared vibrational spectra of 4-Cyanostyrene molecule.

3.3. C≡N vibrations

In the infrared spectrum, C≡N tensile vibration bands of benzonitriles between 2220 cm^{-1} and 2240 cm^{-1} are observed to be strong. This C≡N stretch band may slide higher or lower depending on the condition of the groups attached to the benzene ring.²⁷⁻²⁹ Looking at the infrared spectrum, it was observed as a very strong at 2225 cm^{-1} , and it was assigned as C≡N strain vibration. The peak observed at 536 cm^{-1} was marked as the C-N out-of-plane bending band. From Table 1, it seems that the experimental results and the theoretical results are highly compatible with each other.

3.4. Ring vibrations

3.4.1. C-H vibrations

The peaks observed between $3000\text{-}3100\text{ cm}^{-1}$ are aromatic C-H tensile vibrations³⁰ and they are pure. Looking at the spectrum, the peak that appear at 3066 cm^{-1} with medium intensity was marked as aromatic C-H stretch band. This peak was calculated at 2873.7293 cm^{-1} in HF and 3066.5823 cm^{-1} in DFT. In-plane and out-of-plane C-H bending vibrations are observed at $1000\text{-}1300\text{ cm}^{-1}$ and $950\text{-}800\text{ cm}^{-1}$, respectively.³¹⁻³³ Looking at the spectrum, the bands observed at 1284 cm^{-1} , 1207 cm^{-1} , 1176 cm^{-1} and 1119 cm^{-1} at medium intensity were marked as in-plane

bending. These bands were calculated as 1315.5468 cm^{-1} , 1216.6726 cm^{-1} , 1197.0028 cm^{-1} and 1078.4971 cm^{-1} in HF and 1284.7295 cm^{-1} , 1191.5421 cm^{-1} , 1189.9749 cm^{-1} and 1104.8523 cm^{-1} in DFT, respectively. However, as seen in Table 1, it can be said that the calculated HF values deviate slightly from the experimental values. The band that appears to be very strong at 848 cm^{-1} in the spectrum is marked as out-of-plane bending and is compatible with DFT calculation.

3.4.2. C-C vibrations

In the infrared spectrum, aromatic C-C stretch vibrations generally occur between 1620 cm^{-1} and 1400 cm^{-1} .¹⁷ Looking at the spectrum, the bands at 1627 cm^{-1} , 1605 cm^{-1} , 1552 cm^{-1} , 1504 cm^{-1} , 1423 cm^{-1} and 1404 cm^{-1} , which appear to be strong and very weak in this range, were marked as C-C ring strain vibrations. The bands observed very weak at 745 cm^{-1} and medium strength at 419 cm^{-1} were marked as out-of-plane C-C bending vibration. From Table 1 these signs seem to agree with the theoretical results.

Although the observed bands are compatible with the literature, there is some difference in calculation. This may be due to the calculation of the molecule in the gas phase. It is also known from the literature that the frequencies calculated by the HF method are higher than other methods.^{34,35}

Table 1. Frequencies obtained from the calculations and the experimental data along with their assignment

N	T	Calculation HF/6-311G(dp)			Calculation DFT/B3LYP/6-311G(dp)			Exp. ^c	Assignment
		Frequency	IR Int.	Scaled ^a	Frequency	IR Int.	Scaled ^b		
1	A''	67.1829	0.6598	61.0356	28.7136	0.3670	27.7631	-----	(C ₂ H ₃) torsion
2	A''	207.0090	1.3737	188.0676	103.7538	1.3654	100.3195	-----	Butterfly
3	A'	217.6998	4.3485	197.7802	141.2461	4.3033	136.5708	-----	β (C ₂ H ₃) + β (C≡N)
4	A''	337.7575	4.0868	306.8526	244.7321	4.3430	236.6314	-----	Fluctation
5	A'	354.4086	2.2227	321.9802	245.4644	1.2741	237.3395	-----	β (C ₂ H ₃)
6	A'	418.7019	0.5483	380.3906	384.9904	0.3762	372.2472	-----	v molecule
7	A''	472.9675	0.0651	429.6909	408.4511	0.2545	394.9313	-----	γ (CCH)
8	A''	524.9858	1.4553	476.9495	426.7356	4.0108	412.6106	419 m	γ (CCH)
9	A'	581.2008	4.7494	528.0209	511.2766	2.9985	494.3533	-----	β (CH ₂)
10	A''	653.8436	15.9323	594.0169	559.0377	18.8979	540.5335	536 s	γ (CCN) at Cy.
11	A'	655.5855	0.5163	595.5994	574.3667	0.2203	555.3551	-----	β (CCN) at Cy.
12	A''	721.9496	0.3528	655.8912	655.1946	3.3536	633.5076	-----	γ (CCH)
13	A'	751.8163	0.1759	683.0251	662.7756	0.1241	640.8377	-----	Ring Deformation
14	A'	752.0514	2.3801	683.2386	685.7267	0.0990	663.0291	-----	Molecule Deformation
15	A''	861.3360	1.0637	782.5237	770.4318	0.0814	744.9305	745 vw	γ (CCH)
16	A'	891.5065	1.7953	809.9336	826.4174	0.3285	799.0629	-----	Ring Deformation
17	A''	1023.1287	57.4272	929.5124	846.6817	0.8861	818.6565	-----	γ (CH) at ring
18	A''	1031.7333	0.1472	937.3297	867.8710	48.0671	839.1444	848 vs	γ (CH) at ring
19	A''	1114.0998	0.3477	1012.1596	945.3533	42.3555	914.0621	922 vs	CH ₂ Wagging
20	A''	1127.8882	46.5517	1024.6864	977.8831	0.4127	945.5151	-----	γ (CH) at ring
21	A''	1151.3583	3.6369	1046.0090	982.7572	0.0812	950.2279	-----	γ (CH) at ring
22	A''	1151.8021	1.2139	1046.4122	1028.8205	16.1885	994.7665	991 vs	γ (CH) at V.
23	A'	1166.6827	0.3499	1059.9312	1033.1801	2.5824	998.9818	-----	Ring breathing
24	A'	1181.7350	21.5229	1073.6062	1049.6640	4.9647	1014.9201	1014 m	CH ₂ Rocking
25	A'	1187.1185	3.4969	1078.4971	1142.6749	3.6784	1104.8523	1119 m	β (CH) at ring
26	A'	1283.8421	5.2075	1166.3705	1199.4351	3.2776	1159.7337	-----	v C-(C≡N)
27	A'	1317.5596	5.5843	1197.0028	1230.7115	1.1041	1189.9749	1176 m	β (CH) at ring
28	A'	1339.2104	4.7716	1216.6726	1232.3323	0.3595	1191.5421	1207 w	β (CH) at ring
29	A'	1359.1966	2.7419	1234.8301	1315.2104	5.7635	1271.6769	-----	β (CH) at V.
30	A'	1448.0428	2.9391	1315.5468	1328.7098	0.2190	1284.7295	1284 m	β (CH) at ring
31	A'	1484.8981	0.0234	1349.0299	1355.5765	0.8538	1310.7069	1310vw	β (CH) at V.
32	A'	1566.5226	16.8539	1423.1857	1438.4795	11.8529	1390.8658	1404 s	v(CC) at ring
33	A'	1612.0305	4.5415	1464.5297	1462.0319	2.9805	1413.6386	1423 m	(CH ₂) Sc. + v(CC) at ring
34	A'	1693.7875	25.2312	1538.8059	1540.0096	14.3853	1489.0352	1504 s	v(CC) at ring
35	A'	1739.4688	3.4180	1580.3074	1589.3371	1.1049	1536.7300	1552vw	v(CC) at ring
36	A'	1801.0285	42.9698	1636.2343	1649.0936	18.7440	1594.5086	1605 s	v(CC) at ring
37	A'	1846.3795	3.6552	1677.4357	1690.5320	4.7590	1634.5753	1627 m	v(C=C) at V. + v(CC) at ring
38	A'	2446.3422	95.5720	2222.5018	2335.1359	46.0782	2257.8429	2225 vs	v(C≡N)
39	A'	3124.9551	4.6786	2839.0217	3137.1482	13.3434	3033.3085	2994 m	v(CH) at V.
40	A'	3150.0410	9.2565	2861.8122	3146.7277	3.2470	3042.5710	3012 m	S. v(CH) at V.
41	A'	3163.1583	17.6060	2873.7293	3171.5610	9.0007	3066.5823	3066 m	v(CH) at ring
42	A'	3183.5435	5.6943	2892.2492	3184.2780	3.7021	3078.8783	-----	v(CH) at ring
43	A'	3185.6607	7.1484	2894.1727	3197.9466	6.8913	3092.0945	-----	v(CH) at ring
44	A'	3204.7402	10.0409	2911.5064	3200.2597	1.9608	3094.3311	-----	v(CH) at ring
45	A'	3292.6445	14.5605	2991.3675	3227.2114	10.7017	3120.3907	3090 m	A. v(CH) at V.

Scaled^a: 0.9085, scaled^b: 0.9669, A.: asymmetric, A': in-plane, A'': out-of-plane, Sc.: scissoring, S.: symmetric, Cy.: cyano, V.: vinyl, v: in plane stretch, β: in plane bending, γ: out of plane bending, T: type, N: number, c: Ref.16.

Some vibration types of the 4-Cyanostyrene molecule are listed in Figure 3.

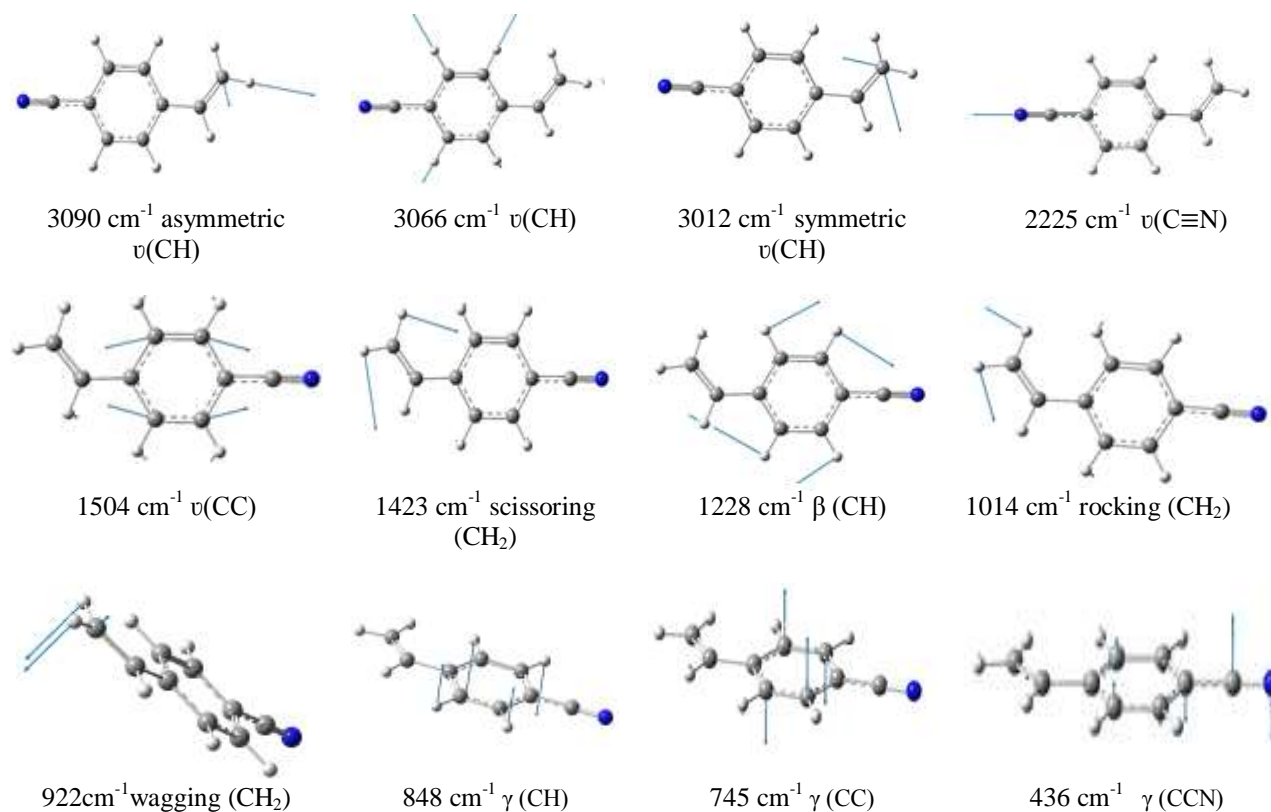


Figure 3. Vibration types of the 4-Cyanostyrene molecule.

4. CONCLUSIONS

The IR frequencies and intensities of the fundamental vibrational bands of 4-Cyanostyrene were calculated using HF and DFT/B3LYP methods with 6-311G(dp) basis set. The infrared absorption and intensities, computed by B3LYP method, are in reasonable agreement with the experimental data. The results confirm the ability of the methodology applied for interpretation of the vibrational spectrum of the 4-Cyanostyrene molecule in the solid state. It is important to do such a study first time on the 4-Cyanostyrene molecule.

ACKNOWLEDGEMENT

The Gaussian 09 program used in this study was provided by The Scientific Research Projects Council of Kilis 7 Aralık University, project number: 2010/02/08.

Conflict of interests

Authors declare that there is no a conflict of interest with any person, institute, company, etc.

REFERENCES

- Rappaport, S. M.; Yeowell-O'Connell, K.; Bodell, W.; Yager, J. W.; Symanski, E. *Cancer Res.* **1996**, 56 (23), 5410-5416.
- Kogevinas, M.; Ferro, G.; Andersen, A. et al. *Scand. J. Work Env. Hea.* **1994**, 20 (4), 251-261.
- Coggon, D.; Ntani, G.; Harris, E. C.; Palmer, K. T. *Occup. Environ. Med.* **2015**, 72 (3), 165-170.
- Christensen, M. S.; Vestergaard, J. M.; d'Amore, F. et al. *Epidemiology* **2018**, 29 (3), 342-351.
- Collins, J. J.; Bodner, K. M.; Bus, J. S. *Epidemiology* **2013**, 24 (2), 195-203.
- Nissen, M. S.; Stokholm, Z. A.; Christensen, M. S.; Schlunssen, V.; Vestergaard, J. M.; Iversen, I. B.; Kolstad, H. A. *Occup. Environ. Med.* **2018**, 75 (6), 412-414.
- Cruzan, G.; Bus, J. S.; Banton, M. I.; Sarang, S. S.; Waites, R.; Layko, D. B.; Raymond, J.; Dodd, D.;

- Andersen, M. E. *Toxicol. Sci.* **2017**, 159 (2), 413-421.
8. Cruzan, G.; Cushman, J. R.; Andrews, L.S.; et al. *J. Appl Toxicol.* **2001**, 21 (3), 185-198.
9. Ponomarev, V.; Tomatis, L. *Scand. J. Work Environ. Hea.* **1978**, 4 (2), 127-135.
10. Conti, B.; Maltoni, C.; Perino, G.; Ciliberti, A. *Ann. NY Acad. Sci.* **1988**, 534 (1), 203-234.
11. Hollas, J. M.; Khalilipour, E.; Thakur, S. N. *J. Mol. Spectrosc.* **1978**, 73 (2), 240-265.
12. Zilberg, S.; Haas, Y. *J. Chem. Phys.* **1995**, 103 (1), 20-36.
13. Bock, C. W.; Trachtman, M.; George, P. *Chem. Phys.* **1985**, 83 (3), 431-443.
14. Frisch, M. J.; Trucks, G. W. Schlegel, H. B. et al. GAUSSIAN 09: Revision C.02 (Pittsburg, PA: Gaussian Inc.) 2009.
15. Frisch, A.; Nielsen, A. B.; Holder, A. J. *Gauss 09 View User Manual (Pittsburg: Gaussian Inc.)* 2009.
16. https://www.acros.com/DesktopModules/Acros_Search_Results/Acros_Search_Results.aspx?search_type=CatalogSearch&SearchString=4-Cyanostyrene (accessed 01.05.2020).
17. Smith, B. C. *Infrared Spectral Interpretation: A Systematic Approach*; CRC Press, New York, 1998.
18. Rao, J. M. *Organic Spectroscopy Principles and Applications*, Narosa Publishing House, New Delhi, 2000.
19. Kanamori, H.; Endo, Y.; Hirota, E. *J. Chem. Phys.* **1990**, 92 (1), 197-205.
20. Kim, E.; Yamamoto, S. *J. Chem. Phys.* **2002**, 116 (24), 10713-10718.
21. Tanaka, K.; Toshimitsu, M.; Harada, K.; Tanaka, T. *J. Chem. Phys.* **2004**, 120 (8), 3604-3618.
22. Shepherd, R. A.; Doyle, T. J.; Graham, W. R. M. *J. Chem. Phys.* **1988**, 89 (5), 2738-2742.
23. Tanskanen, H.; Khriachtchev, L.; Rasanen, M.; Feldman, V. I.; Sukhov, F. F.; Orlov, A. Y.; Tyurin, D. A. *J. Chem. Phys.* **2005**, 123 (6), 064318.
24. Paolucci, D. M.; Gunkelman, K.; McMahon, M. T.; McHugh, J.; Abrash, S. A. *J. Phys. Chem.* **1995**, 99, 10506-10510.
25. Forney, D.; Jacox, M. E.; Thompson, W. E. *J. Mol. Spectrosc.* **1995**, 170, 178-214.
26. Nikow, M.; Wilhelm, M. J.; Dai, H. L. *J. Phys. Chem. A* **2009**, 113 (31), 8857-8870.
27. Dollish, F. R.; Fateley, W. G.; Bentley, F. F. *Characteristic Raman Frequencies of Organic Compounds*; Wiley: N.Y., USA, 1974.
28. Bellamy, L. J. *The Infrared Spectra of Complex Molecules*; Wiley: N.Y., USA, 1975.
29. Lin-Vien, D.; Colthup; N. B.; Fateley; W. G.; Grasselli; J. G. *The Handbook of Infrared and Raman Characteristics frequencies of Organic Molecules* Academic Press: San Diego, California, 1991.
30. Socrates, G. *Infrared and Raman Characteristic Group Frequencies*, 3rd ed.; Wiley: N.Y., USA, 2004.
31. Krishnakumar, V.; Prabavathi; N. *Spectrochim. Acta A* **2008**, 71 (12), 449-457.
32. Altun, A.; Gölcük, K.; Kumru, M. *J. Mol. Struct-Theochem* **2003**, 637, 155-169.
33. Singh, S. J.; Pandey, S. M. *Indian J. Pure Ap. Phy.* **1974**, 12, 300-304.
34. Lee, S. Y. B. *Korean Chem. Soc.* **1998**, 19 (1), 93-98.
35. Wheelless, C. J.; Zhou, X.; Liu; R. *J. Phys. Chem.* **1995**, 99 (33), 12488-12492.



Kinetic and analytical studies on pyrolysis of olive oil industry wastes

Gözde DUMAN TAC*

Department of Chemistry, Faculty of Science, Ege University, Izmir, Turkey

Received: 04 July 2020; Revised: 29 August 2020; Accepted: 09 September 2020

*Corresponding author e-mail: gozdeduman@gmail.com

Citation: Duman Tac, G. *Int. J. Chem. Technol.* 2020, 4 (2), 162-170.

ABSTRACT

The pyrolysis of olive pomace was carried out at two different heating rates at 500°C in the absence and presence of catalysts (commercial fluid catalytic cracking (FCC), aluminosilicate zeolite (ZSM-5) and red mud) using pyrolysis-gas chromatography/mass spectrometry (Py-GC/MS). The products obtained from biomass components in different temperature ranges by sequential pyrolysis of olive pomace were investigated. In addition, the apparent activation energy of olive pomace was calculated by thermogravimetric analysis method and determined as 105.6 kJ mole⁻¹ by Kissinger-Akahira-Sunose (KAS) method and 110.2 kJ mole⁻¹ by Flynn-Wall-Ozawa (FWO) method. According to Py-GC/MS results, the main components in bio-oil consists of phenolic compounds. In sequential pyrolysis, while the highest organic acid was obtained at low temperatures, phenolic compounds were formed at high temperatures. While bio-oil obtained by fast pyrolysis has higher organic acid content than that of bio-oil obtained by slow pyrolysis, slow pyrolysis bio-oil contains more furan and aliphatic ketone, aldehyde and ester. Catalytic studies revealed that catalysts were more effective in the slow pyrolysis process, which allows prolonged catalyst-pyrolysis vapor contact.

Keywords: Pyrolysis, TGA, Py-GC/MS, olive pomace waste, catalyst.

Zeytinyağı endüstrisi atıklarının pirolizi üzerine kinetik ve analitik çalışma

ÖZ

Piroliz gaz kromatografisi/kütle spektrometresi (Py-GC/MS) kullanılarak, pirinanın iki farklı ısıtma hızında 500°C'de katalizör yokluğunda ve varlığında (ticari akışkan katalitik çatlama (FCC), alimünosilikat zeolit (ZSM-5) ve kırmızı çamur) pirolizi gerçekleştirildi. Pirinanın basamaklı pirolizi ile farklı sıcaklık aralıklarındaki biyokütle bileşenlerinden elde edilen ürünler incelendi. Ayrıca pirinanın gözlenen aktivasyon enerjisi termogravimetrik analiz yöntemiyle hesaplandı ve Kissinger-Akahira-Sunose (KAS) metoduna göre 105.6 kJ mole⁻¹, Flynn-Wall-Ozawa (FWO) metoduna göre ise 110.2 kJ mole⁻¹ olarak belirlendi. Py-GC/MS sonuçlarına göre biyoyağın içindeki başlıca bileşenler fenolik bileşiklerden oluşmaktadır. Basamaklı pirolizde, en yüksek organik asit içeriği düşük sıcaklıklarda elde edilirken fenolik bileşikler yüksek sıcaklıklarda oluşmuştur. Hızlı piroliz ile elde edilen biyo-yağ, yavaş piroliz ile elde edilen biyo-yağdan daha yüksek organik asit içeriğine sahipken, yavaş piroliz biyo-yağı daha fazla furan ve alifatik keton, aldehit ve ester içermektedir. Katalitik çalışmalar, katalizörlerin, uzun süreli katalizör-piroliz buhar temasına izin veren yavaş piroliz işleminde daha etkili olduğunu ortaya koymuştur.

Anahtar Kelimeler: Piroliz, TGA, Py-GC/MS, pirina atığı, katalizör.

1. INTRODUCTION

Due to the depletion of fossil fuels and their environmental impact, renewables resources have been sought in recent years. Biomass materials are an abundant resource that is widely spread all around the world as well as the only carbon source among the other renewable resources. Although biomass materials are generally used as solid fuel in traditional methods, different conversion technologies have been developed to use biomass more efficiently and environmentally.¹

Among them, pyrolysis is one of the well-known thermochemical methods for converting biomass into value-added products in absence of oxygen. The yield and quality of the resultant products strongly depend on the conditions of pyrolysis as well as biomass type. Biomass consists of three major components, namely cellulose hemicellulose and lignin, and also relatively small amount of ash and extractives. Each component of biomass has different degradation routes during pyrolysis, giving different products. Basically, a high amount of solid product, so-called "biochar", can be

produced at low temperature pyrolysis and heating rates, while fast heating rate and high temperatures prefer the High yield of liquid products (bio-oil). Bio-oil is a mixture of more than hundred oxygenated organic compounds and has low quality in terms of fuel properties such as poor stability, low pH, high water content and viscosity etc. In order to improve its quality, bio-oil can be upgraded via heterogeneous catalysis. The main purpose of the upgrade is to obtain bio-oil with high energy content and stability by lowering the oxygen content of the bio-oil. Upgrading process can be applied in two ways, in-situ and ex-situ. These two processes distinguish between each other based on placement of the catalyst, as into the pyrolysis reactor or as separate reactor. There have been several studies on ex situ and in situ upgrading of bio-oil in presence of heterogeneous catalysts such as zeolites, metal oxides, etc.²

Besides these parameters, pyrolysis design is also effective on the characteristic of bio-oil. Bio-oil obtained from lab-scale pyrolysis systems probably depends on the pyrolysis unit, recovery and characterization methods. Therefore, a reliable data comparison, which is independent from reactor design, is required to investigate the effect of various conditions such as heating rate, temperature, the presence of catalyst, etc. on bio-oil composition. For this purpose, pyrolysis coupled with gas chromatographic separation and mass spectrometry detection is being used to provide preliminary chemical information on potential compounds derived from bio-oil.³ This system is called pyrolysis-gas chromatography/mass spectrometry (Py-GC/MS). Py-GC/MS offers repeatable and rapid chromatographic separation with using small quantities of sample. Several works have been performed to investigate the pyrolysis parameters such as temperature,⁴ heating rate,⁵ biomass type,^{6,7} particle size,⁸ catalyst⁹⁻¹³, and catalyst contact type¹⁴ on bio-oil composition.

Thermogravimetric analysis is another technique for investigating the pyrolysis behavior of biomass by determining kinetic parameters that provide useful information for pyrolysis parameter optimization and reactor design. Kinetic studies can be performed by two methods, isothermal and non-isothermal model. Non-isothermal method is widely used due to elimination of systematic errors arisen from unfitting assumptions of the reaction mechanism.¹⁵ On the other hand, biomass pyrolysis involves very complex and competitive reactions that cannot be expressed by simple mechanism pathways. At this point, the model-independent approach, that is, the iso-transform method, gives more reliable results in determining the kinetic parameters.¹⁶ Basically, iso-conversional method is calculated as a function of the extent of conversion at different heating rates. Kissinger-Akahira-Sunose

(KAS) and Ozawa-Flynn-Wall (OFW) are the examples of iso-conversional models based on integral approach for TGA data processing.

Mediterranean countries have an important potential in the olive oil sector by producing 97% of the world's olive oil production.¹⁷ Over the past five years, olive oil production in Turkey has increased by 20% and reached the second highest level in 2019 production with annual production of approximately 200,000 tons.¹⁸ A large amount of olive pomace are produced from olive oil extraction by the olive oil sector. Depending on the manufacturing process, olive pomace contains 45-70% of moisture. Olive pomace is usually treated with organic solvents to extract the residual oil, which is called pomace oil.

In this study, pyrolysis of olive pomace after solvent extraction was conducted under various conditions by using Py-GC/MS. Thermal degradation of olive pomace was analyzed using thermogravimetric method in order to determine apparent activation energy. Thermal and catalytic pyrolysis experiments were performed at slow (25°C/min) and fast (1200°C/min) heating rates in order to investigate the effect of catalysts on bio-oil composition. Sequential pyrolysis was also carried out to determine the change in chemical compounds in bio-oil as a function of biomass components.

2. MATERIALS AND METHODS

2.1. Material

Olive pomace, a byproduct of olive oil company, was supplied from olive pomace oil company in Izmir city, Turkey. Olive pomace was dried at 105°C overnight, it was grinded to a particle size less than 250 μ m and stored in sealed glass bottles until its use. Ultimate analysis was carried out using LECO CHNS 932 elemental analyzer according to ASTM D5291-96. The proximate analysis was done according to NREL/TP-510-42622 and ASTM D3175-89a for ash and volatile matter, respectively. The procedure reported by Li and co-workers¹⁹ was followed to determine the components of olive pomace. Proximate, ultimate and component analyses were performed in duplicate to ensure reproducibility of the characterization results. Relative deviation of the analyses was found to be less than 5%. The properties of olive pomace are given in Table 1.

Three different catalysts were tested in catalytic pyrolysis run. ZSM-5 is sodium aluminosilicate zeolite, which is commercially available (Zeolyst International). Fluid catalytic cracking (FCC) is commonly used in petroleum refineries for conversion of crude oils into more valuable products such as gasoline, olefinic gases, etc. Commercial FCC was provided from Izmir Refinery, Turkey.

Table 1. Properties of olive pomace

Proximate analysis		(wt%)
Moisture		8.1
Volatile matter		69.5
Fixed carbon		19.1
Ash		3.3
GCV, MJ kg ⁻¹		20.6
Ultimate analysis (dried weight)		(wt%)
C		50.6
H		5.9
N		2.3
S		0.2
O ^a		37.7
Component analysis (dried weight)		(wt%)
Cellulose		45.3
Hemicellulose		22.9
Lignin		31.1
Extractives		0.7

^a. Calculated from difference.

Red mud is a by-product of Aluminum company which contains high amount of iron oxides. FCC, ZSM-5, and red mud were tested as catalysts. Catalysts were calcinated at 550°C prior to each run. Red mud was activated according to procedure reported by Pratt and Christoverson.²⁰ BET and micropore surface area of catalysts were determined by N₂ adsorption measurement by Gemini V Series Surface Area Analyzers. Metal content of catalysts were analyzed by XRF analyzer (SPECTRO IQ II). Table 2 represents composition and some properties of catalysts.

2.2. Method

Table 2. Properties of catalysts

Catalyst	BET, m ² g ⁻¹	Micropore surface area, m ² g ⁻¹	Bulk density, g cm ⁻³	Main metal content
ZSM-5	355	237	0.34	SiO ₂ /Al ₂ O ₃ : 24
FCC	207	163	0.84	SiO ₂ /Al ₂ O ₃ : 0.68 Fe ₂ O ₃ :41.10%,
Red mud	158	n.d.	0.69	Al ₂ O ₃ :21.32%, SiO ₂ :17.02%

n.d.: not determined.

Pyrolysis experiments were carried out at two different heating rates; namely fast and slow in presence of catalyst. Analytical pyrolysis (Py-GC/MS) was performed using a CDS 2000 pyroprobe and a CDS AS-2500 autosampler (Chemical Data Systems, US). In a typical thermal pyrolysis, 10 mg of biomass sample was loaded into a quartz tube. In case of catalytic pyrolysis, biomass sample was placed between two catalyst layer with a ratio of 1:2:1 (catalyst: biomass: catalyst). The quartz tube was then placed to the probe, which is heated by a filament. Probe was heated to 500°C at a heating rate of 25°C min⁻¹ for slow pyrolysis and 1200°C min⁻¹ held at 500°C for 15 s. Sequential pyrolysis was also conducted with a fast heating rate (1200°C min⁻¹) at the various temperature intervals, i.e. 25°C-200°C, 200°C-300°C, 300°C-400°C, and 400°C-500°C. Sequential pyrolysis is denoted as S200, S300, S400 and S500, where numbers of labels show the final pyrolysis temperatures of each fragment.

A Perkin–Elmer AutoSystem XL Gas Chromatograph fitted with a DB 1701 column (60 m - 25 mm with 0.25 µm film thickness) was used to separate vapours produced with a split ratio of 1:25. The oven program was held temperature at 45°C for 4 min then heated to 240 °C at a rate of 4°C min⁻¹. The injector and detector temperatures were set at 28°C. Electron impact mass spectra were obtained by Perkin–Elmer MS GOLD (UK) at 70 eV. Proposed assignments of the main peaks were made from mass spectra detection using (NIST98 MS library). Identification of Py-GC/MS spectra was carried out by the comparison of the mass ions (m/z) of each peak. Relative area of individual compounds was calculated by taking into the consideration the GC peak areas to semi-quantify these compounds detected. Compounds that had concentration higher than 0.3% took into account for the calculation of relative area. The detected compounds were classified in terms of their chemical structures.

Thermal behaviour of olive pomace was also investigated in a thermogravimetric analyzer (Elmer Diamond TG/DTA) under N₂ gas with a flow rate of 100 ml min⁻¹. Different heating rates (5°C min⁻¹, 10°C min⁻¹, 25°C min⁻¹, 50°C min⁻¹ and 75°C min⁻¹) were applied. Approximately 10 mg of olive pomace was placed in a ceramic crucible and heated from room temperature up to 900°C. Iso-conversional models, namely Kissinger-Akahira-Sunose (KAS) and Flynn-Wall-Ozawa (FWO) were applied to determine apparent activation energy of olive pomace pyrolysis. KAS and FWO methods can be expressed by Equations (1) and (2), respectively.

$$\ln\left(\frac{\beta}{T^2}\right) = \ln\left[\frac{AE_a}{Rg(\alpha)}\right] - \frac{E_a}{RT} \quad (1)$$

$$\log(\beta) = \log\left[\frac{AE_a}{Rg(\alpha)}\right] - 2.315 - 0.457\frac{E_a}{RT} \quad (2)$$

where, β is the heating rate (K s⁻¹). A is the pre-exponential factor (s⁻¹), E_a is the apparent activation energy (kJ mole⁻¹). R is the gas constant (8.314 J mole⁻¹.K⁻¹). T is the reaction temperature (K) and $g(\alpha)$ is the temperature-independent function of reaction model. The conversion degree (α) is described in Eq. (3).

$$\alpha = \frac{(m_i - m_t)}{(m_i - m_f)} \quad (3)$$

where, m_i and m_f are the initial and final mass of olive pomace. m_t is the mass of olive pomace at time t . As the validity of iso-conversional method is limited according to conversion range, the values of E_a were determined in the conversion range of 0.1 and 0.8 for both models. E_a values were determined by plotting $\ln(\beta/T^2)$ against $1/T$ for KAS, while they were determined from linear plot of $\log(\beta)$ versus $1/T$ for OFW.

3. RESULTS AND DISCUSSION

3.1. Kinetic studies of olive pomace

The KAS and OFW plots of different conversion values (α) are presented in Figure 1. The coefficient of determination (R^2) values were higher than 0.95 for all cases, which is the evident of good fitting of model. In both methods, apparent activation energy increased at higher conversion degrees and temperatures. Yet, activation energy is not linearly dependent on the conversion. Lignin in biomass may be responsible for higher activation energy at higher conversion values. At higher temperatures, condensation reactions of the aromatic structure in lignin can occur, causing an increase in E_a .⁵ E_a values of OFW and KAS were quite similar for all conversion values. The mean values of E_a were found to be 105.6 kJ mole⁻¹ for KAS and 110.2 kJ

mole⁻¹ for OFW (see Table 3). Calculated E_a values in this study were close and lower than that in previous studies.¹⁶ Mishra and Mohanty¹⁶ reported that activation energies of different biomasses such as pine sawdust, poplar wood, rice husk and olive cake were between 127.8-350.2 kJ mole⁻¹ for KAS and 103.2-342.1 kJ mole⁻¹ for OFW model depending on the biomass type and heating rate.

Table 3. Activation energies at different conversion degrees

	KAS	R ²	OFW	R ²
Conversion (α)				
0.1	75.0	0.9556	80.0	0.9648
0.2	78.1	0.9704	83.6	0.9769
0.3	86.7	0.9691	91.9	0.9754
0.4	99.6	0.9740	104.5	0.9789
0.5	113.2	0.9779	117.7	0.9817
0.6	123.4	0.9839	127.5	0.9865
0.7	129.7	0.9824	133.7	0.9851
0.8	138.8	0.9874	142.6	0.9893
Mean	105.6		110.2	

3.2. Sequential pyrolysis

Sequential pyrolysis results for olive pomace are shown in Figure 2. The total amount of compounds detected was above 79% of total compounds. Notable differences on compounds can be seen in the first stage, which is a fraction of decomposed products up to 200°C. S-200 was found to have highest organic acids, namely acetic acid and heteroatom containing compounds. High acetic acid yield is in agreement with previous study conducted by Martinez and co-workers.²¹ Acetyl groups in hemicellulose started to eliminate at lower temperatures, which yielded acetic acid.

Phenolic compounds, mainly 2,6-dimethoxy-phenol, 2-methoxy-4-vinyl-phenol and 2-methoxy-phenol, started to form at further stages due to lignin decomposition at elevated temperatures. At lower temperature, ketone formation was lower than that of further steps. In the same manner, furans mainly occurred above 300°C. Levoglucosan was mainly formed at the first stage. Interestingly, levoglucosan could still observe above 300°C without decomposition. It should be also noted that bio-oil from second stage (S-300) had the highest furfural formation (2.97 %).

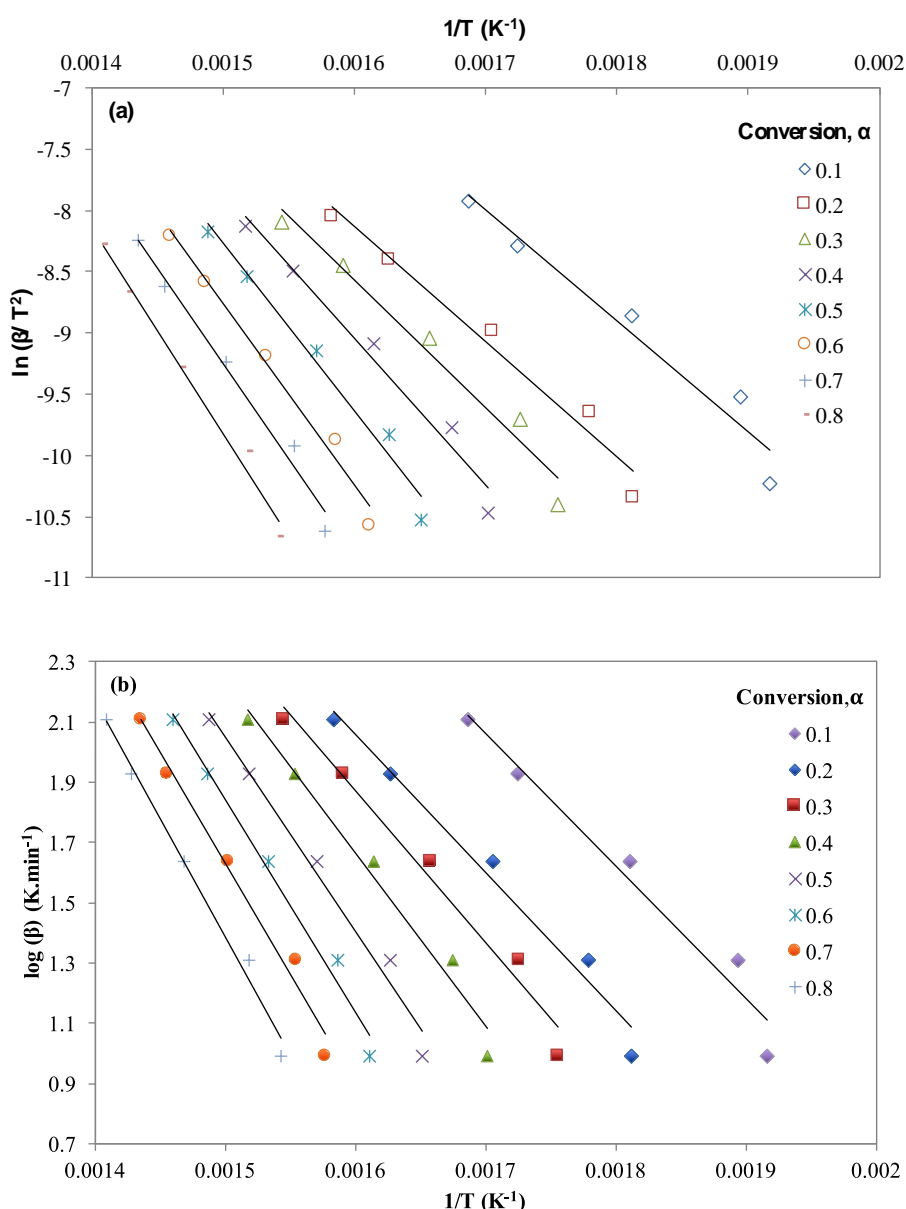


Figure 1. a) The plots of $\ln(\beta T^2)$ against $1/T$ for KAS method, b) The plots of $\log(\beta T^2)$ against $1/T$ for OFW method.

In a previous study done by Greenhalf and co-workers,²² sequential pyrolysis of willow SR was conducted at fast (1500°C/min) and slow (25°C/min) heating rates. They proposed that levoglucosan was converted into furfural at high heating rate, where as 2-furan methanol was obtained at lower heating rate. Based on these results, it is possible to obtain selective liquid products by sequential pyrolysis which makes the bio-oil more feasible for biorefinery purposes.

3.3. Effect of heating rate on pyrolysis products

Thermal experiments were performed in order to investigate the heating rates on bio-oil composition (Figure 3).

From Figure 3, some differences were found in the bio-oil compositions. For both heating rates, phenolic compounds are the main compounds in bio-oil. The amount of phenolics in bio-oil from fast pyrolysis was less than that from slow pyrolysis. This result is probably due to the fact that longer reaction time led to polymerization of phenolic compounds and formation of high molecular weight multi-ring structures which cannot be detected in GC-MS.²³

Fast pyrolysis produced more organic acids, particularly acetic acid and phenols whereas bio-oil from slow pyrolysis had more furans and aliphatic ketones, aldehydes and esters.

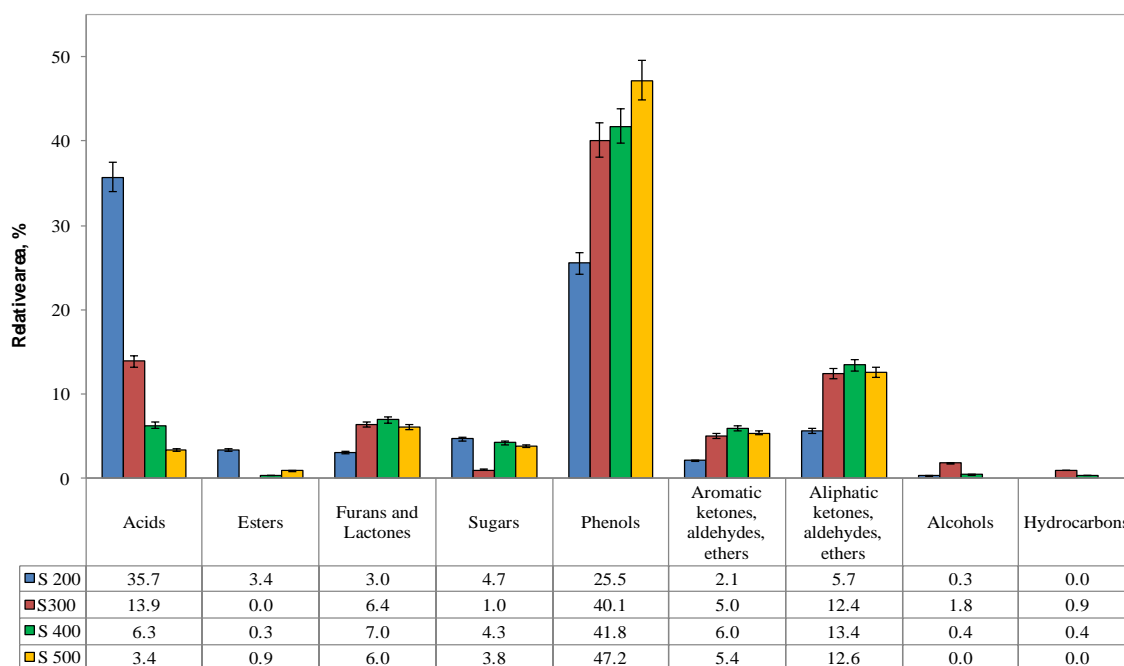


Figure 2. Relative peak areas of the products obtained from sequential pyrolysis.

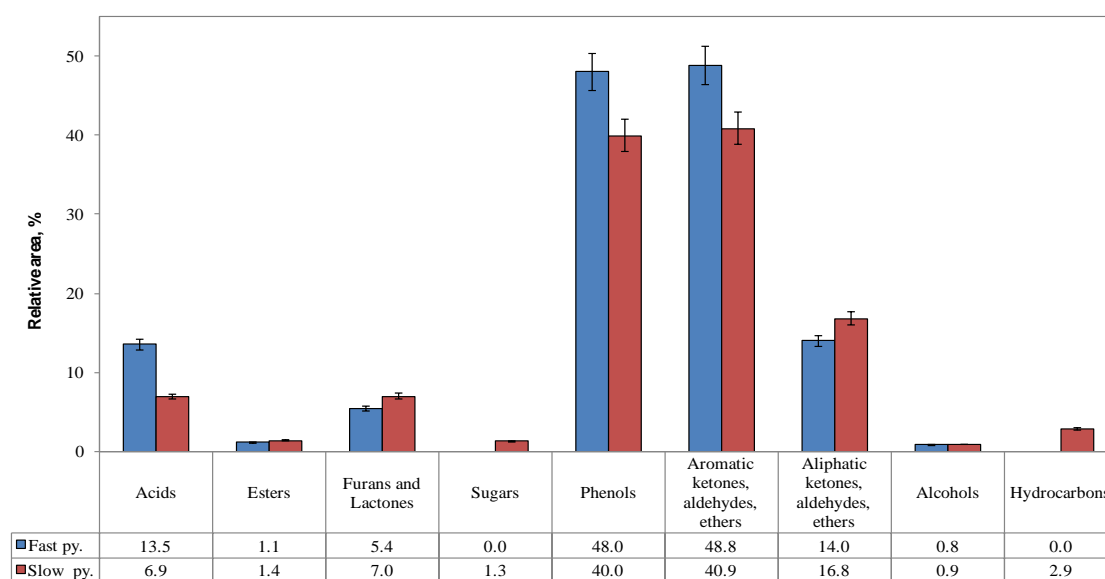


Figure 3. Relative peak areas of the products obtained by slow and fast pyrolysis.

Contrary to our results, Saftari and co-workers,²³ who investigated the effect of heating rate and temperature on products of pyrolysis of six different biomass, reported that high heating rate led to decrease in alcohol, ketone and aldehyde content, resulting from secondary reactions. It should be noted that long reaction times with slow heating rate may endorse secondary reactions, leading to convert organic acids to

other organic compounds. In addition, no hydrocarbons was obtained in fast pyrolysis whereas a small amount of hydrocarbons were detected in bio-oil from slow pyrolysis.

It was also noticed that distribution of individual furanic compounds varies at different heating rates (Table 3). The quantities of each individual compounds

were partially higher in case of slow heating rate. However, only the amount of furfural was slightly higher at fast heating rate. This result was consistent with possible mechanism of levoglucosan decomposition proposed by Greenhalf and co-workers.²² It was stated that the short residence times prevented the proton addition, resulting in the formation of furfural.

Table 3. Furanic compounds at different heating rates, relative area %.

	Fast Pyrolysis	Slow pyrolysis
Furan, 2-methyl-	-	0.5
Furfural	2.8	2.3
2(3H)-furanone, 5-methyl	-	0.32
Ethanone, 1-(2-furanyl)-	0.4	0.5
2-furan methanol	0.6	0.9
2-furancarboxaldehyde, 5-methyl-	-	0.3
2(5H)-furanone	0.8	1.0
Benzofuran, 2,3-dihydro-	0.5	0.6
Benzofuran, 6-methoxy-3-methyl-	0.3	0.5
Total	5.4	6.92

3.4. The effect of catalyst

Three different catalysts were studied in order to investigate the effect on pyrolysis product distribution in case of slow and fast heating rate (Figure 4).

In case of fast pyrolysis, all catalysts except for RM did not significantly effect on products. In presence of RM, phenolic compounds were decomposed while the relative amount of acids, furans and aliphatic ketones/aldehydes/ethers increased.

Differently from fast pyrolysis, bio-oil content varied depending on the catalyst in case of slow pyrolysis. Acidic compounds were increased in presence of all catalysts. Phenolic compounds were dramatically decreased in presence of RM and ZSM-5 whereas higher amount of phenolics were detected in bio-oil obtained in presence of FCC. It is known that ZSM-5 catalyst provides aromatization resulting from decomposition of phenolic composition.²⁴ However, none of aromatic compounds was detected in all pyrolysis products. This may be due to polymerization of aromatic compounds into high molecular weight compounds such as PAH and secondary coke formation onto catalyst surface.^{25,26}

On the other hand, the effect of RM on bio-oil

consumption is significant for both heating rate. The amount of phenols and aromatic ketones/aldehydes/ethers dramatically dropped by using RM, particularly in slow pyrolysis. This decrease can be attributed to formation of PAH compounds and coke formation in presence of RM as in case of ZSM-5. Similar results were found in previous studies reported by Veses and co-workers.²⁷ and Gupta and co-workers.²⁸ Gupta and co-workers²⁸ reported that relative yields of furfurals and organic acids increased and phenol yields decreased by using RM. They concluded that RM had furfural selectivity and facilitated the cleavage of carbon-carbon and carbon-oxygen bond in C6 and C5 molecules. In addition, high yield of acetic acid, which is product of hemicellulose via deacetylation, was attributed to synergistic effect of individual metal oxides in RM, mainly Fe₂O₃, Al₂O₃ and TiO₂. On the other hand, Veses and co-workers²⁷ found that PAH content of bio-oil decreased in case of mineral based catalysts whilst RM led to form PAH compounds. Since a considerable amount of phenols were converted into PAH, the relative percentages of acids, furan and aliphatic ketones/aldehydes/ethers increased in bio-oil.

4. CONCLUSIONS

In this study, pyrolysis of olive pomace at different conditions was investigated by using Py-GC/MS and TGA techniques. E_a of olive pomace pyrolysis is close (105.6 kJ mole⁻¹ for KAS method and 110.2 for OFW) and lower than that of different types of biomasses. For all cases phenolic compounds is the major compound ranging from 15.9% to 49.3% depending on experimental conditions. It was found that enrichment of individual organic compounds was achieved by conducting pyrolysis at different temperature intervals. Sequential pyrolysis seems a promising method to separate pyrolysis products, such as production of organic acids and alcohols at the low temperature stages, ketones/aldehydes and phenols at the high temperatures.

In case of catalytic pyrolysis, the effect of catalyst was more pronounced in case of slow heating rate due to high longer contact time between catalyst and pyrolysis vapor. Slow pyrolysis secondary reactions may take place at slow heating rates, resulting in formation of high molecular weight compounds via depolymerization. RM had the most effective catalyst on formation of acetic acid and furans while it decomposed phenolic compounds by reducing the yield from 48.0% to 36.6% and 40% to 15% in case of fast and slow pyrolysis, respectively. This study therefore exhibits a promising approach to produce targeted chemical compounds by selecting specific conditions for pyrolysis process.

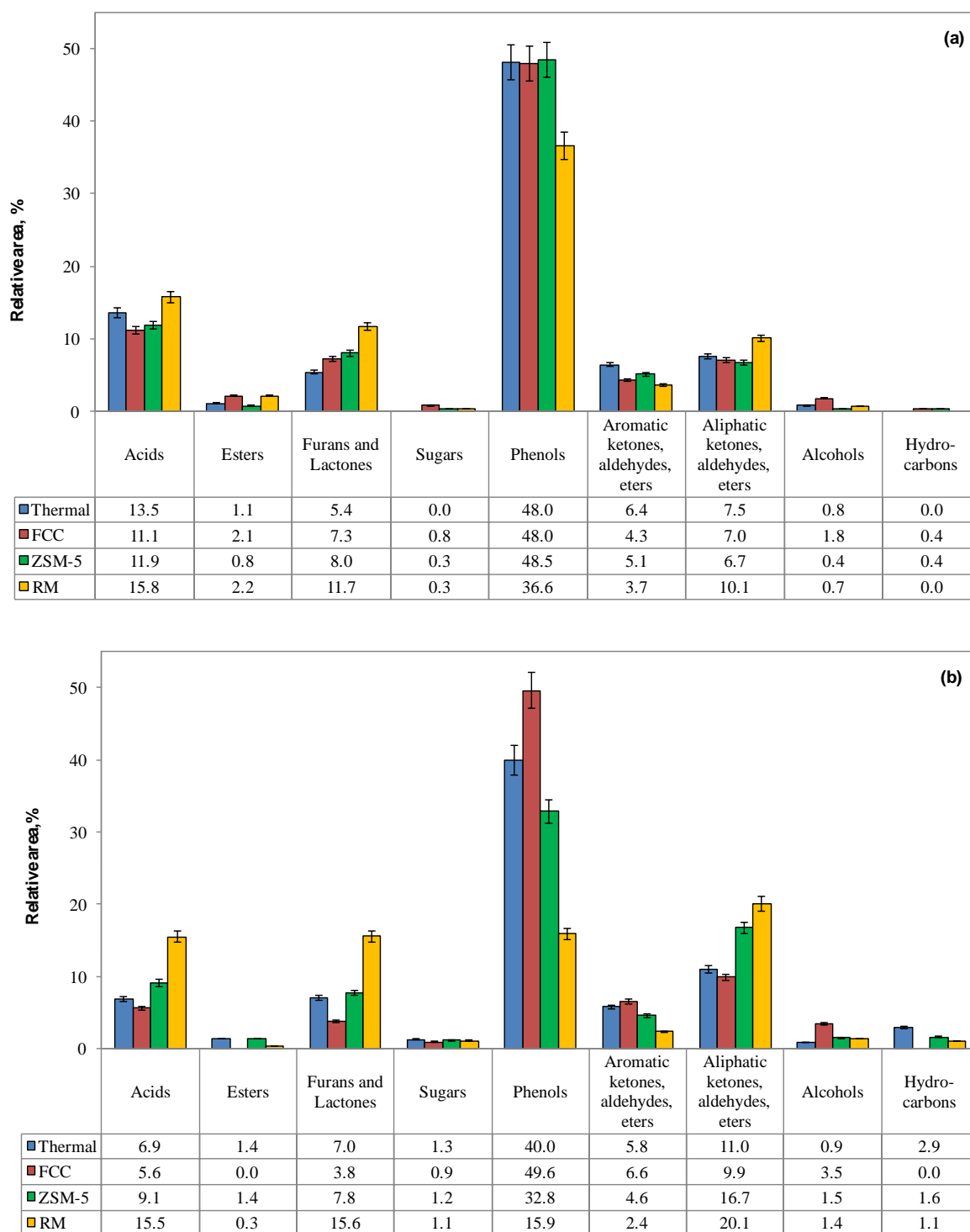


Figure 4. Effect of catalyst on bio-oil composition under a) fast heating rate, b) slow heating rate.

ACKNOWLEDGEMENTS

The author would like to acknowledge for BRISK project for financial support to visit EBRI (UK) laboratories and Dr. Daniel Nowakowski for helping Py-GC/MS studies.

Conflict of interests

I declare that there is no a conflict of interest with any person, institute, company, etc.

REFERENCES

1. Pradhan, P.; Mahajani, S. M.; Arora, A. *Fuel Process. Technol.* **2018**, 181, 215-232.
2. Sharifzadeh, M.; Sadeqzadeh, M.; Guo, M.; Borhani, T. N.; Konda, N. V. S. N. M.; Garcia, M. C.; Wang, L.; Hallett, J.; Shah, N. *Prog. Energ. Combust.* **2019**, 71, 1-80.
3. Wang, S.; Dai, G.; Yang, H.; Luo, Z. *Prog. Energ. Combust.* **2017**, 62, 33-86.
4. Hidayat, S.; Abu Bakar, M. S.; Yang, Y.; Phusunti, N.; Bridgwater, A. V. *J. Anal. Appl. Pyrol.* **2018**, 134, 510-519.
5. Wang, B.; Xu, F.; Zong, P.; Zhang, J.; Tian, Y.; Qiao, Y. *Renew. Energ.* **2019**, 132, 486-496.
6. Li, J.; Chen, Y.; Yang, H.; Zhu, D.; Chen, X.; Wang, X.; Chen, H. *Energ. Fuel* **2017**, 31, 7093-7100.
7. Greenhalf, C. E.; Nowakowski, D. J.; Harms, A. B.; Titiloye, J. O.; Bridgwater, A. V. *Fuel* **2013**, 108, 216-230.
8. Bridgeman, T. G.; Darvell, L. I.; Jones, J. M.; Williams, P. T.; Fahmi, R.; Bridgwater, a. V.; Barraclough, T.; Shield, I.; Yates, N.; Thain, S. C.; Donnison, I. S. *Fuel* **2007**, 86, 60-72.
9. Zhang, S.; Chenguang, W.; Kang, B.; Xinghua, Z.; Chiling, Y.; Renjie, D.; Longlong, M.; Changle, P. *Int. J. Agric. Biol. Eng.* **2017**, 10 (5), 214-225.
10. Zhou, M. xing; Li, W. tao; Wang, X.; Cui, M. shu; Yang, Y. P. *Catal. Today* **2018**, 302, 169-179.
11. Kaewpengkrow, P.; Atong, D.; Sricharoenchaikul, V. *Bioresour. Technol.* **2014**, 163, 262-269.
12. Li, P.; Chen, X.; Wang, X.; Shao, J.; Lin, G.; Yang, H.; Yang, Q.; Chen, H. *Energ. Fuel* **2017**, 17, 31, 3979-3986.
13. Wang, J.; Zhang, B.; Zhong, Z.; Ding, K.; Deng, A.; Min, M.; Chen, P.; Ruan, R. *Energ. Convers. Manage.* **2017**, 139, 222-231.
14. Zhang, B.; Zhong, Z.; Wang, X.; Ding, K.; Song, Z. *Fuel Process. Technol.* **2015**, 138, 430-434.
15. Feroso, J.; Mašek, O. *J. Anal. Appl. Pyrolysis* **2018**, 130, 249-255.
16. Mishra, R. K.; Mohanty, K. *Bioresour. Technol.* **2018**, 251, 63-74.
17. Souilem, S.; El-Abbassi, A.; Kiai, H.; Hafidi, A.; Sayadi, S.; Galanakis, C. M. *Recent Adv. Sustain. Manag.* **2017**, 1-28.
18. Duman, A. K.; Özgen, G. Ö.; Üçtuğ, F. G. *Sustain. Prod. Consum.* **2020**, 22, 126-137.
19. Pratt, K. C.; Christoverson, V. *Fuel* **1982**, 61, 460-462.
20. Li S.; Xu, S.; Liu, S.; Yang, C.; Lu, Q. *Fuel Process. Technol.* **2004**, 85, 1201-1211.
21. González Martínez, M.; Ojra-aho, T.; da Silva Perez, D.; Tamminen, T.; Dupont, C. *J. Anal. Appl. Pyrol.* **2019**, 137, 195-202.
22. Greenhalf, C. E.; Nowakowski, D. J.; Harms, A. B.; Titiloye, J. O.; Bridgwater, A. V. *Fuel* **2012**, 93, 692-702.
23. Safdari, M. S.; Amini, E.; Weise, D. R.; Fletcher, T. H. *Fuel* **2019**, 242, 295-304.
24. Zhang, M.; Resende, F. L. P.; Moutsoglou, A. *Fuel* **2014**, 116, 358-369.
25. Zhou, G.; Jensen, P. A.; Le, D. M.; Knudsen, N. O.; Jensen, A. D. *Green Chem.* **2016**, 18, 1965-1975.
26. Ben, H.; Ragauskas, A. J. *ACS Sustain. Chem. Eng.* **2013**, 1, 316-324.
27. Veses, A.; Aznar, M.; López, J. M.; Callén, M. S.; Murillo, R.; García, T. *Fuel* **2015**, 141, 17-22.
28. Gupta, J.; Papadikis, K.; Kozhevnikov, I. V.; Konyshcheva, E. Y. *J. Anal. Appl. Pyrol.* **2017**, 128, 35-43.



Synthesis and characterization of a new 2D-imine-linked covalent organic framework

 Lalehan AKYÜZ

Department of Chemistry Technology, Technical Vocational School, Aksaray University, Aksaray 68100, Turkey

Received: 10 July 2020; Revised: 21 August 2020; Accepted: 11 September 2020

*Corresponding author e-mail: lale_akyuz@hotmail.com

Citation: Akyüz, L. *Int. J. Chem. Technol.* 2020, 4 (2), 171-178.

ABSTRACT

Covalent organic structures (COFs) are extraordinarily porous solids defined as organic polymeric materials with large surface area. COF compounds are widely studied for nanotechnology applications. Additionally, there are applications for its usability in semiconductor technologies and drug delivery systems. Within the scope of this article, a new covalent organic structure (COF) was synthesized using triformylbenzene (TFB) and 3,3',5,5'-tetramethyl benzidine (TMB), which were not previously included in the literature. The compound synthesized here is the two-dimensional imine-linked COF (LA-COF-2) compound. The synthesized COF compound was characterized using FT-IR, SEM, TGA, PXRD and elemental analysis. The LA-COF-2 compound is composed of aggregated particles of approximately 200 nm. The thermal stability of LA-COF-2 compound is high and compatible with the literature. The compound is stable to base, N,N-Dimethylacetamide (DMA) and water.

Keywords: Synthesis, characterization, covalent organic framework (COF).

Yeni bir 2D-imin bağlı kovalent organik yapının sentezi ve karakterizasyonu

ÖZ

Kovalent organik yapılar (COFs), geniş yüzey alanına sahip organik polimerik malzemeler olarak tanımlanan olağanüstü gözenekli katı maddelerdir. COF bileşikleri nanoteknoloji uygulamaları için geniş çapta incelenmektedir. Ek olarak, yarı iletken teknolojilerinde ve ilaç dağıtım sistemlerinde kullanılabilirliği için uygulamalar vardır. Bu proje kapsamında triformilbenzen (TFB) ve 3,3',5,5'-tetrametil benzidin (TMB) kullanılarak, daha önce literatürde yer almayan yeni bir kovalent organik kafes (covalent organic framework-COF) yapısı sentezlenmiştir. Burada sentezlenen bileşik, iki boyutlu imine bağlı COF (LA-COF-2) bileşiğidir. Sentezlenen COF bileşiği FT-IR, SEM, TGA, PXRD ve elementel analiz kullanılarak karakterize edildi. LA-COF-2 bileşiği, yaklaşık 200 nm'lik kümelenmiş partiküllerden oluşmaktadır. LA-COF-2 bileşiğinin termal kararlılığı yüksektir ve literatür ile uyumludur. Bileşik baz, N,N-dimetilasetamid (DMA) ve suya karşı kararlıdır.

Anahtar Kelimeler:Sentez, karakterizasyon, kovalent organik kafes (COF).

1. INTRODUCTION

Covalent organic frameworks (COFs) have extremely low densities which are a new type of porous organic material formed by the binding of organic units through strong covalent bonds between entirely light elements (C, Si, B, O, N). COFs have been firstly developed as the crystalline porous organic polymers via the dehydration reactions of 1,4-benzenediboric acid itself (COF-1) by Yaghi and co-workers. Then, COF-5 and COF-105 containing boronate ester bonds have been synthesized from the reaction of boric acids with catechol derived compounds.¹⁻² After the synthesis of COF-5 and COF-105, many more two-dimensional and three-dimensional COFs (2D and 3D COFs) having

different structures have been synthesized using monomers with different functional groups.³⁻⁸ Especially, due to the COFs derived from B-O bonds with low chemical stability, COFs containing C-N bonds such as imine,^{6,9-11} triazine¹² and hydrazone¹³ linkages have also been improved in addition to boron compounds, over times. In particular, two-dimensional crystalline COFs have attracted attention as porous crystalline polymers. 2D-COFs have been investigated for nanotechnology application areas such as conductivity,^{14,15} optoelectron devices,¹⁶ optical sensing,^{3,7,17} catalyzing¹⁸ and electrochemical sensing¹⁹ due to their electron rich, big π -delocalization and film forming properties.

Schiff base condensation reactions are widely used for the preparation of COFs via solvothermal reactions in sealed vials.¹ Herein, a new framework-based imine linked COF material has been designed and synthesized with the condensation reaction of building block 3,3',5,5'-tetramethyl benzidine (TMB) with linking unit triformylbenzene (TFB). The COF synthesis reaction was performed in under solvothermal conditions. The characterization of COF was investigated using FT-IR, SEM, TGA, PXRD and elemental analysis. In addition, the chemical stability of COF was investigated in base (6 N NaOH), N,N-Dimethylacetamide (DMA) and water by using TGA and FT-IR analyses.

2. MATERIALS AND METHODS

2.1. Chemical and reagents

TFB and TMB were obtained from Sigma Aldrich. mesitylene, 1,4-dioxane, ethanol, dimethylformamide and tetrahydro furan were purchased from Merck. All other reagents were of analytical grade.

2.2. FT-IR analysis

FT-IR spectra were obtained using a Perkin Elmer mark FT-IR Spectrophotometer. The spectra were recorded for starting materials and LA-COF-2 at the scanning range of 4,000-650 cm^{-1} .

2.3. Thermogravimetric analysis

The thermogravimetric analysis (TGA) was carried out on NETSZCH TGA-DSC Thermogravimetric Analyzer. The analyses were done under N_2 gas flow, and the samples were heated from 0°C to 700°C at 10 K/min.

2.4. Powder X-ray diffraction

Powder X-ray diffraction (PXRD) analyses were carried out using a full-fledged Bruker D8 Advance instrument with Cu $\text{K}\alpha$ line focused radiation at 40 kV and 40 mA from $2\theta = 3.0^\circ$ up to 90° .

2.5. Field emission-scanning electron microscopy (FE-SEM)

Scanning electron microscopy (SEM) was carried out using a LEICA/CAMBRIDGE LEO S-440 STEREOSCAN SEM to investigate the surface morphology of the samples. The materials were coated with gold as a thin layer using a Gatan Precision Etching Coating System (PECS).

2.6. Synthesis of LA-COF-2

TMB (32.979 mg, 0.155 mmole), TFB (14.595 mg, 0.09

mmole), 3 ml 1,4-dioxane and 0.6 ml 3 M acetic acid were poured into the pyrex tube. The pyrex tube was frozen with liquid N_2 and evacuated the 150 mTorr internal pressure. The evacuated pyrex tube was placed at 180°C in an oven and reaction was continued for 3 days to yield a yellow solid in pyrex tube. The precipitate was obtained by filtration and washed three times with 10 ml of anhydrous THF and DMA and acetone. The solid which is insoluble in common organic solvents was dried at 100°C for 12 h. Yield: 76%. Elemental analysis, calculated; $(\text{C}_{144}\text{H}_{126}\text{N}_{12})_n$: C 85.46; H 6.23; N 8.31. Found; C 84.01; H 6.91; N 8.82; O 0.26.

2.7. Chemical stability

The chemical stability of LA-COF-2 was investigated in 6 N NaOH, distilled water and DMA. Correctly weighed LA-COF-2 samples were placed in 20 ml of 6 N NaOH, DMA and distilled water and carefully mixed for 120 h. The mixtures were filtered by the centrifuge. The precipitate was dried at 100°C for 24 h. The dried samples were weighed again, and mass losses were determined. FT-IR analyses were repeated for the treated samples. Spectra were compared to the starting spectrum of LA-COF-2 samples. In addition, TGA thermograms were compared to determine the change in the thermal stability of the samples treated.

3. RESULTS AND DISCUSSION

LA-COF-2 shown in Figure 1a was synthesized by heating the suspension of 3,3'-dimethoxybiphenyl-4,4'-diamine and TFB in a mixture of 1,4-dioxane and aqueous acetic acid within the sealed pyrex tube. LA-COF-2 is insoluble in common organic solvents such as dimethyl sulfoxide, tetrahydrofuran, acetone, N,N-dimethylformamide. The honeycomb structure of LA-COF-2 is given in the Figure 1b.

3.1. FT-IR analysis

FT-IR analyses were performed to confirm the imine linkages formed between aldehyde and primary amine functional group of the starting material. The spectra of LA-COF-2, TMB and TFB compounds are given in Figure 2a. FT-IR spectrum of LA-COF-2 showed that the imine linkage peak (C=N stretching) was observed at 1626 cm^{-1} . When compared the spectra of starting materials with the LA-COF-2, the C=O and N-H bands of starting materials are weaker in LA-COF-2. The attenuation of the peaks is further evidence of the formation of the imine linkages. Also, it can be concluded that the weak peaks at these wave numbers were attributed to the unreacted terminal amino and aldehyde groups of COF.

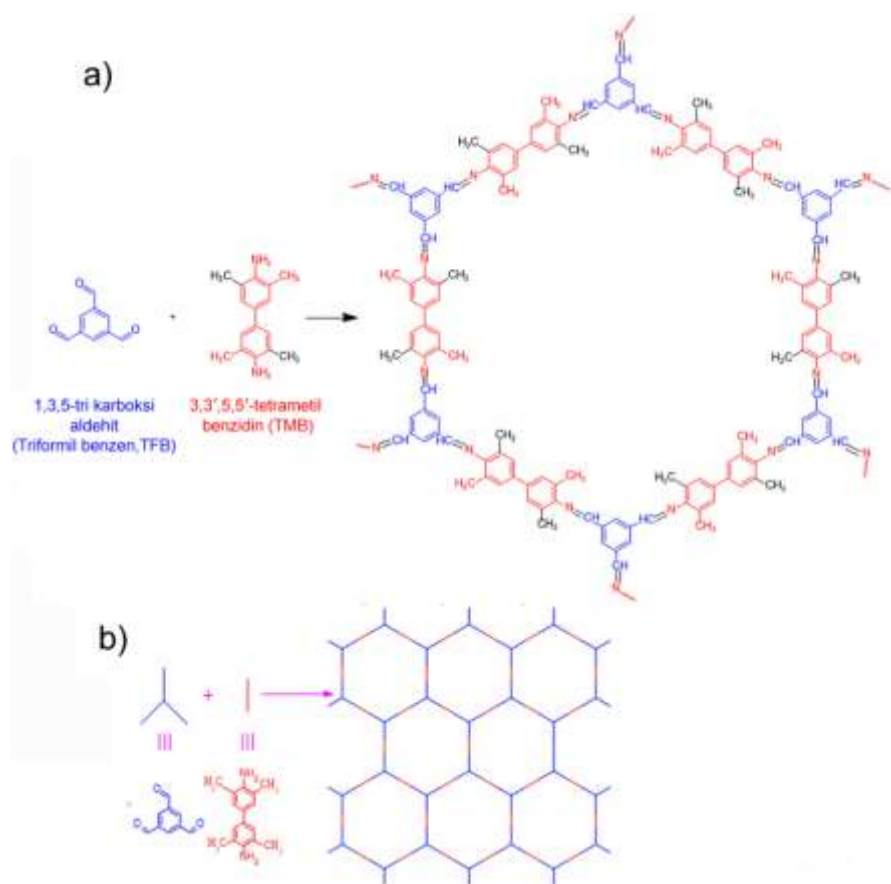


Figure 1. a) Synthesis of LA-COF-2, b) Honeycomb structure of LA-COF-2.

In addition, the stretching vibrations of C-N single bonds are weak or moderate in the wave numbers range of approximately $1080\text{--}1360\text{ cm}^{-1}$. Accordingly, in the LA-COF-2 compound, the peaks observed at a wave number of 1131.30 cm^{-1} indicate the stretching vibrations of the C-N single bond of the imine structure. When the obtained spectrum was compared to the literature,^{6,10} it was seen that the similar spectrum was obtained.

3.2. PXRD analysis

The crystallinity of LA-COF-2 was investigated by Cu $K\alpha$ radiation with powder X-ray diffraction (PXRD) analysis. X-ray diffractogram of LA-COF-2 compound is shown in Figure 2b. The peak observed at $2\theta = 1.98^\circ$ indicates that the compound has a crystalline structure. Banarjee and co-workers²⁰ explained that when the pores of the COF compounds increased in width, the sharp peak position observed at $\sim 5^\circ$ was observed at lower 2θ values. As seen in Figure 2c, the pore apertures of LA-COF-2 were calculated as 30 \AA . On the other hand, the wide peak observed at about $2\theta = 15^\circ$ can be linked to the π - π interactions of the 2D layers shown in Figure 2d.

Similar PXRD spectra for imine-linked COF structures have been also obtained for the TpBD-COF (triformylphloroglucinol-benzidine) series by Banarjee and co-workers.²⁰ Similarly, the results from the present study are consistent with previous studies.²¹⁻²³

The previously reported three-dimensional diamond structure, the imine-bonded COF-300, is arranged with nitrogen atoms of imine bonds. Due to this arrangement, it was reported that COF-300 was reported to be able to coordinate with metal ions with less effect. Accordingly, a new imine-linked LA-COF-2 which is in two-dimensional layered-sheet structure (Figure 2d) can be an ideal choice for incorporating a variety of metal ions.

3.3. SEM analysis

The surface morphologies of the synthesized LA-COF-2 compound were examined using SEM analyses. Figures 3a and 3b show the SEM images taken in various magnifications of LA-COF-2. As seen in this figures, the LA-COF-2 compound consists of particles aggregated approximately 200 nm in size. These particles have a layered leaf-shaped morphology.

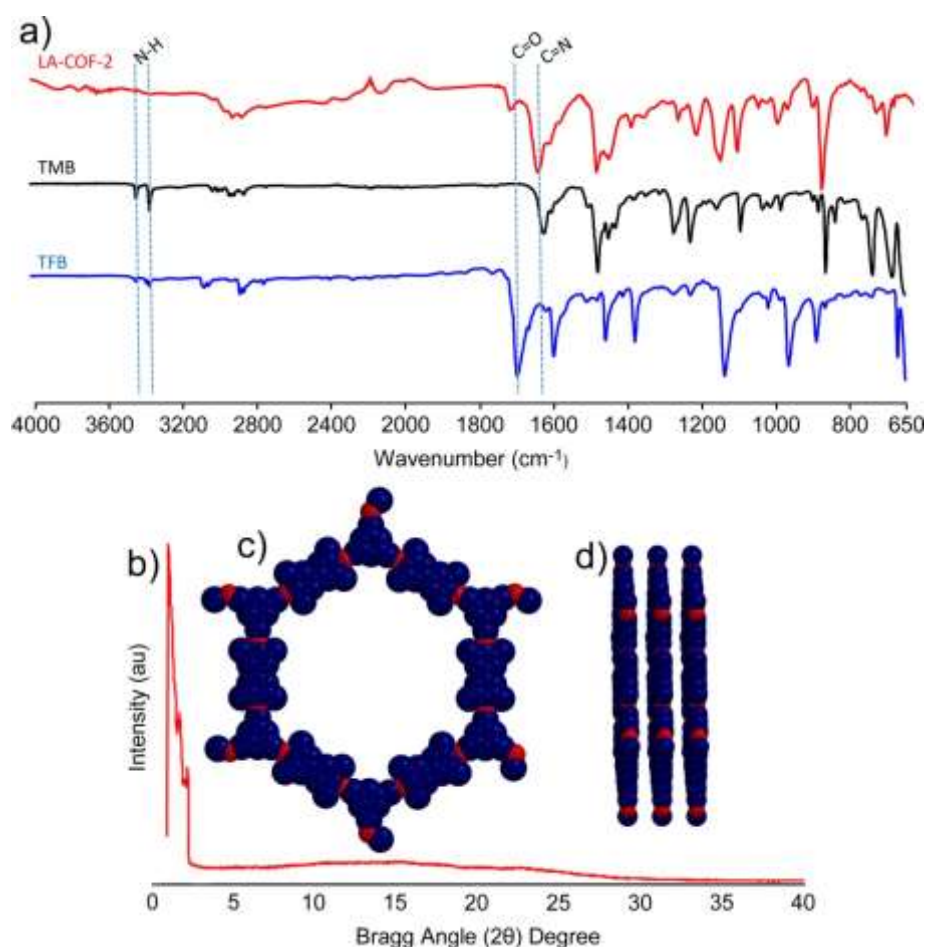


Figure 2. a) FT-IR spectra of LA-COF-2, TMB and TFB, b) X-ray diffractogram of LA-COF-2, c) 3D model of LA-COF-2, d) Side representation view of 2D-layers of LA-COF-2.

It can be thought that this structure is formed as a result of the π - π interaction of hexagonal units and the layers coming together to form aggregates.

In addition, EDX mapping analysis was performed for the synthesized COF compound. Figure 3c, 3d and 3e show the carbon, nitrogen and oxygen distribution of LA-COF-2 compound. Figure 3f illustrates the EDX spectrum, which gives the percentages of the atoms in the compound by weight. The amounts of carbon, nitrogen and oxygen in LA-COF-2 have been determined as 85.44%, 10.05% and 4.50%, respectively.

Results obtained with EDX mapping analysis are compatible with elemental analysis results. The amount of oxygen was calculated as 0.26% by elemental analysis which is a more precise analysis method. Considering the chemical structure, it can be said that the oxygen observed in the LA-COF-2 compound is the remaining terminal oxygen of the unreacted triformyl benzene.

3.4. TGA analysis

Thermogravimetric analysis was used to investigate the thermal stability of LA-COF-2 and thermogram is given in Figure 4. The maximum decomposition temperature for the LA-COF-2 was determined as 446°C. The second decomposition temperature was observed as 529°C, and when the temperature reaches to 700°C, it was seen that 71% of the framework structure was degraded. The thermal stability of the synthesized compound is very close to the thermal stability values of imine-linked COF compounds obtained in previous studies.^{9,10,24}

4.5. Chemical stability of LA-COF-2

In order to determine the chemical stability of LA-COF-2, 15 mg of the samples were put into 20 ml of water, DMA and 6 N NaOH solution for 5 days. Samples recovered by filtration were weighed again after drying.

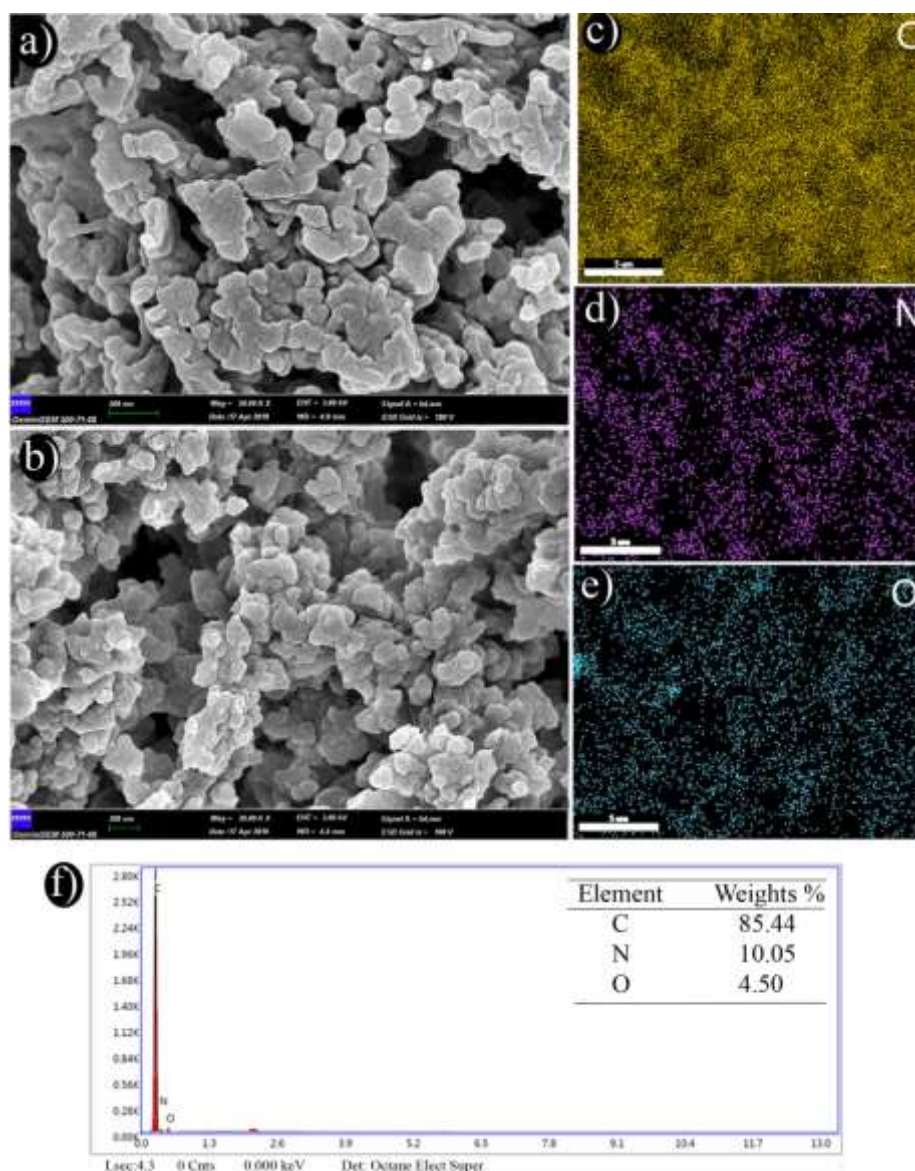


Figure 3. SEM images of LA-COF-2: a) 50 KX, b) 30 KX magnifications. EDX mapping analysis of LA-COF-2: c) C, d) N, e) O, f) EDX spectrum of LA-COF-2 (inset table shows weight percentage of C, N and O atoms).

No mass loss was observed as a result of weighing. TGA and FTIR analyses were performed on the samples treated with solvents.

DTG and TG% thermograms for LA-COF-2 and solvent treated LA-COF-2 samples are given in Figures 5a and 5b, respectively. In addition, DTG max and total mass loss values of the samples are shown in a table given in Figure 5b. As can be seen from the table, the main decomposition temperature of about 446°C for LA-COF-2 compound did not change significantly when the samples were treated with the solvent. After 446°C, all samples began to decompose at 24.4-29.4% up to 700°C.

As understood from TGA thermogram, LA-COF-2 compound was seemed to remain stable when treated with different solvents for 5 days. FT-IR spectra of LA-COF-2 compound and solvent treated LA-COF-2 samples are given in Figure 5c. The C=N stretching peak, which specifically indicates the imine structure in the spectrum, was recorded at approximately the same wave number after solvent treatment. However, in the sample treated with NaOH, this peak was observed at different severity. But, no change in peak intensity was observed in the other solvents. The obtained results proved that LA-COF-2 compound has high chemical stability against base, water and organic solvent and structural integrity is maintained in the solvent.

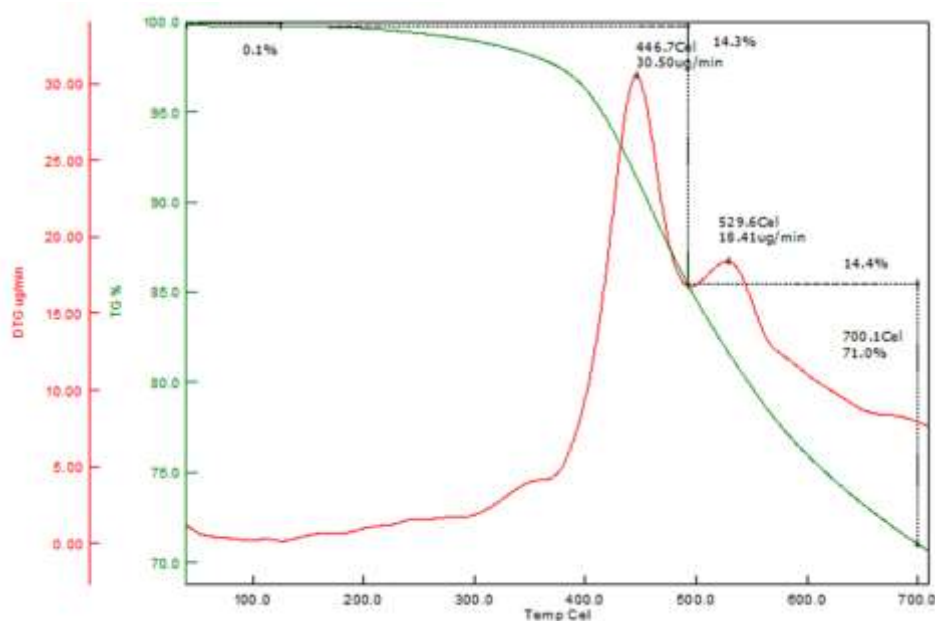


Figure 4. TGA thermogram of LA-COF-2.

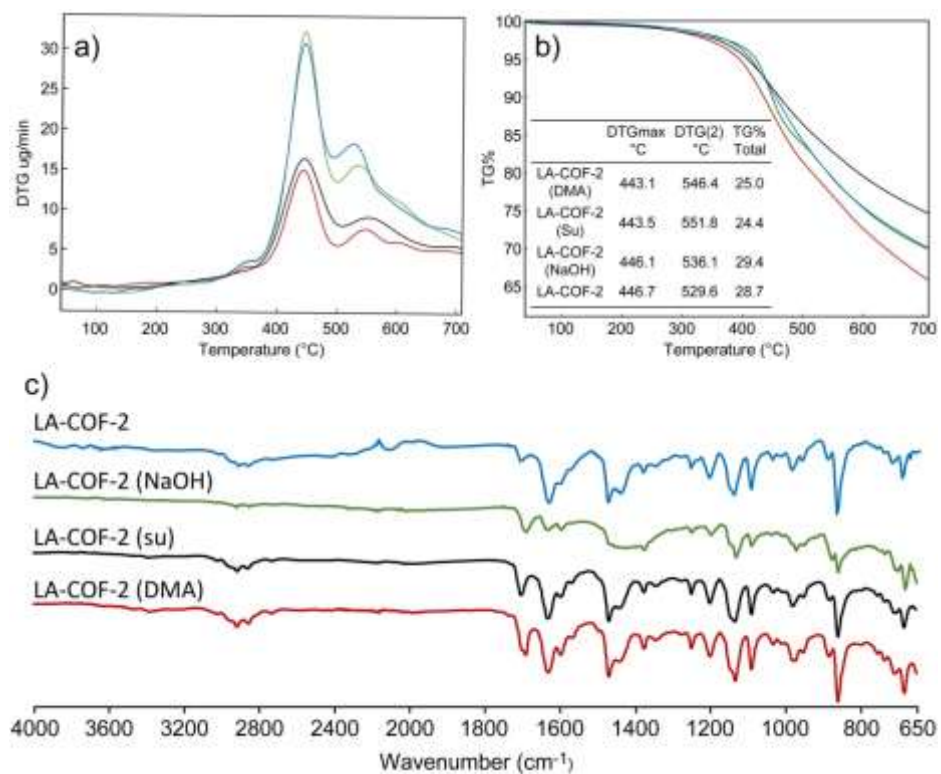


Figure 5. a) DTG curves of LA-COF-2 and solvent treated LA-COF-2, b) TG% curves of LA-COF-2 and solvent treated LA-COF-2, c) FT-IR spectra of LA-COF-2 and solvent treated LA-COF-2.

It has been reported in the literature, that the previously synthesized COFs are insoluble in water and common organic solvents such as hexane, tetrahydrofuran, acetonitrile, acetone, methanol and N,N-dimethylformamide.^{6,13} However, it has not been investigated under hard conditions such as NaOH. Whereas, LA-COF-2 was found to be stable to NaOH in the present study.

4. CONCLUSIONS

In the present paper, a new imine-linked COF molecule with high chemical and thermal stability was successfully synthesized. The vibration peak of the imine bond (C=N) of LA-COF-2 was observed at 1626 cm⁻¹ wave number. As a result of the images recorded by SEM analysis, it was determined that LA-COF-2 compound consisted of aggregated particles approximately 200 nm in size. From TGA analysis, it was determined that the synthesized compound had high thermal stability. It was observed that the synthesized LA-COF-2 compound remained stable to base, DMA and water. As a result, it was concluded that LA-COF-2 could be used in nanotechnology application areas such as drug delivery and gas storage thanks to its porous structure.

ACKNOWLEDGEMENTS

This work was supported by Aksaray University Research Fund for financial support through Project numbers BAP 2018-025.

Conflict of interests

Author declares that there is no a conflict of interest with any person, institute, company, etc.

REFERENCES

- Cote, A. P.; Benin, A. I.; Ockwig, N. W.; O'Keeffe, M.; Matzger, A. J.; Yaghi, O. M. *Science* **2005**, 310 (5751), 1166-1170.
- El-Kaderi, H. M.; Hunt, J. R.; Mendoza-Cortés, J. L.; Côté, A. P.; Taylor, R. E.; O'Keeffe, M.; Yaghi, O. M. *Science* **2007**, 316 (5822), 268-272.
- Dogru, M.; Sonnauer, A.; Gavryushin, A.; Knochel, P.; Bein, T. *Chem. Commun.* **2011**, 47 (6), 1707-1709.
- Spitler, E. L.; Dichtel, W. R. *Nature Chem.* **2010**, 2 (8), 672.
- Tilford, R. W.; Gemmill, W. R.; zur Loye, H.-C.; Lavigne, J. J. *Chem. Mater.* **2006**, 18 (22), 5296-5301.
- Uribe-Romo, F. J.; Hunt, J. R.; Furukawa, H.; Klock, C.; O'Keeffe, M.; Yaghi, O. M. *J. Am. Chem. Soc.* **2009**, 131 (13), 4570-4571.
- Wan, S.; Guo, J.; Kim, J.; Ihee, H.; Jiang, D. *Angew. Chem. Int. Edit.* **2008**, 47 (46), 8826-8830.
- Wan, S.; Guo, J.; Kim, J.; Ihee, H.; Jiang, D. *Angew. Chem. Int. Edit.* **2009**, 48 (30), 5439-5442.
- Albacete, P.; Martinez, J. I.; Li, X.; Lopez-Moreno, A.; Mena-Hernando, S. a.; Platero-Prats, A. E.; Montoro, C.; Loh, K. P.; Perez, E. M.; Zamora, F. J. *Am. Chem. Soc.* **2018**, 140 (40), 12922-12929.
- Rabbani, M. G.; Sekizkardes, A. K.; Kahveci, Z.; Reich, T. E.; Ding, R.; El-Kaderi, H. M. *Chem. Eur. J* **2013**, 19 (10), 3324-3328.
- Akyuz, L. *Micropor. Mesopor. Mat.* **2020**, 294, 109850.
- Kuhn, P.; Antonietti, M.; Thomas, A. *Angew. Chem. Int. Edit.* **2008**, 47 (18), 3450-3453.
- Uribe-Romo, F. J.; Doonan, C. J.; Furukawa, H.; Oisaki, K.; Yaghi, O. M. *J. Am. Chem. Soc.* **2011**, 133 (30), 11478-11481.
- Ding, H.; Li, Y.; Hu, H.; Sun, Y.; Wang, J.; Wang, C.; Wang, C.; Zhang, G.; Wang, B.; Xu, W. Zhang, D. *Chem-Eur. J.* **2014**, 20 (45), 14614-14618.
- Cai, S.-L.; Zhang, Y.-B.; Pun, A. B.; He, B.; Yang, J.; Toma, F. M.; Sharp, I. D.; Yaghi, O. M.; Fan, J.; Zheng, S. R. *Chem. Sci.* **2014**, 5 (12), 4693-4700.
- Dogru, M.; Handloser, M.; Auras, F.; Kunz, T.; Medina, D.; Hartschuh, A.; Knochel, P.; Bein, T. *Angew. Chem.- Ger Edit* **2013**, 125 (10), 2992-2996.
- Zhang, W.; Qiu, L.-G.; Yuan, Y. P.; Xie, A. J.; Shen, Y. H.; Zhu, J. F. *J. Hazard. Mater.* **2012**, 221, 147-154.
- Ding, S.-Y.; Gao, J.; Wang, Q.; Zhang, Y.; Song, W. G.; Su, C.-Y.; Wang, W. *J. Am. Chem. Soc.* **2011**, 133 (49), 19816-19822.
- Ben, T.; Shi, K.; Cui, Y.; Pei, C.; Zuo, Y.; Guo, H.; Zhang, D.; Xu, J.; Deng, F.; Tian, Z. *J. Mater. Chem.* **2011**, 21 (45), 18208-18214.
- Karak, S.; Kandambeth, S.; Biswal, B. P.; Sasmal, H. S.; Kumar, S.; Pachfule, P.; Banerjee, R. *J. Am. Chem. Soc.* **2017**, 139 (5), 1856-1862.

21. Mitra, S.; Sasmal, H. S.; Kundu, T.; Kandambeth, S.; Illath, K.; Diaz Diaz, D.; Banerjee, R. *J. Am. Chem. Soc.* **2017**, 139 (12), 4513-4520.

22. Bunck, D. N.; Dichtel, W. R. *J. Am. Chem. Soc.* **2013**, 135 (40), 14952-14955.

23. Chandra, S.; Kandambeth, S.; Biswal, B. P.; Lukose, B.; Kunjir, S. M.; Chaudhary, M.; Babarao, R.; Heine, T.; Banerjee, R. *J. Am. Chem. Soc.* **2013**, 135 (47), 17853-17861.

24. Wu, C.; Liu, Y.; Liu, H.; Duan, C.; Pan, Q.; Zhu, J.; Hu, F.; Ma, X.; Jiu, T.; Li, Z. *J. Am. Chem. Soc.* **2018**, 140 (31), 10016-10024.



Quantitative analysis of phenolic compounds of commercial basil cultivars (*Ocimum basilicum* L.) by LC-TOF-MS and their antioxidant effects

Nusret GENÇ¹, Mahfuz ELMASTAŞ², İsa TELCİ³, Ramazan ERENLER^{1,*}

¹Department of Chemistry, Faculty of Arts and Sciences, Tokat Gaziosmanpaşa University, Tokat 60240, Turkey

²Department of Biochemistry, Faculty of Pharmacy, University of Health Sciences, Istanbul, Turkey

³Department of Field Crops, Faculty of Agricultural Sciences and Technologies, Isparta University of Applied Sciences, Isparta 32260, Turkey

Received: 16 September 2020; Revised: 09 October 2020; Accepted: 13 October 2020

*Corresponding author e-mail: renerler@gmail.com

Citation: Genç, N.; Elmastaş, M.; Telci, İ.; Erenler, R. *Int. J. Chem. Technol.* 2020, 4 (2), 179-184.

ABSTRACT

Basil (*Ocimum basilicum* L.), an aromatic and medicinal plant, is used for food and pharmaceutical purposes. In this work, quantitative analyses of phenolic compounds for commercial basil cultivars, which are Sweet (1), Purple (2), Lettuce (3), Brush (4) grown in Tokat city in Turkey's ecology, were executed by Liquid Chromatography Time-of-Flight Mass Spectrometry (LC-TOF-MS). Antioxidant activities of related genotypes were determined using 2,2-Diphenyl-1-picrylhydrazyl (DPPH)'s radical, 2,2'-Azino-bis(3-ethylbenzothiazoline-6-sulfonic acid (ABTS)'s diammonium salt and the ferric reducing antioxidant power (FRAP) assays. The activity-compound relationship was revealed. Brush (4) genotype revealed the most DPPH [296 µmole TE (Trolox equivalent/g DW (gram dry weight)], ABTS (706 µmole TE/g DW), and FRAP (650 µmole TE/g DW) activities. It was determined that rosmarinic acid was in the highest amount in all genotypes. Among the genotypes, it was determined that Lettuce contained the most rosmarinic acid with a value of 180460.6 (mg kg⁻¹ DW).

Keywords: *Ocimum basilicum* L., antioxidant activity, basil cultivar, quantitative analysis, LC-TOF-MS.

Ticari fesleğen çeşitlerinin (*Ocimum basilicum* L.) fenolik bileşiklerinin LC-TOF-MS ile kantitatif analizi ve antioksidan etkileri

ÖZ

Aromatik ve tıbbi bir bitki olan reyhan (*Ocimum basilicum* L.) gıda ve ilaç amaçlı kullanılmaktadır. Bu çalışmada, Türkiye'nin ekolojisinde Tokat şehrinde yetişen Sweet (1), Purple (2), Lettuce (3), Brush (4) olmak üzere dört ticari fesleğen çeşidinin fenolik bileşiklerinin kantitatif analizleri LC-TOF/MS ile gerçekleştirilmiştir. İlgili genotiplerin antioksidan aktiviteleri, 2,2-Difenil-1-pikrilhidrazil (DPPH) radikali, 2,2-azino-bis(3-etilbenzotiazolin-6-sülfonik asit (ABTS)'in diamonyum tuzu ve indirgenme gücü (FRAP) yöntemleri kullanılarak belirlendi. Aktivite-bileşik ilişkisi gösterildi. Brush 4 genotipi en yüksek DPPH [296 µmol TE (Trolox ekivalent) /g DW (gram kuru ağırlık)], ABTS (706 µmol TE/g DW) ve FRAP (650 µmol TE/g DW) aktivitesi gösterdi. Rosmarinik asidin bütün genotiplerde en yüksek miktarda olduğu belirlendi. Genotipler arasında Lettuce (3)'ün, 180460.6'lık (mg kg⁻¹ kuru bitki) bir değer ile en fazla rosmarinik asit içerdiği belirlendi.

Anahtar Kelimeler: Reyhan, antioksidan aktivitesi, reyhan kültürü, kantitatif analiz, LC-TOF-MS.

1. INTRODUCTION

Natural products have been consumed extensively for therapeutic properties for centuries.^{1,2} Herbal medicines have been accepted as a main basis of crucial health care in many countries.³ Almost 80% of the world population still depends on folk medicine.

Spectroscopic developments have led to the isolation of active compounds from plants in the 19th century. Hence, many organic advances have been inspired by natural products. Synthetic chemists have begun to synthesize natural products with pharmaceutical properties due to the isolation of natural products.⁴ Natural compound frameworks have been regarded as

special structures consist of the basis of effective medicines.⁵⁻⁹ The importance of natural products is due to the active compounds they contain.¹⁰⁻¹⁸

Ocimum basilicum L., basil, which is an aromatic and medicinal plant belonging to the Labiatae family consists of more than 150 species. Although this plant is native to Mediterranean, Africa, America and Asia, it is widely grown in many countries.¹⁹ Due to its significance for medicine, it is sold as fresh, dried, or frozen as well.²⁰ This plant with essential oils has been employed widely in diet, cosmetics, and dental for many years. *Ocimum basilicum* L. has been consumed for the remedy of various illnesses such as viral ocular and hepatic infections, headaches, coughs, diarrhoea, worm, warts, constipation, kidney malfunction.²¹ The main essential oil compounds of *Ocimum* species have been identified as linalool, geraniol, camphor and 1,8-cineol, which are classified as monoterpenes.²² *Ocimum basilicum* L. essential oil consisting of linalool and eugenol as major products has showed an antibacterial activity on *Giardia lamblia*.²³ Phytochemical studies on *Ocimum* genus has revealed that this plant contains some significant secondary metabolites such as flavonoids, steroids and terpenes, anthocyanins.²⁴ Due to the including bioactive secondary metabolites, *Ocimum* has exhibited a large variety of biological effects such as anticancer, antioxidant, anti-aging, immunity enhancement, antibacterial, diabetes mellitus.²⁵

The compounds of essential oil have terpene skeletons with the high volatility that protects plants from external threats. Essential oils are generally terpenoids, a great various class of secondary metabolites. They have been used extensively in flavour and cosmetic applications since ancient times. Due to their high volatility, the essential oils are released into the air space around the plant. Hence, they play a significant role as signaling compounds for pollinators and herbivores.²⁶⁻²⁸

The eighteen Turkish basil essential oils have been studied, and cluster analysis has been carried out by presenting the variety of essential oils in the landraces. So, seven various chemotypes have been elucidated.²⁹

Antioxidants reveal a significant role for human health by decreasing oxidative stress. In addition, they are used to prevent food from deterioration. Antioxidants have attracted attention against oxidative stress. Antioxidants are divided into natural and synthetic products. Natural antioxidants are preferred by consumers since they are safe, non-toxic and no side effects.³⁰

In this work, the quantitative analyses of phenolic compounds were carried out for 4 commercial basil (Sweet 1, Purple 2, Lettuce 3, Brush 4) grown in Tokat

where Turkey's ecology and antioxidant activity was executed on cultivar basil.

2. MATERIALS AND METHODS

2.1. General

The standard compounds, 2,2-Diphenyl-1-picrylhydrazyl radical (DPPH[•]), 2,2'-Azino-bis(3-ethylbenzothiazoline-6-sulfonic acid) diammonium salt (ABTS), potassium hexacyanoferrate (III), sodium peroxydisulphate, potassium dihydrogen phosphate, trolox, trichloroacetic acid (TCA), sodium carbonate, sodium hydroxide, iron (III) chloride, iron (II) chloride, ethanol, formic acid, acetonitrile, methanol, dichloromethane were supplied from the Sigma-Aldrich company.

2.2. Plant Materials

Seed of four basil cultivars (*Ocimum basilicum* L.), Sweet (1), Purple (2), Lettuce (3), Brush (4) were cultivated at the research field of Tokat Gaziosmanpasa University. The plants were harvested during vegetative period. Plant materials were dried at the shade under room temperature.

2.3. Extraction

Each dried plant sample (0.4 g) was extracted with methanol/dichloromethane (4/1, 20 ml). After vortex stage, each extract solution was kept in the ultrasonic bath at 30°C for 30 min, then the solution was mixed at room temperature for 24 h. The solvent was evaporated by reduced pressure to yield the crude extract for analysis of antioxidant activity and phenolic compounds. Quantitative analyses of phenolic compounds were performed in 4 commercial basil cultivars (Sweet 1, Purple 2, Lettuce 3, Brush 4) by Liquid Chromatography Time-of-Flight Mass Spectrometry (LC-TOF-MS).

2.4. Analysis of phenolic compounds

The extract solutions of *O. basilicum* cultivars were prepared (5 mg l⁻¹). The solutions were filtered through 0.22 µm syringe type PTFE filter then injected into the vials. Quantitative analyses were executed by HPLC system equipped with Agilent 1260 infinity LC pump, 6210 TOF-MS detector and Zorbax SB-C18 (4.6 × 100 mm, 3.5 µm, 2.7 mm) (Agilent Technologies) column. The water with 0.1 formic acid (X) and acetonitrile (Y) were applied for mobile phase. The program was adjusted as follow: 0-2 min 10% Y, 2-21 min 45% Y, 21-25 min 75% Y, 25-29 min 15% Y, 29-35 min, 20% Y. The elution was completed for 35 min. Positive ion mode was used for analysis, the temperature of gas was 320°C, the voltage of fragmentary was 175 volts. The

calibration graph was employed to identify the phenolic compounds. LC-TOF-MS analysis was executed according to retention time and molecular masses of each standart. Concentrations of phenolic compounds were calculated as mg kg⁻¹ dry plant.

2.5. Antioxidant assays

2.5.1. DPPH[•] free radical assay

DPPH[•] activities of *O. basilicum* cultivars were carried out.³¹ 1.0 ml, 0.26 mM of DPPH[•] solution was treated with *O. basilicum* extract at 20, 40, and 80 µl concentrations at room temperature for 30 min. The absorbance was read by a spectrophotometer at 517 nm in which lower absorbance of the reaction product revealed the higher activity. DPPH[•] scavenging activity was calculated from Eq. (1).

$$\text{DPPH}^{\bullet} \text{ scavenging activity (\%)} = [(A1 - A2)/A2] \times 100 \quad (1)$$

where A1 and A2 are control and sample absorbances.³²

2.5.2. ABTS^{•+} scavenging assay

The reaction of ABTS (2.0 mM) with K₂S₂O₈ (potassium persulfate) (2.45 mM) in phosphate buffer for 6 h in dark at room temperature yielded the formation of ABTS^{•+} radical cation solution. Each *O. basilicum* extract solution (40 and 80 µl) was completed to 3 ml with phosphate buffer (pH 7.4, 1.0 ml). Consequently, 1.0 ml of ABTS^{•+} solution was reacted with *O. basilicum* extract solution (3.0 ml). After incubation for 10 min at room temperature, absorbance measurement was executed at 734 nm. The ABTS^{•+} scavenging effect was calculated for each *O. basilicum* extract concentration. The absorbance was measured at 734 nm. ABTS^{•+} scavenging activity was calculation from Eq. (2)

$$\text{ABTS}^{\bullet+} \text{ scavenging effect (\%)} = [(A1 - A2)/A2] \times 100 \quad (2)$$

where A1 is the initial concentration of ABTS^{•+}, and A2 is remaining concentration.³⁰

2.5.3. Reducing power

After preparation of sodium phosphate buffer (0.2 M, pH 6.7), each sample solution was treated with 1.25 ml, 1% of potassium ferricyanide [K₃Fe(CN)₆] for thirty min at 45°C. The buffer solution was added to the reaction mixture until the volume reached to 2.5 ml. 1.25 ml, 10% of trichloroacetic acid and 0.1%, 0.25 ml of iron (III) chloride were added to the reaction mixture.

The absorbance measurement was executed at 700 nm using a spectrophotometer.³²

2.6. Statistical Analyses

SPSS software (SPSS 15.0) was used for the statistical analysis. The trials were repeated triplicate, and the results were presented as mean value and standard deviation (SD). ANOVA one-way analysis was carried for the evaluation of results. Significant variances in groups were indicated at p < 0.05.

3. RESULTS AND DISCUSSION

Quantitative analyses of phenolic compounds from four cultivar basil (*Ocimum basilicum* L.) were presented. Some phenolic compounds were used for the standards (Table 1). Quantitative analysis revealed that rosmarinic acid was the major compound in all genotypes (Table 1). Among the corresponding genotypes, Lettuce (3) consisted of the most rosmarinic acid (18460.6 mg kg⁻¹ DW). Brush (4), Sweet (1), Purple (2) contained the rosmarinic acid with the quantity of 17880.1 mg kg⁻¹ DW, 7805.9 mg kg⁻¹ DW, 2610 mg kg⁻¹ DW respectively. Besides rosmarinic acid, Sweet (1) cultivar consisted of the rutine and chicoric acid as major products with the quantity of 1376.9 mg kg⁻¹ DW and 211.0 mg kg⁻¹ DW respectively. However, Purple (2) consisted of rutin and 4-hydroxybenzoic acid with the value of 669.8 mg kg⁻¹ DW and 216.6 mg kg⁻¹ DW, respectively. Rutin (3532.4 mg kg⁻¹ DW) and 4-hydroxybenzoic acid (228.4 mg kg⁻¹ DW) were detected as the second and third main compounds in Lettuce (3). Brush (4) included the rutin and 4-hydroxybenzoic as the major compounds as well. These cultivars did not contain the chlorogenic acid, apigenin-7-O-glucoside and naringenin.

A research was carried out on three purple Basil (*Ocimum basilicum* L.) cultivars, and six standards were used. It was presented that plant maturity influenced the anthocyanin, phenolic concentrations and reducing capacity significantly, while cultivar had a significant effect on anthocyanin concentrations and FRAP antioxidant activity. Rosmarinic acid was found as a major compound.³³ It is also major compound in our study. Another study was executed on *Ocimum basilicum* L. obtained from three different city of Egypt. The variations of the chemical composition of essential oils were determined. Linalool, estragole, methyl cinnamate, bicyclosesquiphellandrene, eucalyptol, alpha bergamotene, eugenol were the major compounds in all essential oil contents. In addition, methanol extract revealed the more antioxidant activity than that of the essential oils.³⁴ A research was carried out on 15 basil (*Ocimum basilicum* L.) cultivars. It was presented that

Table 1. Phenolic compounds of Basil (*Ocimum basilicum* L.) Landraces (mg k⁻¹ dried plant)

LR	GA	GEA	CA	HA	PA	CFA	HBA	RU	CUA	CCA	FA	RA	SA
1	96.02	40.03	155.38	139.53	0.00	155.61	7.71	1376.94	0.00	211.00	40.49	7805.92	86.46
2	101.77	51.78	153.79	216.59	0.00	140.85	10.23	669.77	11.89	0.00	0.00	2610.15	100.77
3	0.00	44.70	154.03	228.41	0.00	223.17	14.46	3532.35	0.00	144.19	0.00	18460.56	87.85
4	140.15	58.32	264.92	435.83	125.17	277.77	8.49	2026.14	0.00	0.00	44.57	17880.05	91.59

1: Fr sweet, **2:** Fr purple, **3:** Fr lettuce, **4:** Fr brush. GA: gallic acid, GEA: gentisic acid, CA: caftaric acid, CHA: chlorogenic acid, HA: 4-hydroxybenzoic acid, PA: protocatechuic acid, CFA: caffeic acid, HBA: 4-hydroxybenzaldehyde, RU: rutin, CUA: *p*-coumaric acid, CCA: chicoric acid, FA: ferulic acid, HE: hesperidin, AG: apigenin-7-*O*-glucoside, RA: rosmarinic acid, SA: salicylic acid, N: naringenin, LR: landraces. Landraces genotypes do not contain CHA, HE, AG and N.

cultivar influenced the phenolic composition and antioxidant activity. Nine of the cultivars had chicoric acid in high concentrations than rosmarinic acid. Individual phenolic acid composition strongly influenced antioxidant activity.³⁵

The antioxidant activities of water, ethanol, and acetone extracts of purple basil were investigated. It was determined that ethanol extract revealed the most antioxidant activity.³⁶ Our research includes some novelty compared to the corresponding study. Seventeen standards were utilized. The cultivar conditions and basil genotypes were completely different. Hence the results contain novelty in comparison with the previous work.

Antioxidant activities of four basil cultivars (*Ocimum basilicum* L.) were investigated as well. Brush (**4**) showed the most antioxidant activity. DPPH[•], ABTS^{•+} and FRAP activities for Brush (**4**) were assigned as 296.0 μmole TE/g DW, 706.3 μmole TE/g DW, 650.5 μmole TE/g DW, respectively. Lettuce (**3**) cultivar showed the second most activity in all assays including DPPH[•], ABTS^{•+}, and FRAP with the values of 291.8 μmole TE/g DW, 566.9 μmole TE/g DW, 634.9 μmole TE/g DW, respectively. Sweet (**1**) was determined as third active genotype. The activities of DPPH[•], ABTS^{•+} and FRAP for Sweet (**1**) were assigned to 161.5 μmole TE/g DW, 390.0 μmole TE/g DW and 417.0 μmole TE/g DW, respectively. Purple (**2**) genotype revealed the least activity among the investigated genotypes with the values of 93.2 μmole TE/g DW, 203.0 μmole TE/g DW and 150.6 μmole TE/g DW corresponding to the DPPH[•], ABTS^{•+} and FRAP assays, respectively (Table 2).

Lettuce (**3**) (22889.7 mg kg⁻¹) and Brush (**4**) (21353.0 mg kg⁻¹) contained the most phenolic content. Hence, it was seen that there was a direct proportion between phenolic content and activity. However, there could be an active compound in the genotype revealing the

excellent activity caused the genotype to be high in the activity. All cultivar basil composed rosmarinic acid as a major compound. Rosmarinic acid occurs throughout Boraginaceae and Lamiaceae family. Rosmarinic acid is the bioactive compound revealing a large amount of biological activity such as antioxidant, antiinflammatory, antimutagen, antibacterial, and antiviral. Moreover, it is also utilized in cosmetic and food additive to avoid food decay. Therefore, rosmarinic acid is accepted to be one of the most talented food functional polyphenols.³⁷ As a consequence, Basil genotypes could be an effective source of rosmarinic acid.

Table 2. Antioxidant activity of Basil (*Ocimum silicum* L.) landraces (μmole TE/g DW)*

Landraces	DPPH [•]	ABTS ^{•+}	FRAP
Sweet (1)	161.5 ± 14.8b	389.9 ± 6.6c	417.0 ± 13.1c
Purple (2)	93.2 ± 1.5c	202.9 ± 2.0d	150.8 ± 2.6d
Lettuce (3)	291.8 ± 3.9a	566.8 ± 4.0b	634.9 ± 10.1b
Brush (4)	296.0 ± 0.1a	706.3 ± 4.9a	650.2 ± 7.1a

*There is no a significant difference between the mean values to the same letter at the column according to the Duncan test (P < 0.05).

4. CONCLUSION

It was determined that Basil (*Ocimum basilicum* L.) included significant phenolic compounds. Hence, this aromatic and medicinal plant could be a source of corresponding compounds. It was seen that all commercial cultivar basil consisted of rosmarinic acid as a major product with a considerable quantity. Therefore, these genotypes could be the source of

executed to increase the quantity of rosmarinic acid in the *Ocimum basilicum* L.

ACKNOWLEDGEMENTS

This work includes a part of doctoral study of Dr. Nusret Genc. The authors thank to The Scientific and Technological Research Council of Turkey (TUBITAK) for financially support (No: 111O677).

Conflict of interests

Authors declare that there is no a conflict of interest with any person, institute, company, etc.

REFERENCES

- Genç, N.; Yıldız, İ.; Karan, T.; Eminağaoğlu, Ö.; Erenler, R. *Turk. J. Biodiv.* **2019**, 2 (1), 1-5.
- Topçu, G.; Erenler, R.; Çakmak, O.; Johansson, C. B.; Çelik, C.; Chai, H.-B.; Pezzuto, J. M. *Phytochemistry* **1999**, 50 (7), 1195-1199.
- Erenler, R.; Nusret, G.; Elmastaş, M.; Eminağaoğlu, Ö. *Turk. J. Biodiv.* **2019**, 2 (1), 13-17.
- Newman, D. J.; Cragg, G. M. *J. Nat. Prod.* **2007**, 70 (3), 461-477.
- Dede, E.; Genc, N.; Elmastas, M.; Aksit, H.; Erenler, R. *Nat. Prod. J.* **2019**, 9 (3), 238-243.
- Elmastas, M.; Celik, S. M.; Genc, N.; Aksit, H.; Erenler, R.; Gulcin, İ. *Int. J. Food Prop.* **2018**, 21 (1), 374-384.
- Elmastas, M.; Erenler, R.; Isnac, B.; Aksit, H.; Sen, O.; Genc, N.; Demirtas, I. *Nat. Prod. Res.* **2016**, 30 (3), 299-304.
- Erenler, R.; Adak, T.; Karan, T.; Elmastas, M.; Yıldız, I.; Aksit, H.; Topcu, G.; Sanda, M. A. *EPSTEM* **2017**, 139-145.
- Yaglioglu, A. S.; Akdulum, B.; Erenler, R.; Demirtas, I.; Telci, I.; Tekin, S. *Med. Chem. Res.* **2013**, 22 (6), 2946-2953.
- Aksit, H.; Çelik, S. M.; Sen, Ö.; Erenler, R.; Demirtas, I.; Telci, I.; Elmastas, M. *Rec. Nat. Prod.* **2014**, 8 (3), 277-280.
- Elmastaş, M.; Telci, İ.; Akşit, H.; Erenler, R. *Turk. J. Biochem.* **2015**, 40 (6), 456-462.
- Erenler, R.; Sen, O.; Yaglioglu, A. S.; Demirtas, I. *Comb. Chem. High T. Scr.* **2016**, 19 (1), 66-72.
- Aydin, A.; Erenler, R.; Yılmaz, B.; Tekin, Ş. *J. Turk. Chem. Soc., Sec. A: Chem.* **2016**, 3 (3), 217-228.
- Erenler, R.; Sen, O.; Aksit, H.; Demirtas, I.; Yaglioglu, A. S.; Elmastas, M.; Telci, İ. *J. Sci. Food Agr.* **2016**, 96 (3), 822-836.
- Erenler, R.; Pabuccu, K.; Yaglioglu, A. S.; Demirtas, I.; Gul, F. Z. *Naturforsch. C.* **2016**, 71 (3-4), 87-92.
- Erenler, R.; Demirtas, I.; Karan, T.; Altun, M.; Gul, F. *Int. J. Sec. Metabol.* **2017**, 4 (3, Special Issue 2), 512-516.
- Guzel, A.; Aksit, H.; Elmastas, M.; Erenler, R. *Pharmacogn. Mag.* **2017**, 13 (50), 316-320.
- Karan, T.; Erenler, R. *Pharmacogn. Mag.* **2017**, 13 (Suppl 3), 723-725.
- Grayer, R. J.; Bryan, S. E.; Veitch, N. C.; Goldstone, F. J.; Paton, A.; Wollenweber, E. *Phytochemistry* **1996**, 43 (5), 1041-1047.
- Loughrin, J. H.; Kasperbauer, M. J. *J. Agr. Food Chem.* **2001**, 49 (3), 1331-1335.
- Lee, S.J.; Umano, K.; Shibamoto, T.; Lee, K.G. *Food Chem.* **2005**, 91 (1), 131-137.
- Martins, A. P.; Salgueiro, L. R.; Vila, R.; Tomi, F.; Cañigueral, S.; Casanova, J.; da Cunha, A. P.; Adzet, T. *Planta Med.* **1999**, 65 (02), 187-189.
- de Almeida, I.; Alviano, D. S.; Vieira, D. P.; Alves, P. B.; Blank, A. F.; Lopes, A. H. C.; Alviano, C. S.; Maria do Socorro, S. R. *Parasitol. Res.* **2007**, 101 (2), 443-452.
- da Silva, L. A. L.; Pezzini, B. R.; Soares, L. *Pharmacogn. Mag.* **2015**, 11 (41), 96.
- Zhan, Y.; An, X.; Wang, S.; Sun, M.; Zhou, H. *Bioorgan. Med. Chem.* **2020**, 28 (1), 115179.
- Karan, T.; Yıldız, I.; Aydın, A.; Erenler, R. *Rec. Nat. Prod.* **2018**, 12 (3), 273-283.
- Türkmen, N.; Öz, A.; Sönmez, A.; Erol, T.; Gülümser, D.; Yurdakul, B.; Kayır, Ö.; Elmastas, M.; Erenler, R. *J. New Results Sci.* **2014**, 3 (6), 27-31.
- Bayır, B.; Gündüz, H.; Usta, T.; Şahin, E.; Özdemir, Z.; Kayır, Ö.; Sen, Ö.; Akşit, H.; Elmastaş, M.; Erenler, R. *J. New Results Sci.* **2014**, 6, 44-50.
- Telci, I.; Bayram, E.; Yılmaz, G.; Avcı, B. *Biochem.*

Syst. Ecol. **2006**, 34 (6), 489-497.

30. Erenler, R.; Telci, I.; Ulutas, M.; Demirtas, I.; Gul, F.; Elmastas, M.; Kayir, O. *J. Food Biochem.* **2015**, 39 (5), 622-630.

31. Elmastas, M.; Ozturk, L.; Gokce, I.; Erenler, R.; Aboul-Enein, H. Y. *Anal. Lett.* **2004**, 37 (9), 1859-1869.

32. Demirtas, I.; Erenler, R.; Elmastas, M.; Goktasoglu, A. *Food Chem.* **2013**, 136 (1), 34-40.

33. McCance, K. R.; Flanigan, P. M.; Quick, M. M.; Niemeyer, E. D. *J. Food Compost. Anal.* **2016**, 53, 30-39.

34. Ahmed, A. F.; Attia, F. A.; Liu, Z.; Li, C.; Wei, J.; Kang, W. *Food Sci. Hum. Wellness* **2019**, 8 (3), 299-305.

35. Kwee, E. M.; Niemeyer, E. D. *Food Chem.* **2011**, 128 (4), 1044-1050.

36. Yeşiloğlu, Y.; Şit, L. *Spectrochim. Acta A* **2012**, 95, 100-106.

37. Peng, X.; Wang, X. C.; Qi, W.; Su, R. X.; He, Z. M. *Food Chem.* **2016**, 192, 178-187.